Spring 2019

Engineering Multifunctional and Morphologically Diverse Polymer Brush Surfaces

Cassandra M. Reese
University of Southern Mississippi

ENGINEERING MULTIFUNCTIONAL AND MORPHOLOGICALLY DIVERSE POLYMER BRUSH SURFACES

by

Cassandra Maria Reese

A Dissertation
Submitted to the Graduate School,
the College of Arts and Sciences
and the School of Polymer Science and Engineering
at The University of Southern Mississippi
in Partial Fulfillment of the Requirements
for the Degree of Doctor of Philosophy

Approved by:

Dr. Derek L. Patton, Committee Chair
Dr. Sarah E. Morgan
Dr. Robson F. Storey
Dr. Sergei I. Nazarenko
Dr. Yoan C. Simon

Dr. Derek L. Patton Committee Chair	Dr. Jeffrey S. Wiggins Director of School	Dr. Karen S. Coats Dean of the Graduate School

May 2019

Published by the Graduate School

ABSTRACT

The combination of surface-initiated polymerization (SIP) and post-polymerization (PPM) serves as a powerful approach to fabricate complex, multifunctional polymer films, which can be precisely tuned for desired surface engineering applications. Careful manipulation of PPM parameters such as reaction conditions, the tethered brush parameters, and the physical properties of the unbound post-modifier greatly influence the depth of penetration of the post-modifier and the polymer brush compositional heterogeneity. This dissertation focuses on engineering polymer brush surfaces with multifunctional chemistries and tunable morphologies by investigating the PPM parameters that dictate the distribution of post-modifiers on grafted polymer brush surfaces.

The first chapter of this dissertation outlines the benefits of SIP and PPM for the design of complex polymer surfaces. Furthermore, this chapter explains the motivation for designing complex, functional polymer surfaces with tunable morphologies from the nanometer to micron scale.

In the second chapter, microwave-assisted surface-initiated polymerization is exploited to prepare poly(acrylamide-homocysteine thiolactone) (pAHT) brushes. The pAHT brushes serve as a powerful platform to undergo sequential and one-pot amine-thiol-ene conjugation reactions. XPS depth profile experiments provided insight into the modified pAHT brush through-thickness composition and PPM efficiency (e.g. sequential versus one-pot reactions).

The third chapter focuses on a simple PPM approach to engineer buckling instabilities (e.g. wrinkles) in ultrathin (< 100 nm) poly(styrene-*alt*-maleic anhydride)

(pSMA) brush surfaces. The wrinkled morphologies were judiciously tuned by PPM reaction time and anhydride conversion. Partial cross-linking of the outer layer of the pSMA brushes under poor solvent conditions is critical to obtain the wrinkled morphologies upon swelling. ToF-SIMS depth profiling and *in situ* ellipsometry provided insight into the parameters that influence the buckling behavior.

In the fourth chapter, an expression to quantify the applied compressive strain was derived for bilayer systems where the strain is unknown. The expression was validated using a prototypical bilayer model system (e.g. polystyrene on polydimethylsiloxane). Next, the expression was used to quantify the strain of the wrinkled pSMA brushes in the previous chapter. Finally, the calculated strain values of the wrinkled pSMA brushes were corroborated using the relationship between applied strain and persistence length of aligned wrinkles.

ACKNOWLEDGMENTS

First and foremost, I would like to acknowledge my advisor, Dr. Derek L. Patton. You have been an excellent mentor and role model throughout my graduate career. Thank you for your advice, mentorship, and guidance over the years. Thank you for always having an open door and being there when I needed you. You have helped me grow tremendously, personally and professionally, and I thank you for your endless support and holding me to the highest possible standard. You showed me how to think differently, work harder, and pursue any opportunity that I set my mind to. I truly appreciate everything you have done for me.

I would like to express my gratitude to my committee members – Dr. Morgan, Dr. Storey, Dr. Nazarenko, and Dr. Simon for their tremendous support in my professional career. I truly appreciate your guidance throughout my time at USM and your motivation to help me develop as a scientist.

I would like to thank the Patton Research Group (past and present) – Dr. Emily Hoff, Dr. Brian Donovan, Dr. Li Xiong, Dr. Wei Guo, Dr. Yidan Guan, Dr. Dahlia Amato, Dr. Doug Amato, William Walker, Ben Alameda, and Reese Sloan. You all have been outstanding colleagues and friends. Specifically, I would like to express my gratitude to Dr. Wei Guo for being my mentor during my first year in the lab and helping with polymer brush synthesis. My undergraduates – Brittany Thompson and Phillip Logan. Thank you for your hard work and dedication to the projects you contributed to.

I would like to thank all of my collaborators – Dr. Christopher Stafford, Dr. Brad Lokitz, Dr. Olga Ovchinnikova, and Dr. Anton Ievlev. Specifically, I would like to express my gratitude to Dr. Christopher Stafford at NIST for insightful discussions about

wrinkled polymer brushes. Thank you for allowing me to work with you at NIST and helping me grow as a scientist.

Finally, I would like to acknowledge financial support from the NSF Graduate Research Fellowship Program (DGE-1445151) and the NSF NRT program “Interface” (DGE-1449999) for financial and traineeship support, respectively.

DEDICATION

This dissertation is dedicated to my family and fiancé. Mom, I am so lucky to have such a hard-working and loving mother. You are a role model and I'm so grateful to have your persistence and strong-minded personality. I hope to be as amazing as you are one day. Dad, I am grateful to have such an amazing father. You taught me to be a fighter and never give up. Thank you for teaching me to be tenacious and how to fight for my dreams. Mark, you have made a tremendous impact in my life and I am grateful for everything you have done for our family. Anthony, you are an amazing brother and I am so proud of everything you have accomplished. Thank you for believing in me and giving me endless support. Travis, I am so thankful I met you in graduate school. Thank you for always encouraging me to strive both personally and professionally. Thank you for always being supportive and challenging me to be the best person I can be. I am forever grateful for your love, friendship, and support.

TABLE OF CONTENTS

LIST OF TABLES

LIST OF ILLUSTRATIONS

LIST OF SCHEMES

LIST OF ABBREVIATIONS

AFM	atomic force microscopy
AIBN	azobisisobutyronitrile
ATRP	atom-transfer radical polymerization
ATR-FTIR	attenuated total reflection Fourier transform infrared spectroscopy
BBA	4-bromobenzyl amine
CuAAC	copper catalyzed azide-alkyne cyclo addition
DBU	1,8-diazabicyclo[5.4.0]undec-7-ene
DI	deionized
DMSO	dimethyl sulfoxide
EA	ethanolamine
EtOAc	ethyl acetate
EtOH	ethanol
FA	*1H, 1H*-perfluoro-*N*-decyl acrylate
FA	2-(perfluorobutyl)ethyl acrylate
FFT	fast Fourier transform
FTIR	Fourier transform infrared spectroscopy
gATR-FTIR	grazing angle attenuated total reflection Fourier transform infrared spectroscopy
GPC	gel permeation chromatography
HA	hexylamine

HEA	2-hydroxyethyl acrylate
LbL	layer-by-layer
L-B	Langmuir-Blodgett
M_n	number-average molecular weight
MW	molecular weight
N_A	Avogadro's number
NR	neutron reflectivity
PBS	phosphate-buffered saline
PDMS	polydimethylsiloxane
PPM	post-polymerization modification
PPT	propanethiol
pAHT	poly(acrylamide-homocysteine thiolactone)
PDMS	polydimethylsiloxane
PS	polystyrene
pSMA	poly(styrene-*alt*-maleic anhydride)
TEA	triethylamine
QCM	quartz crystal microbalance
QNM	quantitative nanomechanical property mapping
RAFT	reversible addition−fragmentation chain-transfer polymerization
RI	refractive indices
RMS	root-mean-squared

SAMs	self-assembled monolayers
SEM	scanning electron microscopy
SIMS	secondary ion mass spectroscopy
SIP	surface-initiated polymerization
SR	swelling ratio
Sty	styrene
TCEP	tris(2-carboxylethyl) phosphine hydrochloride
TEA	trimethylamine
TEM	transmission electron microscopy
TGA	thermogravimetric analysis
T_g	glass transition temperature
THF	tetrahydrofuran
TlAm	thiolactone acrylamide
ToF-SIMS	time of flight secondary ion mass spectroscopy
UV	ultraviolet
WCA	water contact angle
XPS	X-ray photoelectron spectroscopy
XRR	X-ray reflectivity
μ*CP*	microcontact printing
μ*W-SIP*	microwave-assisted surface-initiated polymerization

CHAPTER I – INTRODUCTION

1.1 Polymer Thin Films

Polymer thin films have been widely used to modify and tune surface properties in a wide variety of high-tech applications such as anti-corrosion,[1,2] lubrication,[3,4] adhesion,[5,6] controlled wettability,[7,8] antibacterial[9] and marine antifouling surfaces.[10] The deposition of thin organic coatings can be categorized into two classes – thin films that are attached by physical forces and films that are covalently bound to the surface.[11] Polymer films that rely on weak inter-molecular forces (e.g. hydrogen bonding, electrostatic interactions, or van der Waal forces) are prepared via a number of methods: Langmuir-Blodgett technique,[12] layer-by-layer (LbL),[13] spin coating, dip coating, doctor blading, and many others.[14] Although these polymer films are easy to prepare, they are less robust and the weak physical interactions may lead to adhesive failure of the system.

An alternative approach to improve the long-term stability of polymer thin films is to use covalent attachment of molecules to a scaffold. A common technique, self-assembled monolayer (SAM), involves the use of small molecules with reactive handles that form covalent linkages with a corresponding moiety on the substrate.[15] Common examples are silanes on oxide surfaces, thiols on noble metal surfaces, or phosphates on metal oxide surfaces. Despite its advantages, the SAM process is self-limiting, meaning the surface-attachment reaction stops when all the reactive moieties have been consumed or are no longer accessible. Consequently, this technique leads to SAM films with very thin layers (less than 5 nm).[16]

1.2 Polymer Brushes

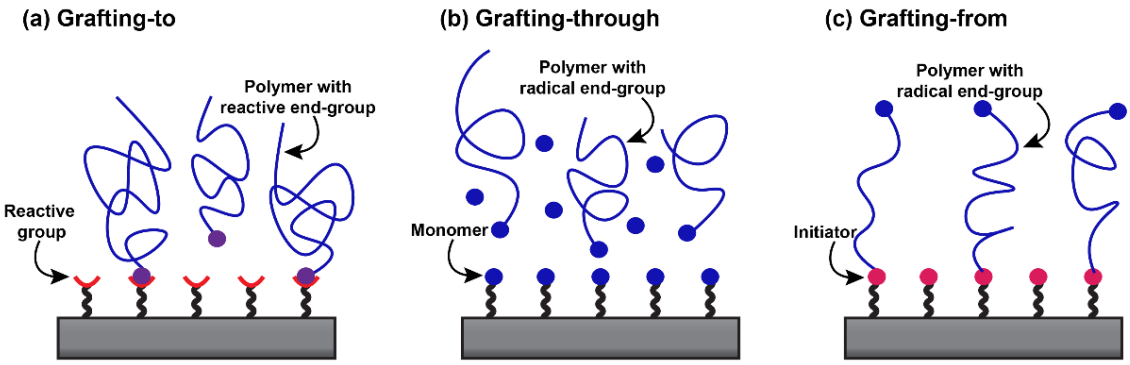

Scheme 1.1 Schematic illustration of various methods for immobilizing chains on surfaces: (a) grafting-to, (b) grafting-through and (c) grafting-from.

Polymer brushes, an array of polymer chains densely grafted to a surface, can be generated via a *grafting-to*, *grafting-through*, or *grafting-from* method (Scheme 1.1).[14,17] The *grafting-to* technique involves the covalent attachment of preformed polymer chains containing predefined functional groups. The location of the predefined functional groups is important. If the functional groups are pendent to the backbone, then a polymer brush is not the resulting product of covalent attachment to a substrate. The *grafting-through* technique incorporates the use of SAMs of monomer or polymerizable groups which participate in solution initiated polymerization.[18,19] However, both methods exhibit a fundamental limitation, polymer grafting density, which is limited both thermodynamically and kinetically.[20] For example, at higher grafting densities the diffusion of polymer chains slows down and the rate of attachment is diffusion-limited. This extremely slow rate of attachment forms a kinetic barrier against incoming polymer chains. Furthermore, the attachment of polymer chains to a surface with a high grafting density becomes unfavorable for thermodynamic reasons.[21] At high grafting densities, the macromolecules adopt an extended chain conformation perpendicular to the substrate

surface due to strong intermolecular segment-segment interactions. Thus, at high grafting densities, a polymer chain in a coil conformation must change to an extended chain conformation at the surface. This results in an entropic penalty due to the establishment of one chemical linkage connecting the chain to the polymer surface, and this penalty limits the attachment of further polymer chains. Furthermore, the final brush thickness is limited by the molecular weight of the polymer in solution (e.g. film thickness of 100 nm are typically inaccessible).

To overcome these limitations, the *grafting-from* strategy is a powerful technique which relies on polymer chains synthesized from an initiator immobilized on a substrate; this technique is also called "surface-initiated polymerization" to indicate that polymerization occurs primarily at the surface.[22,23] In some cases, particularly with azobis-isobutyronitrile (AIBN), one of the most widely used initiators for free radical polymerization, free (non-bound) polymer is generated in the solution, which can easily be washed off.[24] Surface-initiated polymerization (SIP) represents one of the most effective and versatile methods for tailoring the physico-chemical properties of polymer brush surfaces.[25] The ability to modify surfaces with any geometry with outstanding film homogeneity at nanometer thicknesses offers many advantages over solution cast films. Additionally, the three dimensional brush conformation enhances surface functionality by providing functional groups at the interface and throughout the film.[26] This feature makes SIP vastly superior to SAMs where functionality is limited to the outermost edge of the surface. Furthermore, SIP allows for excellent control over film thickness (greater than 100 nm), tunable grafting densities, and functionality of polymer brushes with almost molecular precision.[27]

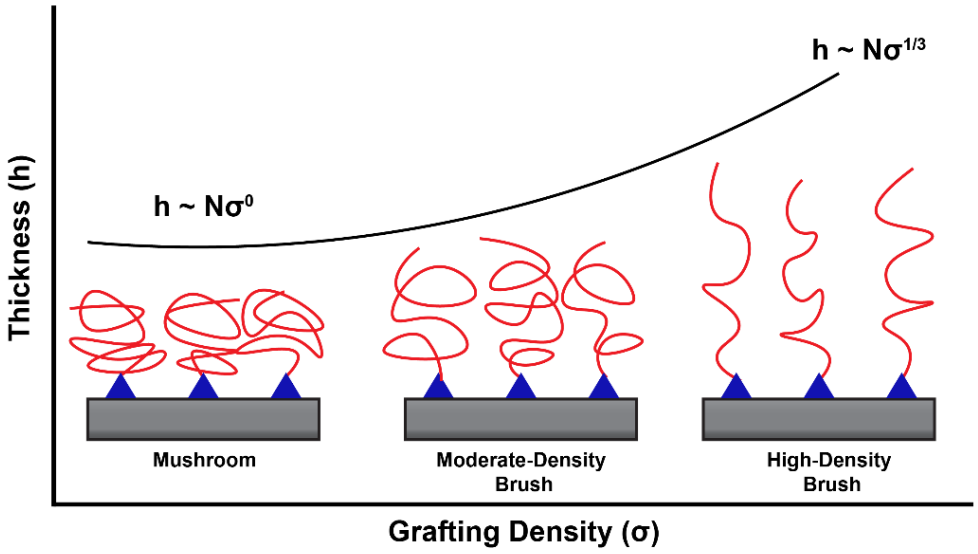

Scheme 1.2 Schematic illustration of the scaling law for brush thickness and grafting density, where h is thickness, N represents the degree of polymerization and σ represents grafting density.

Brittain and Minko[21] developed the key intrinsic parameters which define a polymer brush structure, where the conformation of the polymer chain is related the distance between grafting points. The distance between grafting points is thus related to the transition between the "mushroom" regime and the "brush" regime. This transition can be quantitatively described as the reduced tethered density (Σ)

$$\Sigma = \sigma\pi R_g^2 \qquad \text{Equation 1}$$

where R_g is the radius of gyration of the polymer, and σ is defined as the grafting density:

$$\sigma = \frac{h\rho N_A}{M_n} \qquad \text{Equation 2}$$

where h represents dry polymer brush thickness, ρ is the bulk density of the polymer, N_A is Avogadro's number, and M_n is the number average molecular weight. The bulk density (ρ) of the polymer brush is generally assumed to be equivalent to that of the bulk polymer. At low grafting densities, polymer chains adopt the so-called "mushroom" or

"pancake" conformation. Conversely, at high grafting densities, the surface-bound chains adopt the highly stretched "brush" conformation, where the polymer brush thickness (h) scales to the 1/3 power of the grafting density (σ) (Scheme 1.2).[11,28]

Polymer brushes can be synthesized via numerous methods such as anionic/cationic polymerization,[29] ring-opening polymerization,[30,31] radical polymerization techniques (e.g. thermal and photo-initiated free radical polymerization), nitroxide-mediated polymerization,[32] atom transfer radical polymerization (ATRP),[33–35] and reversible addition-fragmentation chain transfer polymerization.[36,37] Surface-initiated ATRP has the benefit of designing polymers with end-groups capable of reinitiating polymerization, which is useful to design copolymer structures with controlled block sizes.[38,39]

1.3 Characterization of Polymer Brush Surfaces

The analysis and characterization of ultrathin polymer brush surfaces remain a significant challenge due to reduced dimensionality of the polymer chains.[40] Therefore, there is a great need to understand the fundamental properties of polymer brushes at interfaces for advanced technologies. A number of characterization techniques (spectroscopic, microscopic, and optical) are used to characterize polymer brush interfaces.

1.3.1 Spectroscopic and Optical Characterization Techniques

Ultra-violet-visible (UV-Vis) spectroscopy is a direct method to measured polymer film growth from transparent substrates. In addition, the kinetics of polymer brush post-polymerization modification (Section 1.4) can be measured using UV-Vis.[41]

X-ray reflectivity (XRR) and neutron reflectivity (NR) techniques can be used to determine film thickness, short-range and long-range ordering, and diffusion kinetics.[38,42–45]

The chemical functionality can be determined via attenuated total reflectance Fourier transform infrared spectroscopy (ATR-FTIR), X-ray photoelectron spectroscopy (XPS), and time-of-flight secondary ion mass spectroscopy (ToF-SIMS). In particular, ATR-FTIR is used to monitor specific IR-sensitive functional groups.[46,47] XPS[48–50] and ToF-SIMS[51,52] probe the relative abundance of atomic species on the surface. XPS determines the elemental surface composition of a surface by irradiating the surface with an X-ray beam and measuring the kinetic energy of the photoelectrons escaping the top 1-10 nm of the material. ToF-SIMS utilizes a pulsed ion beam which causes secondary ions to be emitted from the outermost layer (0.1-1 nm) of the sample surface. The time-of-flight analyzer measures the mass of the emitted ions, which is used to determine the identity of an element. Furthermore, sputtering techniques can be utilized in combination with XPS or ToF-SIMS to determine the chemical composition of a polymer brush as a function of film thickness or sputtering depth.[44,53–55]

Optical techniques, such as ellipsometry, are used to monitor film thickness.[56] Ellipsometry is a non-destructive characterization technique that measures the change in polarization as light reflects or transmits from a thin film. The change in polarization is quantified by the amplitude ratio (Ψ) and the phase difference (Δ). The film thickness can be determined by comparing it to a multilayer model based on Fresnel equations, with a given refractive index of each layer. *In situ* ellipsometry has also been explored to monitor the swelling behavior of polymer brush surfaces.[57]

1.3.2 Microscopy Characterization Techniques

Microscopy techniques are utilized to determine surface roughness, morphology, and phase segregation. The common techniques include atomic force microscopy (AFM),[55,58] scanning electron microscopy (SEM),[59] optical microscopy,[60–62] and fluorescence microscopy.[63,64] AFM has also been used to determine the mechanical properties, such as modulus[65,66] and adhesion,[67,68] of polymer brush surfaces.

1.3.3 Other Characterization Methods

Contact angle measurements using a goniometer allow the determination of surface free energy or tension of a sample. This measurement is indicative of the hydrophobicity or hydrophilicity of a surface. Quartz crystal microbalance (QCM) is a sensitive technique that measures nanogram to microgram changes in mass per unit area. Specifically, QCM with dissipation allows changes in frequency and dissipation of a quartz crystal resonator and has been utilized to monitor conformational changes of polymer brushes upon swelling..[69,70]

Gel permeation chromatography (GPC) can be used to determine the number average molecular weight (M_n) of the solution-borne polymer formed from the free initiator (e.g. AIBN) in solution. Another method is to cleave the polymer brush chains with hydrofluoric acid and measure the M_n via GPC.[71] In other cases, a sacrificial initiator is added to the monomer solution in order to determine M_n and control film thickness.[72–74]

1.4 Click Chemistry and Post-Polymerization Modification (PPM)

Despite recent advances in SIP, there remains a broad range of complex side-chain functionalities that cannot be introduced via direct polymerization using any

controlled polymerization technique. Certain functional groups cannot be directly polymerized from the surface due to i) exorbitant cost of functional monomer synthesis and/or ii) intolerance of the functional moiety in the polymerization process (i.e. reactivity, steric bulk).[75] A modular approach that circumvents the aforementioned concerns is to fabricate polymer brushes with reactive side chain functionality, which can be modified with the molecule of interest via a sequential post-polymerization modification (PPM) step (Scheme 1.3).[76] PPM of polymer brushes is a powerful approach for tailoring the chemical and mechanical properties of polymer brush surfaces.[77–79] Click chemistry, a method of PPM, was first introduced by Sharpless in 2001 and is defined as reactions that are modular, utilize readily available reactions, and exhibit fast kinetics.[80–82] A number of "click" reactions have been exploited for surface modification, such as copper-catalyzed azide-alkyne cycloadditions (CuAAC),[83–85] activated ester-amine reactions,[86–88] Diels-Alder cycloadditions,[89–93] epoxy nucleophilic ring-opening reactions,[94–96] and thiol-based reactions (e.g. thiol-ene,[63,76,97,98] thiol-alkyne,[61,99] thiol-isocyanate,[62] and thiol-disulfide[100]). Of these thiol-click approaches, the use of a thiolactone (a cyclic thioester) as a latent thiol functionality has gained significant interest as a versatile PPM route for the design of multifunctional materials.[101–103] However, thiolactone chemistry has yet to be explored as a modular approach for the design of complex polymer brush surfaces. To address this unexplored area, the utility of thiolactone as a PPM strategy is explored in the following section.

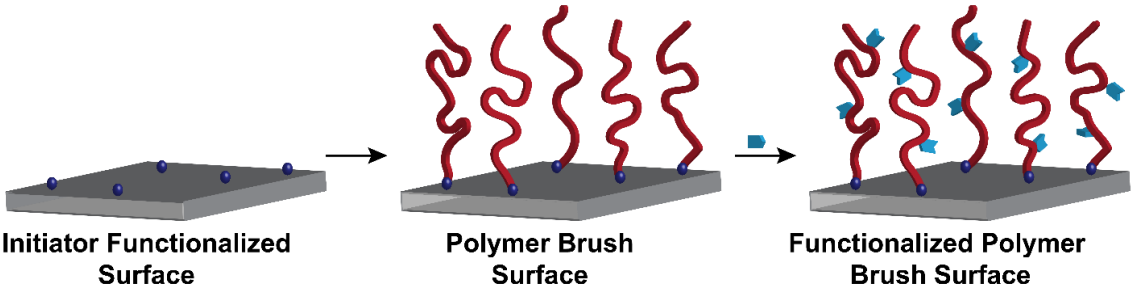

Scheme 1.3 Schematic illustration of post-polymerization modification of polymer brush surfaces.

1.4.2 Thiolactones as a PPM Strategy

Thiolactone derivatives have emerged as a powerful platform for the design of multifunctional materials via orthogonal modifications.[104] Thiolactones are cyclic esters of mercapto-acids, which can contain four-, five- and six-membered rings. The common synthetic procedure for the preparation of thiolactones is the direct lactonization of the corresponding mercapto-acid.[105–107] Due to the inherent ring strain, the ring-opening of the thiolactone ring is dictated by the ring size. A number of nucleophiles can be utilized for the ring-opening reactions (amines, alcohols, water), however, hydrolysis and alcoholysis only occur in basic medium.[108–110] Thus, aminolysis is the preferred route to ring-open the thiolactone since it does not require an additional additive for the reaction to occur. The aminolysis reaction generally follows second-order kinetics.[111] Espeel et al. demonstrated that the stereo-electronic properties of the primary amines dictate the relative rate differences during the aminolysis reaction of γ-thiobutyrolactone (Scheme 1.4).[101] For example, aliphatic nonfunctional primary amines (amine 1, Scheme 1.4) react faster than amines containing an inductive-withdrawing group (amines 3-7). Furthermore, the steric constraints from branching of Jeffamine (amine 8, Scheme 1.4) greatly decreases the reaction rate.

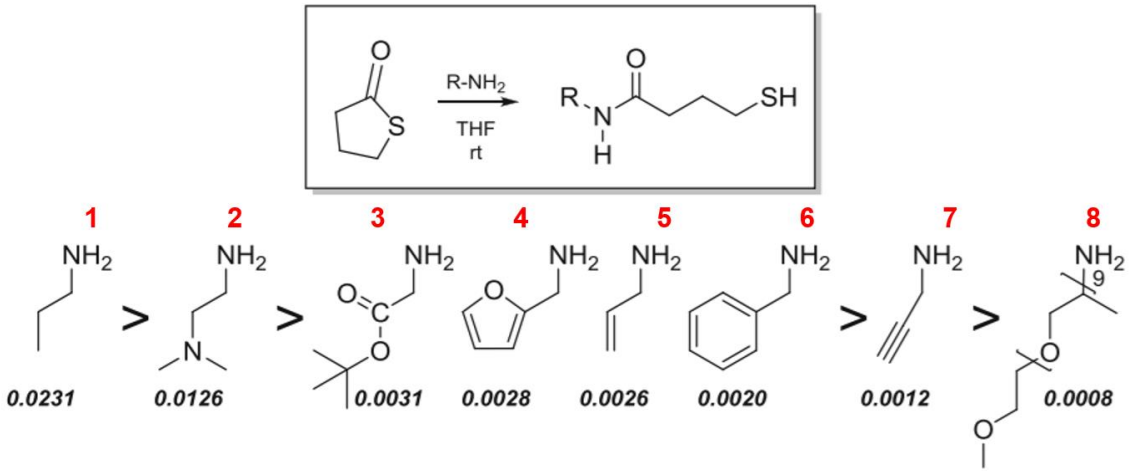

Scheme 1.4 Rate constants (L mol^{-1} s^{-1}) of the aminolysis of γ-thiobutyrolactone in the presence of various primary amines (reproduced from ref. 101 with permission).

After nucleophilic ring-opening of the thiolactone with primary amines, the thiol is released (Scheme 1.5a) and can undergo sequential thiol-coupling chemistries such as radical-mediated thiol-ene, nucleophilic thiol-Michael addition, and thiol-disulfide exchange. The double PPM of thiolactone-containing polymers allows site-specific chemoselective transformations, which allows the incorporation of multiple functional groups in an orthogonal fashion.[112,113] The PPM of the thiolactone moiety can be performed in a two-step process (Scheme 1.5a) or in a one-pot double modification reaction (Scheme 1.5b).[101,103,104]

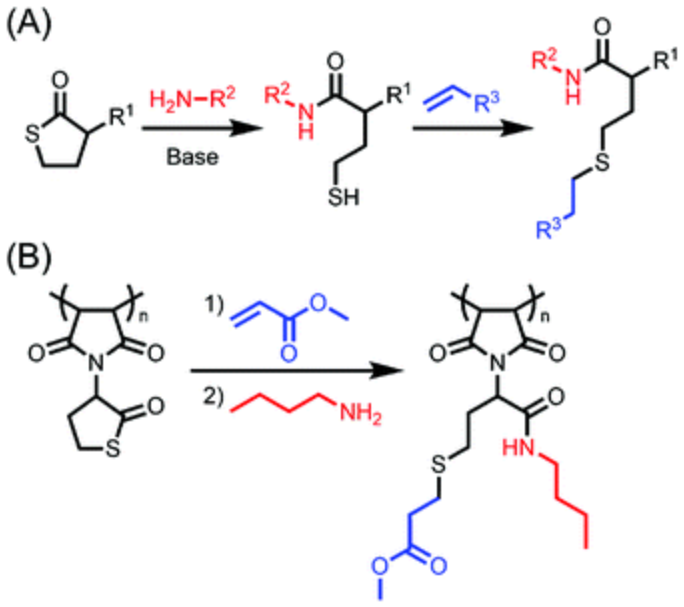

Scheme 1.5 (A) Aminolysis of thiolactone group, followed by sequential thiol-click modification. (B) One pot, double modification of thiolactone-containing polymers (reproduced from ref. 103 with permission).

The synthetic approach of thiolactone chemistry has two major advantages compared to other efficient activated-ester chemistries employed in PPM reactions. First, thiolactone PPM chemistry exhibits 100 % atom-efficient reactions since no small molecule condensate is formed. In addition, this double modification strategy can be performed in an efficient one-pot reaction, accelerating the amine-thiol-ene PPM reactions. Du Prez and others[114–116] have demonstrated the potential for thiolactone chemistry and the design for new polymeric architectures, with a recent focus on sequence-controlled polymers.[117]

1.5 PPM Efficiency in Polymer Brushes

Although PPM is a well-established strategy to engineer functional polymer surfaces, this technique is particularly challenging due to the reduced chain conformational entropy of stretched polymer chains, which renders the penetration of the

brush by reactive post-modifiers into the brush highly unfavorable.[118,119] Thus, the efficacy, depth of penetration and through-thickness compositional homogeneity of the PPM process in the brush regime are ultimately dependent on i) the reaction conditions (i.e. solvent quality, reaction efficiency, and reaction time), ii) the tethered brush parameters (i.e. grafting density and thickness), and iii) the physical properties of the unbound reactive modifier (i.e. molecular mass and steric bulk).

For example, under good solvent conditions and a large excess of the reactive post-modifiers (low molecular weight) relative to the reactive moieties on the brush, the PPM reaction can be described by pseudo-first-order kinetics. Arnold et al. reported a pseudo-first-order kinetic model for the aminolysis of activated ester polymer brush surfaces.[41] In addition, Guo and coworkers reported pseudo-first-order kinetics of the aminolysis of styrene-maleic anhydride copolymer brushes.[58] However, the PPM kinetics results were separated into two regimes, where the latter had a lower rate constant as the PPM reaction becomes more diffusion limited. The transition into the diffusion limited regime is attributed to strong segmental repulsion and reduced chain conformational entropy rendering the penetration of the brush by a post-modifier more unfavorable as the reaction proceeds. Similar PPM kinetics have been reported by Orski et al.[85]

Conversely, for high molecular weight reactive modifiers, the PPM conversion is often less than quantitative. Therefore, it can be assumed that increases in brush thickness, grafting density, and MW of the reactive modifier will lead to a decreased depth of penetration and consequently, an increased brush compositional heterogeneity. The investigation of the aforementioned parameters (i-iii) on PPM of polymer brush conformation was investigated using neutron reflectivity[45] and XPS[44] depth profiling.

Specifically, Schüwer et al. investigated the PPM of poly(2-hydroxyethyl methacrylate) brushes using NR.[45] The experiments indicated that smaller post-modifiers penetrate deeper into the polymer brush, and brushes with higher thickness and grafting density resulted in the post-modifier reaction to occur primarily at the polymer/air interface. Alswieleh and coworkers recently demonstrated the use of solvent quality to spatially control cross-linking throughout the brush (Scheme 1.6), where poor solvent (hexane) resulted in cross-linking primarily in the surface region of the brush due to a collapsed brush conformation.[120] Conversely, good solvent (THF) led to uniform cross-linking throughout the swollen brush. Intentional manipulation of PPM parameters provides an opportunity to design polymer brush surfaces with through-thickness heterogeneities that fulfill the requirements for nanoscale buckling within ultrathin films on rigid substrates.

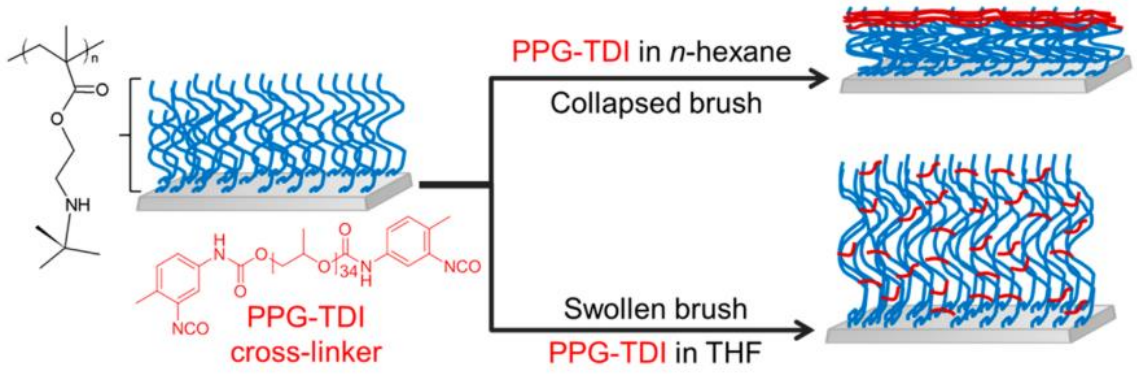

Scheme 1.6 Schematic illustration of spatial control of cross-linking using solvent quality (reproduced from reference 118 with permission).

1.6 Designing Polymer Surfaces with Buckling Instabilities

Buckling instabilities (wrinkles, creases, and folds) are a universal phenomenon in natural and synthetic systems over a wide range of length scales. Common examples are wrinkling in human skin, imperfectly cured coatings, and thin rigid materials expanding while being bound to a compliant polymer film.[121,122] In polymeric films, stresses beyond

a critical strain can trigger deformations in the film, resulting in interfacial delamination and fracture, which ultimately leads to undesirable applications.[123] However, in recent years, researchers have focused on utilizing wrinkling and other surface instabilities to tailor material properties and control surface topography.[124,125] Significant efforts have focused on exploiting this approach to create surfaces suitable for a wide range of applications, including adjustable adhesives,[126] tunable optics,[127,128] stretchable electronics,[129] anti-counterfeit technologies,[130] stem-cell growth and differentiation,[131] antifouling,[132,133] and metrology.[134]

Scheme 1.7 Schematic depiction of wrinkles developing in a bilayer film comprised of rigid film attached to a soft substrate. The wrinkles exhibit a wrinkle wavelength, λ, and amplitude, A.

Buckling instabilities in polymer films can be engineered using three primary film structures: layered, homogeneous, and gradient systems.[135,136] In the prototypical example, surface wrinkling can occur from an in-plane compression (thermal, osmotic, or mechanical) of a bilayer film composed of a thin, high modulus film bonded to a semi-infinite, low modulus substrate (Scheme 1.7). The critical strain, ε_c, for wrinkling is dictated by the difference in mechanical properties of the bilayer film[135]

$$\varepsilon_c = \frac{1}{4}\left(\frac{3\bar{E}_s}{\bar{E}_f}\right)^{2/3} \qquad \text{Equation 3}$$

where $\bar{E} = E/(1-\nu^2)$, E and ν are the plane-strain modulus, Young's modulus, and Poisson's ratio of the film (f) and the substrate (s), respectively. Above a critical strain,

the film buckles and forms sinusoidal wrinkles throughout the film surface. The onset and wavelength of the wrinkles are dictated by the thickness, t, of the top film and the film/substrate modulus ratio

$$\lambda_c = 2\pi t \left(\frac{3\bar{E}_f}{\bar{E}_s}\right)^{1/3} \qquad \text{Equation 4}$$

The amplitude, A, of the wrinkles is related to the applied compressive strain, ε

$$A = t\left(\frac{\varepsilon}{\varepsilon_c} - 1\right)^{1/2} \qquad \text{Equation 5}$$

Researchers have demonstrated numerous methods to construct a modulus mismatch between the stiff layer and underlying substrate, including metal deposition,[137] UV/ozone oxidation,[138] photoinduced cross-linking,[139,140] and surface grafting techniques[141]; however, these methods have focused primarily on thin films on elastomeric substrates. Typically, the top layer consists of a hard material, such as a metal. However, polymer brushes enable an alternative strategy as they exhibit anisotropic mechanical properties due to the finite extensibility of the polymer chains perpendicular to the surface. Additionally, covalent tethering of the chains to the surface resists film delamination from the substrate. Although polymer brushes serve as an alternative approach for wrinkling in bilayer films, relatively few studies have focused on methods to include buckling instabilities in ultrathin (< 100 nm) polymer films attached to rigid substrates.[142–144]

Brooks et al.[145] reported the fabrication of nanoscale creases in ultrathin poly(pentafluorophenyl acrylate) (pPFPA) brushes on rigid silicon substrates following PPM of the pPFPA with an amine-terminated polymer using microcontact printing (μCP). The PPM process increased the molecular mass of the pPFPA brush resulting in

osmotic swelling normal to the substrate surface. Confinement of swollen brush under the μCP stamp led to a critical in-plane stress, which was relieved via formation of creases. The size and structure of the creases were modulated by varying brush grafting density and pressure applied during the μCP process. This approach was extended to fabricate creased morphologies using reactive diffusion of a viscous amine-terminated polymer solution to provide confinement.[88]

Recently, we reported a simple route to engineer wrinkled morphologies in polymer brush surfaces using PPM techniques.[55] Specifically, cross-linking poly(styrene-*alt*-maleic anhydride) under poor solvent conditions limits the PPM reaction to the near surface region of the brush, where reaction time dictates the thickness of the cross-linked surface region. Exposure of the cross-linked brush to good solvent conditions generates an in-plane compressive stress from the mismatch between lateral and perpendicular swelling directions within the brush. The stress causes an out-of-plane deformation, resulting in the observed wrinkled morphologies. We demonstrated a simple method to judiciously tune wrinkle wavelength by manipulating cross-linking time.

1.7 Summary and Dissertation Overview

The combination of surface-initiated polymerization and post-polymerization modifications serves as an attractive approach for tailoring the chemical and mechanical properties of polymer brush surfaces. PPM efficiency is governed by multiple factors such as solvent quality, reaction time, grafting density, brush thickness, and the physical properties of the post-modifier. Intentional manipulation of PPM parameters provides a route to engineer polymer brush scaffolds with complex functionalities and through-thickness heterogeneities that satisfy the requirements for surface buckling.

This dissertation focuses on the design and synthesis of polymer brush surfaces with reactive functional moieties for robust, sequential post-polymerization modification to develop multifunctional surfaces. This approach can be further utilized to engineer surfaces with complex morphologies across multiple length scales (e.g. nanometer to micron).

In Chapter II, poly(acrylamide-homocysteine thiolactone) (pAHT) was synthesized via microwave-assisted surface-initiated polymerization (μW-SIP). Modification of pAHT brushes with primary amines generates a thiol precursor, which undergoes sequential base-catalyzed thiol-Michael reactions. Additionally, a one-pot double modification reaction is employed to demonstrate the versatility of thiolactone chemistry as a powerful PPM platform. XPS depth profile experiments provided insight into the PPM efficiency (e.g. sequential vs one-pot reactions) of pAHT brush surfaces.

In Chapter III, PPM of poly(styrene-*alt*-maleic anhydride) (pSMA) copolymer brushes enabled a simple route to engineer tunable wrinkled morphologies. The length scale of the buckled features is tuned using PPM reaction time. Characterization of the PPM kinetics and swelling behavior via ellipsometry and ToF-SIMS provided key insight into parameters influencing the buckling behavior.

In Chapter IV, an expression to deduce the compressive strain of wrinkled pSMA brushes is derived. First, the expression is validated using a model system (e.g. polystyrene mounted onto a PDMS substrate). Next, the expression is utilized to quantify the applied strain of the wrinkled pSMA brush surfaces. Finally, this methodology is used to elucidate the relationship between applied compressive strain and the persistence length of aligned wrinkles via AFM lithography.

1.8 References

(1) Caldona, E. B.; De Leon, A. C. C.; Thomas, P. G.; Naylor, D. F.; Pajarito, B. B.; Advincula, R. C. Superhydrophobic Rubber-Modified Polybenzoxazine/SiO_2 Nanocomposite Coating with Anticorrosion, Anti-Ice, and Superoleophilicity Properties. *Ind. Eng. Chem. Res.* **2017**, *56* (6), 1485–1497. https://doi.org/10.1021/acs.iecr.6b04382.

(2) Das, S.; Kumar, S.; Samal, S. K.; Mohanty, S.; Nayak, S. K. A Review on Superhydrophobic Polymer Nanocoatings: Recent Development and Applications. *Ind. Eng. Chem. Res.* **2018**, *57* (8), 2727–2745. https://doi.org/10.1021/acs.iecr.7b04887.

(3) Goda, T.; Konno, T.; Takai, M.; Ishihara, K. Photoinduced Phospholipid Polymer Grafting on Parylene Film: Advanced Lubrication and Antibiofouling Properties. *Colloids Surfaces B Biointerfaces* **2007**, *54* (1), 67–73. https://doi.org/10.1016/j.colsurfb.2006.09.006.

(4) Klein, Jacob; Kumacheva, Eugenia; Mahalu, Diana; Perahia, Dvora; Fetter, L. J. Reduction of Frictional Forces between Solid Surfaces Bearing Polymer Brushes. *Nature* **1994**, *370*, 634–636. https://doi.org/10.1038/370634a0

(5) Balzer, B. N.; Micciulla, S.; Dodoo, S.; Zerball, M.; Gallei, M.; Rehahn, M.; V. Klitzing, R.; Hugel, T. Adhesion Property Profiles of Supported Thin Polymer Films. *ACS Appl. Mater. Interfaces* **2013**, *5* (13), 6300–6306. https://doi.org/10.1021/am4013424.

(6) Xia, W.; Hsu, D. D.; Keten, S. Dependence of Polymer Thin Film Adhesion Energy on Cohesive Interactions between Chains. *Macromolecules* **2014**, *47* (15), 5286–5294. https://doi.org/10.1021/ma5006974.

(7) Anastasiadis, S. H. Development of Functional Polymer Surfaces with Controlled Wettability. *Langmuir* **2013**, *29* (30), 9277–9290. https://doi.org/10.1021/la400533u.

(8) Lee, H. J.; Park, K. Variable Wettability Control of a Polymer Surface by Selective Ultrasonic Imprinting and Hydrophobic Coating. *Colloid Polym. Sci.* **2016**, *294* (9), 1413–1423. https://doi.org/10.1007/s00396-016-3902-y.

(9) Cloutier, M.; Mantovani, D.; Rosei, F. Antibacterial Coatings: Challenges, Perspectives, and Opportunities. *Trends Biotechnol.* **2015**, *33* (11), 637–652. https://doi.org/10.1016/j.tibtech.2015.09.002.

(10) Chambers, L. D.; Stokes, K. R.; Walsh, F. C.; Wood, R. J. K. Modern Approaches to Marine Antifouling Coatings. *Surf. Coatings Technol.* **2006**, *201* (6), 3642–3652. https://doi.org/10.1016/j.surfcoat.2006.08.129.

(11) Rühe, J. Polymer Brushes: On the Way to Tailor-Made Surfaces. In *Polymer brushes*, Wiley: 2006; pp 1-31. https://doi.org/10.1002/3527603824.ch0.

(12) Moehwald, H.; Brezesinski, G. From Langmuir Monolayers to Multilayer Films. *Langmuir* **2016**, *32* (41), 10445–10458. https://doi.org/10.1021/acs.langmuir.6b02518.

(13) Decher, G.; Schlenoff, J. *Materials, Multilayer Thin Films: Sequential Assembly of Nanocomposite Materials*, Wiley-VCH: 2012.

(14) Halperin, A.; Tirrell, M.; Lodge, T. P. Tethered Chains in Polymer

Microstructures. *Macromol. Synth. Order Adv. Prop.* **1992**, *100*, 31–71. https://doi.org/10.1007/BFb0051635.
(15) Ulman, A. Formation and Structure of Self-Assembled Monolayers. *Chem. Rev.* **1996**, *96* (4), 1533–1554. https://doi.org/10.1021/cr9502357.
(16) Ulman, A. *An Introduction to Ultrathin Organic Films From Langmuir - Blodgett to Self-Assembly*; Elsevier Science, 2013.
(17) Zhao, B.; Brittain, W. J. Polymer Brushes: Surface-Immobilized Macromolecules. *Prog. Polym. Sci.* **2000**, *25* (5), 677–710. https://doi.org/10.1016/S0079-6700(00)00012-5.
(18) Mohammadi Sejoubsari, R.; Martinez, A. P.; Kutes, Y.; Wang, Z.; Dobrynin, A. V.; Adamson, D. H. "Grafting-Through": Growing Polymer Brushes by Supplying Monomers through the Surface. *Macromolecules* **2016**, *49* (7), 2477–2483. https://doi.org/10.1021/acs.macromol.6b00183.
(19) Henze, M.; Mädge, D.; Prucker, O.; Rühe, J. "Grafting through": Mechanistic Aspects of Radical Polymerization Reactions with Surface-Attached Monomers. *Macromolecules* **2014**, *47* (9), 2929–2937. https://doi.org/10.1021/ma402607d.
(20) Rühe, J. Polymer Brushes: On the Way to Tailor-Made Surfaces. *In Polymer Brushes: Synthesis, Characterization, Applications*; Advincula, R. C., Brittain, W. J., Caster, K. C., Ruhe, J., Eds.; Wiley-VCH Verlag GmbH & Co. KGaA, 2005; pp 1-50.
(21) Brittain, W. J.; Minko, S. A Structural Definition of Polymer Brushes. *J. Polym. Sci. Part A Polym. Chem.* **2007**, *45* (16), 3505–3512. https://doi.org/10.1002/pola.22180.
(22) Azzaroni, O. Polymer Brushes Here, There, and Everywhere: Recent Advances in Their Practical Applications and Emerging Opportunities in Multiple Research Fields. *J. Polym. Sci. Part A Polym. Chem.* **2012**, *50* (16), 3225–3258. https://doi.org/10.1002/pola.26119.
(23) Minko, S. Grafting on Solid Surfaces: "Grafting to" and "Grafting from" Methods. In *Polymer Surfaces and Interfaces: Characterization, Modification, and Applications*; Stamm, M., Ed.; Springer Berlin Heidelberg, 2008; pp 215–234.
(24) Rühe, J.; Knoll, W. Functional Polymer Brushes. *Macromol. Sci. Part C Polym. Rev.* **2002**, *C42*, 91–138.
(25) Prucker, O.; Rühe, J. Polymer Layers through Self-Assembled Monolayers of Initiators. *Langmuir* **1998**, *14* (24), 6893–6898. https://doi.org/10.1021/la971035o.
(26) Murata, H.; Prucker, O.; Rühe, J. Synthesis of Functionalized Polymer Monolayers from Active Ester Brushes. *Macromolecules* **2007**, *40* (15), 5497–5503. https://doi.org/10.1021/ma0624550.
(27) Edmondson, S.; Osborne, V. L. V.; Huck, W. T. S. W. Polymer Brushes via Surface-Initiated Polymerizations. *Chem. Soc. Rev.* **2004**, *33* (1), 14–22. https://doi.org/10.1039/b210143m.
(28) Milner, S. T. Polymer Brushes. *Science* **1991**, *251*, 905–914.
(29) Advincula, R. Polymer Brushes by Anionic and Cationic Surface-Initiated Polymerization (SIP). *Adv. Polym. Sci.* **2006**, *197* (1), 107–136. https://doi.org/10.1007/12_066.
(30) Weck, M.; Jackiw, J. J.; Rossi, R. R.; Weiss, P. S.; Grubbs, R. H. Ring-Opening

Metathesis Polymerization from Surfaces. *J. Am. Chem. Soc.* **1999**, *121* (16), 4088–4089. https://doi.org/10.1021/ja983297y.
(31) Carrot, G.; Rutot-Houzé, D.; Pottier, A.; Degée, P.; Hilborn, J.; Dubois, P. Surface-Initiated Ring-Opening Polymerization: A Versatile Method for Nanoparticle Ordering. *Macromolecules* **2002**, *35* (22), 8400–8404. https://doi.org/10.1021/ma020558m.
(32) Barbey, R.; Lavanant, L.; Paripovic, D.; Schuwer, N.; Sugnaux, C.; Tugulu, S.; Klok, H.-A. Polymer Brushes via Surface-Initiated Controlled Radical Polymerization: Synthesis, Characterization, Properties, and Applications. *Chem. Rev.* **2009**, *109*, 5437–5527. https://doi.org/10.1021/cr900045a.
(33) Pyun, J.; Kowalewski, T.; Matyjaszewski, K. Synthesis of Polymer Brushes Using Atom Transfer Radical Polymerization. *Macromol. Rapid Commun.* **2003**, *24* (18), 1043–1059. https://doi.org/10.1002/marc.200300078.
(34) Kang, C.; Crockett, R. M.; Spencer, N. D. Molecular-Weight Determination of Polymer Brushes Generated by SI-ATRP on Flat Surfaces. *Macromolecules* **2014**, *47* (1), 269–275. https://doi.org/10.1021/ma401951w.
(35) Bao, Z.; Bruening, M. L.; Baker, G. L. Control of the Density of Polymer Brushes Prepared by Surface-Initiated Atom Transfer Radical Polymerization. *Macromolecules* **2006**, *39* (16), 5251–5258. https://doi.org/10.1021/ma060095a.
(36) Baum, M.; Brittain, W. J. Synthesis of Polymer Brushes on Silicate Substrates via Reversible Addition Fragmentation Chain Transfer Technique. *Macromolecules* **2002**, *35* (3), 610–615. https://doi.org/10.1021/ma0112467.
(37) Li, C.; Benicewicz, B. C. Synthesis of Well-Defined Polymer Brushes Grafted onto Silica Nanoparticles via Surface Reversible Addition-Fragmentation Chain Transfer Polymerization. *Macromolecules* **2005**, *38* (14), 5929–5936. https://doi.org/10.1021/ma050216r.
(38) Kai, Y.; Hanfu, W.; Longjian, X.; Yanchun, H. Stimuli-Responsive Polyelectrolyte Block Copolymer Brushes Synthesized from the Si Wafer via Atom-Transfer Radical Polymerization. *Langmuir* **2007**, *23* (3), 1443–1452. https://doi.org/10.1021/la062159g.
(39) Kim, J. B.; Huang, W.; Bruening, M. L.; Baker, G. L. Synthesis of Triblock Copolymer Brushes by Surface-Initiated Atom Transfer Radical Polymerization. *Macromolecules* **2002**, *35* (14), 5410–5416. https://doi.org/10.1021/ma011736z.
(40) Advincula, R. C. The Analysis and Characterization of Polymer Brushes: From Flat Surfaces to Nanoparticles. In *Polymer Brushes: Synthesis, Characterization, Applications*; Advincula, R. C., Brittain, W. J., Caster, K. C., Ruhe, J., Eds.; Wiley-VCH Verlag GmbH & Co. KGaA, 2005; pp 189–211.
(41) Arnold, R. M.; Sheppard, G. R.; Locklin, J. Comparative Aminolysis Kinetics of Different Active Ester Polymer Brush Platforms in Postpolymerization Modification with Primary and Aromatic Amines. *Macromolecules* **2012**, *45* (13), 5444–5450. https://doi.org/10.1021/ma3005839.
(42) Currie, E. P. K.; Wagemaker, M.; Stuart, M. A. C.; Van Well, A. A. Structure of Grafted Polymers, Investigated with Neutron Reflectometry. *Phys. B Condens. Matter* **2000**, *283* (1–3), 17–21. https://doi.org/10.1016/S0921-4526(99)01883-9.
(43) Levicky, R.; Koneripalli, N.; Tirrell, M.; Satija, S. K. Concentration Profiles in

Densely Tethered Polymer Brushes. *Macromolecules* **1998**, *31* (11), 3731–3734. https://doi.org/10.1021/ma9717653.
(44) Barbey, R.; Laporte, V.; Alnabulsi, S.; Klok, H. Postpolymerization Modification of Poly(Glycidyl Methacrylate) Brushes: An XPS Depth-Profiling Study. *Macromolecules* **2013**, *46*, 6151–6158.
(45) Schüwer, N.; Geue, T.; Hinestrosa, J. P.; Klok, H. A. Neutron Reflectivity Study on the Postpolymerization Modification of Poly(2-Hydroxyethyl Methacrylate) Brushes. *Macromolecules* **2011**, *44* (17), 6868–6874. https://doi.org/10.1021/ma201069d.
(46) Yamamoto, S.; Ejaz, M.; Tsujii, Y.; Fukuda, T. Surface Interaction Forces of Well-Defined, High-Density Polymer Brushes Studied by Atomic Force Microscopy. 2. Effect of Graft Density. *Most* **2000**, 5608–5612. https://doi.org/10.1021/ma991988o.
(47) Kawaguchi, M.; Kato, T.; Takahashi, A.; Nagata, N.; Yoshioka, A. Adsorption of Polybutadienes with Polar Group Terminations on the Solid Surface. 1. Infrared Study at the Silica Surface. *Macromolecules* **1988**, *21* (4), 1059–1062. https://doi.org/10.1021/ma00182a036.
(48) Kong, X.; Kawai, T.; Abe, J.; Iyoda, T. Amphiphilic Polymer Brushes Grown from the Silicon Surface by Atom Transfer Radical Polymerization. *Macromolecules* **2001**, *34* (6), 1837–1844. https://doi.org/10.1021/ma001152h.
(49) Advincula, R.; Zhou, Q.; Park, M.; Wang, S.; Mays, J.; Sakellariou, G.; Pispas, S.; Hadjichristidis, N. Polymer Brushes by Living Anionic Surface Initiated Polymerization on Flat Silicon (SiOx) and Gold Surfaces: Homopolymers and Block Copolymers. *Langmuir* **2002**, *18* (22), 8672–8684. https://doi.org/10.1021/la025962t.
(50) Fan, X.; Xia, C.; Fulghum, T.; Park, M. K.; Locklin, J.; Advincula, R. C. Polymer Brushes Grafted from Clay Nanoparticles Adsorbed on a Planar Substrate by Free Radical Surface-Initiated Polymerization. *Langmuir* **2003**, *19* (3), 916–923. https://doi.org/10.1021/la026039u.
(51) De Los Santos Pereira, A.; Kostina, N. Y.; Bruns, M.; Rodriguez-Emmenegger, C.; Barner-Kowollik, C. Phototriggered Functionalization of Hierarchically Structured Polymer Brushes. *Langmuir* **2015**, *31* (21), 5899–5907. https://doi.org/10.1021/acs.langmuir.5b01114.
(52) Stetsyshyn, Y.; Raczkowska, J.; Lishchynskyi, O.; Awsiuk, K.; Zemla, J.; Dąbczyński, P.; Kostruba, A.; Harhay, K.; Ohar, H.; Orzechowska, B.; Panchenko, Y.; Vankevych, P.; Budkowski, A. Glass Transition in Temperature-Responsive Poly(Butyl Methacrylate) Grafted Polymer Brushes. Impact of Thickness and Temperature on Wetting, Morphology, and Cell Growth. *J. Mater. Chem. B* **2018**, *6* (11), 1613–1621. https://doi.org/10.1039/c8tb00088c.
(53) Kim, Y. P.; Bong, S. L.; Kim, E.; Choi, I. S.; Dae, W. M.; Tae, G. L.; Kim, H. S. Activity-Based Assay of Matrix Metalloproteinase on Nonbiofouling Surfaces Using Time-of-Flight Secondary Ion Mass Spectrometry. *Anal. Chem.* **2008**, *80* (13), 5094–5102. https://doi.org/10.1021/ac800299d.
(54) LeMieux, M. C.; Peleshanko, S.; Anderson, K. D.; Tsukruk, V. V. Adaptive Nanomechanical Response of Stratified Polymer Brush Structures. *Langmuir*

2007, *23* (1), 265–273. https://doi.org/10.1021/la061723k.
(55) Guo, W.; Reese, C. M.; Xiong, L.; Logan, P. K.; Thompson, B. J.; Stafford, C. M.; Ievlev, A. V.; Lokitz, B. S.; Ovchinnikova, O. S.; Patton, D. L. Buckling Instabilities in Polymer Brush Surfaces via Postpolymerization Modification. *Macromolecules* **2017**, *50* (21), 8670–8677. https://doi.org/10.1021/acs.macromol.7b01888.
(56) Kostruba, A.; Ohar, M.; Kulyk, B.; Zolobko, O.; Stetsyshyn, Y. Surface Modification by Grafted Sensitive Polymer Brushes: An Ellipsometric Study of Their Properties. *Appl. Surf. Sci.* **2013**, *276*, 340–346. https://doi.org/10.1016/j.apsusc.2013.03.094.
(57) Habicht, J.; Schmidt, M.; Rühe, J.; Johannsmann, D. Swelling of Thick Polymer Brushes Investigated with Ellipsometry. *Langmuir* **1999**, *15* (7), 2460–2465. https://doi.org/10.1021/la980573d.
(58) Guo, W.; Xiong, L.; Reese, C. M.; Amato, D. V.; Thompson, B. J.; Logan, P. K.; Patton, D. L. Post-Polymerization Modification of Styrene-Maleic Anhydride Copolymer Brushes. *Polym. Chem.* **2017**, *8* (44), 6778–6785. https://doi.org/10.1039/c7py01659j.
(59) Juang, A.; Scherman, O. A.; Grubbs, R. H.; Lewis, N. S. Formation of Covalently Attached Polymer Overlayers on Si(111) Surfaces Using Ring-Opening Metathesis Polymerization Methods. *Langmuir* **2001**, *17* (5), 1321–1323. https://doi.org/10.1021/la0012945.
(60) Panzarasa, G.; Dübner, M.; Soliveri, G.; Edler, M.; Griesser, T. Branched Poly(Ethyleneimine): A Versatile Scaffold for Patterning Polymer Brushes by Means of Remote Photocatalytic Lithography. *Nanotechnology* **2017**, *28* (39). https://doi.org/10.1088/1361-6528/aa8108.
(61) Hensarling, R. M.; Doughty, V. A.; Chan, J. W.; Patton, D. L. "Clicking" Polymer Brushes with Thiol-Yne Chemistry: Indoors and Out. *J. Am. Chem. Soc.* **2009**, *131* (41), 14673–14675. https://doi.org/10.1021/ja9071157.
(62) Hensarling, R. M.; Rahane, S. B.; Leblanc, A. P.; Sparks, B. J.; White, E. M.; Locklin, J.; Patton, D. L. Thiol-Isocyanate "Click" Reactions: Rapid Development of Functional Polymeric Surfaces. *Polym. Chem.* **2011**, *2* (1), 88–90. https://doi.org/10.1039/c0py00292e.
(63) Buhl, M.; Tesch, M.; Lamping, S.; Moratz, J.; Studer, A.; Ravoo, B. J. Preparation of Functional Alternating Polymer Brushes and Their Orthogonal Surface Modification through Microcontact Printing. *Chem. - A Eur. J.* **2017**, *23* (25), 6042–6047. https://doi.org/10.1002/chem.201603565.
(64) Lamping, S.; Otremba, T.; Ravoo, B. J. Carbohydrate-Responsive Surface Adhesion Based on the Dynamic Covalent Chemistry of Phenylboronic Acid- and Catechol-Containing Polymer Brushes. *Angew. Chemie - Int. Ed.* **2018**, *57* (9), 2474–2478. https://doi.org/10.1002/anie.201711529.
(65) Li, A.; Ramakrishna, S. N.; Schwarz, T.; Benetti, E. M.; Spencer, N. D. Tuning Surface Mechanical Properties by Amplified Polyelectrolyte Self-Assembly: Where "Grafting-from" Meets "Grafting-To." *ACS Appl. Mater. Interfaces* **2013**, *5* (11), 4913–4920. https://doi.org/10.1021/am4006379.
(66) Kutnyanszky, E.; Vancso, G. J. Nanomechanical Properties of Polymer Brushes by

Colloidal AFM Probes. *Eur. Polym. J.* **2012**, *48* (1), 8–15. https://doi.org/10.1016/j.eurpolymj.2011.09.008.
(67) Bhairamadgi, N. S.; Pujari, S. P.; Leermakers, F. A. M.; Van Rijn, C. J. M.; Zuilhof, H. Adhesion and Friction Properties of Polymer Brushes: Fluoro versus Nonfluoro Polymer Brushes at Varying Thickness. *Langmuir* **2014**, *30* (8), 2068–2076. https://doi.org/10.1021/la404915k.
(68) Landherr, L. J. T.; Cohen, C.; Agarwal, P.; Archer, L. A. Interfacial Friction and Adhesion of Polymer Brushes. *Langmuir* **2011**, *27* (15), 9387–9395. https://doi.org/10.1021/la201396m.
(69) Jhon, Y. K.; Bhat, R. R.; Jeong, C.; Rojas, O. J.; Szleifer, I.; Genzer, J. Salt-Induced Depression of Lower Critical Solution Temperature in a Surface-Grafted Neutral Thermoresponsive Polymer. *Macromol. Rapid Commun.* **2006**, *27* (9), 697–701. https://doi.org/10.1002/marc.200600031.
(70) Tanoue, H.; Yamada, N. L.; Ito, K.; Yokoyama, H. Quantitative Analysis of Polymer Brush Formation Kinetics Using Quartz Crystal Microbalance: Viscoelasticity of Polymer Brush. *Langmuir* **2017**, *33* (21), 5166–5172. https://doi.org/10.1021/acs.langmuir.7b00961.
(71) Zoppe, J. O.; Ataman, N. C.; Mocny, P.; Wang, J.; Moraes, J.; Klok, H. Surface-Initiated Controlled Radical Polymerization : State-of-the-Art, Opportunities, and Challenges in Surface and Interface Engineering with Polymer Brushes. *Chem. Rev.* **2017**, *117*, 1105-1318. https://doi.org/10.1021/acs.chemrev.6b00314.
(72) Husseman, M.; Malmström, E. E.; McNamara, M.; Mate, M.; Mecerreyes, D.; Benoit, D. G.; Hedrick, J. L.; Mansky, P.; Huang, E.; Russell, T. P.; Hawker, C. J. Controlled Synthesis of Polymer Brushes by "Living" Free Radical Polymerization Techniques. *Macromolecules* **1999**, *32* (5), 1424–1431. https://doi.org/10.1021/ma981290v.
(73) Ejaz, M.; Yamamoto, S.; Ohno, K.; Tsujii, Y.; Fukuda, T. Controlled Graft Polymerization of Methyl Methacrylate on Silicon Substrate by the Combined Use of the Langmuir−Blodgett and Atom Transfer Radical Polymerization Techniques. *Macromolecules* **1998**, *31* (17), 5934–5936. https://doi.org/10.1128/AAC.29.5.955.
(74) Marutani, E.; Yamamoto, S.; Ninjbadgar, T.; Tsujii, Y.; Fukuda, T.; Takano, M. Surface-Initiated Atom Transfer Radical Polymerization of Methyl Methacrylate on Magnetite Nanoparticles. *Polymer (Guildf).* **2004**, *45* (7), 2231–2235. https://doi.org/10.1016/j.polymer.2004.02.005.
(75) Galvin, C. J.; Genzer, J. Applications of Surface-Grafted Macromolecules Derived from Post-Polymerization Modification Reactions. *Prog. Polym. Sci.* **2012**, *37* (7), 871–906. https://doi.org/10.1016/j.progpolymsci.2011.12.001.
(76) Arnold, R. M.; Patton, D. L.; Popik, V. V.; Locklin, J. A Dynamic Duo: Pairing Click Chemistry and Postpolymerization Modification to Design Complex Surfaces. *Acc. Chem. Res.* **2014**, *47* (10), 2999–3008. https://doi.org/10.1021/ar500191m.
(77) Mansfeld, U.; Pietsch, C.; Hoogenboom, R.; Becer, C. R.; Schubert, U. S. Clickable Initiators, Monomers and Polymers in Controlled Radical Polymerizations - A Prospective Combination in Polymer Science. *Polym. Chem.*

2010, *1* (10), 1560–1598. https://doi.org/10.1039/c0py00168f.
(78) Gauthier, M. A.; Gibson, M. I.; Klok, H. A. Synthesis of Functional Polymers by Post-Polymerization Modification. *Angew. Chemie - Int. Ed.* **2009**, *48* (1), 48–58. https://doi.org/10.1002/anie.200801951.
(79) Boaen, N. K.; Hillmyer, M. A. Post-Polymerization Functionalization of Polyolefins. *Chem. Soc. Rev.* **2005**, *34* (3), 267–275. https://doi.org/10.1039/b311405h.
(80) Kolb, H. C.; Finn, M. G.; Sharpless, K. B. Click Chemistry: Diverse Chemical Function from a Few Good Reactions. *Angew. Chemie - Int. Ed.* **2001**, *40* (11), 2004–2021. https://doi.org/10.1002/1521-3773(20010601)40:11<2004::AID-ANIE2004>3.0.CO;2-5.
(81) Kolb, H. C.; Sharpless, K. B. The Growing Impact of Click Chemistry on Drug Discovery. *Drug Discov. Today* **2003**, *8*, 1128–1137. https://doi.org/10.1016/s1936-7961(08)00219-4.
(82) Barner-Kowollik, C.; Du Prez, F. E.; Espeel, P.; Hawker, C. J.; Junkers, T.; Schlaad, H.; Van Camp, W. "Clicking" Polymers or Just Efficient Linking: What Is the Difference? *Angew. Chemie - Int. Ed.* **2011**, *50* (1), 60–62. https://doi.org/10.1002/anie.201003707.
(83) Zhang, S.; Vi, T.; Luo, K.; Koberstein, J. T. Kinetics of Polymer Interfacial Reactions: Polymer Brush Formation by Click Reactions of Alkyne End-Functional Polymers with Azide-Functional Substrates. *Macromolecules* **2016**, *49* (15), 5461–5474. https://doi.org/10.1021/acs.macromol.6b01220.
(84) Arslan, M.; Tasdelen, M. A. Polymer Nanocomposites via Click Chemistry Reactions. *Polymers (Basel).* **2017**, *9* (10), 1-24. https://doi.org/10.3390/polym9100499.
(85) Orski, S. V.; Sheppard, Gareth, R.; Arumugam, S.; Arnold, R. M.; Popik, V. V.; Locklin, J. Rate Determination of Azide Click Reactions onto Alkyne Polymer Brush Scaffolds: A Comparison of Conventional and Catalyst-Free Cycloadditions for Tunable Surface Modification. *Langmuir* **2012**, *28*, 14693–14702. https://doi.org/10.1021/la3032418.
(86) Brooks, K.; Razavi, M. J.; Wang, X.; Locklin, J. Nanoscale Surface Creasing Induced by Post-Polymerization Modification. *ACS Nano* **2015**, *9* (11), 10961–10969. https://doi.org/10.1021/acsnano.5b04144.
(87) Brooks, K.; Yatvin, J.; McNitt, C. D.; Reese, R. A.; Jung, C.; Popik, V. V.; Locklin, J. Multifunctional Surface Manipulation Using Orthogonal Click Chemistry. *Langmuir* **2016**, *32* (26), 6600–6605. https://doi.org/10.1021/acs.langmuir.6b01591.
(88) Brooks, K.; Razavi, M. J.; White, E. M.; Wang, X.; Locklin, J. The Formation and Evolution of Creased Morphologies Using Reactive Diffusion in Ultrathin Polymer Brush Platforms. *Adv. Mater. Interfaces* **2017**, *4* (13), 1–7. https://doi.org/10.1002/admi.201700084.
(89) Arumugam, S.; Orski, S. V.; Locklin, J.; Popik, V. V. Photoreactive Polymer Brushes for High-Density Patterned Surface Derivatization Using a Diels-Alder Photoclick Reaction. *J. Am. Chem. Soc.* **2012**, *134* (1), 179–182. https://doi.org/10.1021/ja210350d.

(90) Arumugam, S.; Popik, V. V. Patterned Surface Derivatization Using Diels-Alder Photoclick Reaction. *J. Am. Chem. Soc.* **2011**, *133* (39), 15730–15736. https://doi.org/10.1021/ja205652m.
(91) Yameen, B.; Rodriguez-Emmenegger, C.; Preuss, C. M.; Pop-Georgievski, O.; Verveniotis, E.; Trouillet, V.; Rezek, B.; Barner-Kowollik, C. A Facile Avenue to Conductive Polymer Brushes via Cyclopentadiene-Maleimide Diels-Alder Ligation. *Chem. Commun.* **2013**, *49* (77), 8623–8625. https://doi.org/10.1039/c3cc44683b.
(92) Gevrek, T. N.; Bilgic, T.; Klok, H. A.; Sanyal, A. Maleimide-Functionalized Thiol Reactive Copolymer Brushes: Fabrication and Post-Polymerization Modification. *Macromolecules* **2014**, *47* (22), 7842–7851. https://doi.org/10.1021/ma5015098.
(93) Yuksekdag, Y. N.; Gevrek, T. N.; Sanyal, A. Diels-Alder "Clickable" Polymer Brushes: A Versatile Catalyst-Free Conjugation Platform. *ACS Macro Lett.* **2017**, *6* (4), 415–420. https://doi.org/10.1021/acsmacrolett.7b00041.
(94) Soto-Cantu, E.; Lokitz, B. S.; Hinestrosa, J. P.; Deodhar, C.; Messman, J. M.; Ankner, J. F.; Kilbey, S. M. Versatility of Alkyne-Modified Poly(Glycidyl Methacrylate) Layers for Click Reactions. *Langmuir* **2011**, *27* (10), 5986–5996. https://doi.org/10.1021/la2000798.
(95) Lokitz, B. S.; Messman, J. M.; Hinestrosa, J. P.; Alonzo, J.; Verduzco, R.; Brown, R. H.; Osa, M.; Ankner, J. F.; Kilbey, S. M. Dilute Solution Properties and Surface Attachment of RAFT Polymerized 2-Vinyl-4,4-Dimethyl Azlactone (VDMA). *Macromolecules* **2009**, *42* (22), 9018–9026. https://doi.org/10.1021/ma9015399.
(96) Barbey, R.; Klok, H. A. Room Temperature, Aqueous Post-Polymerization Modification of Glycidyl Methacrylate-Containing Polymer Brushes Prepared via Surface-Initiated Atom Transfer Radical Polymerization. *Langmuir* **2010**, *26* (23), 18219–18230. https://doi.org/10.1021/la102400z.
(97) Gevrek, T. N.; Bilgic, T.; Klok, H. A.; Sanyal, A. Maleimide-Functionalized Thiol Reactive Copolymer Brushes: Fabrication and Post-Polymerization Modification. *Macromolecules* **2014**, *47* (22), 7842–7851. https://doi.org/10.1021/ma5015098.
(98) Cai, T.; Wang, R.; Neoh, K. G.; Kang, E. T. Functional Poly(Vinylidene Fluoride) Copolymer Membranes via Surface-Initiated Thiol-Ene Click Reactions. *Polym. Chem.* **2011**, *2* (8), 1849–1858. https://doi.org/10.1039/c1py00106j.
(99) Wang, C.; Ren, P. F.; Huang, X. J.; Wu, J.; Xu, Z. K. Surface Glycosylation of Polymer Membrane by Thiol-Yne Click Chemistry for Affinity Adsorption of Lectin. *Chem. Commun.* **2011**, *47* (13), 3930–3932. https://doi.org/10.1039/c1cc10634a.
(100) Li, L.; Feng, W.; Welle, A.; Levkin, P. A. UV-Induced Disulfide Formation and Reduction for Dynamic Photopatterning. *Angew. Chemie* **2016**, *128* (44), 13969–13973. https://doi.org/10.1002/ange.201607276.
(101) Espeel, P.; Goethals, F.; Driessen, F.; Nguyen, L.-T. T.; Du Prez, F. E. One-Pot, Additive-Free Preparation of Functionalized Polyurethanes via Amine–thiol–ene Conjugation. *Polym. Chem.* **2013**, *4* (8), 2373-2616. https://doi.org/10.1039/c3py00004d.
(102) Espeel, P.; Goethals, F.; Stamenović, M. M.; Petton, L.; Du Prez, F. E. Double Modular Modification of Thiolactone-Containing Polymers: Towards Polythiols

and Derived Structures. *Polym. Chem.* **2012**, *3* (4), 1007-1015. https://doi.org/10.1039/c2py00565d.
(103) Espeel, P.; Goethals, F.; Du Prez, F. E. One-Pot Multistep Reactions Based on Thiolactones: Extending the Realm of Thiol-Ene Chemistry in Polymer Synthesis. *J. Am. Chem. Soc.* **2011**, *133* (6), 1678–1681. https://doi.org/10.1021/ja1098098.
(104) Espeel, P.; Du Prez, F. E. One-Pot Multi-Step Reactions Based on Thiolactone Chemistry: A Powerful Synthetic Tool in Polymer Science. *Eur. Polym. J.* **2015**, *62*, 247–272. https://doi.org/10.1016/j.eurpolymj.2014.07.008.
(105) Pattenden, G.; Shuker, A. J. Synthetic Studies towards Leinamycin. A Concise Synthesis of the Spiro-Fused 1,3-Dioxo-1,2-Dithiolane Moiety. *Tetrahedron Lett.* **1991**, *32* (45), 6625–6628. https://doi.org/10.1016/0040-4039(91)80239-3.
(106) Vegh, D.; Zalupsky, P.; Morel, J.; Decroix, B. A New Convenient Method for Preparation of Condensed Aromatic and Heterocyclic Thiolactones. *Synth. Commun.* **1992**, *22* (14), 2057–2061. https://doi.org/10.1080/00397919208021340.
(107) Garbiras, B. J.; Marburg, S. Preparation of Carboxythiolactones and Their Active Derivatives. *Synthesis (Stuttg).* **1999**, No. 2, 270–274. https://doi.org/10.1055/s-00000084.
(108) Montgomery, J. A.; Clayton, S. J.; Thomas, H. J.; Shannon, W. M.; Arnett, G.; Bodner, A. J.; Kion, I.; Cantoni, G. L.; Chiang, P. K. Carbocyclic Analogue of 3-Deazaadenosine : A Novel Antiviral Agent Using S -Adenosylhomocysteine Hydrolase as a Pharmacological Target. *J. Med. Chem.* **1982**, *25*, 626–629. https://doi.org/10.1021/jm00348a004.
(109) Montgomery, J. A.; Thomas, H. J.; Thorpe, M. C. Synthesis of S- (3-Deazaadenosy 1) -L-Homocysteine. *J. Med. Chem.* **1981**, *24*, 1514–1516. https://doi.org/10.1021/jm00144a028.
(110) Espeel, P.; Du Prez, F. E. One-Pot Double Modification of Polymers Based on Thiolactone Chemistry. *Adv Polym Sci.* **2015**, *269*, 105–132. https://doi.org/10.1007/12.
(111) Garel, J.; Tawfik, D. S. Mechanism of Hydrolysis and Aminolysis of Homocysteine Thiolactone. *Chem. - A Eur. J.* **2006**, *12* (15), 4144–4152. https://doi.org/10.1002/chem.200501145.
(112) Durmaz, H.; Sanyal, A.; Hizal, G.; Tunca, U. Double Click Reaction Strategies for Polymer Conjugation and Post-Functionalization of Polymers. *Polym. Chem.* **2012**, *3* (4), 825–835. https://doi.org/10.1039/c1py00471a.
(113) Tunca, U. Orthogonal Multiple Click Reactions in Synthetic Polymer Chemistry. *J. Polym. Sci. Part A Polym. Chem.* **2014**, *52* (22), 3147–3165. https://doi.org/10.1002/pola.27379.
(114) De Bruycker, K.; Mertens, C.; Du Prez, F. E. Thiolactone Chemistry for the Synthesis of Functional Silicon-Based Amphiphilic Co-Networks. *J. Polym. Sci. Part A Polym. Chem.* **2019**, *57*, 322-333. https://doi.org/10.1002/pola.29179
(115) Martens, S.; Holloway, S. O.; Du Prez, F. E. Click and Click-Inspired Chemistry for the Design of Sequence-Controlled Polymers. *Macromol. Rapid Commun.* **2017**, *38*, 1700469. https://doi.org/10.1002/marc.201700469
(116) Kubo, T.; Easterling, C. P.; Olson, R. A.; Sumerlin, B. S. Synthesis of Multifunctional Homopolymers via Sequential Post-Polymerization Reactions.

Polym. Chem. **2018**, *9*, 4605-4610. https://doi.org/10.1039/C8PY01055B.
(117) Driessen, F.; Du Prez, F. E.; Espeel, P. Precision Multisegmented Macromolecular Lineups: A Display of Unique Control over Backbone Structure and Functionality. *ACS Macro Lett.* **2015**, *4* (6), 616–619. https://doi.org/10.1021/acsmacrolett.5b00231.
(118) Schuh, C.; Rühe, J. Penetration of Polymer Brushes by Chemical Nonidentical Free Polymers. *Macromolecules* **2011**, *44* (9), 3502–3510. https://doi.org/10.1021/ma102410z.
(119) Zhulina, E. B.; Borisov, O. V.; Brombacher, L. Theory of a Planar Grafted Chain Layer Immersed in a Solution of Mobile Polymer. *Macromolecules* **1991**, *24* (16), 4679–4690. https://doi.org/10.1021/ma00016a031.
(120) Alswieleh, A. M.; Cheng, N.; Leggett, G. J.; Armes, S. P. Spatial Control over Cross-Linking Dictates the PH-Responsive Behavior of Poly(2-(Tert - Butylamino)Ethyl Methacrylate) Brushes. *Langmuir* **2014**, *30* (5), 1391–1400. https://doi.org/10.1021/la403666y.
(121) Cerda, E.; Mahadevan, L. Geometry and Physics of Wrinkling. *Phys. Rev. Lett.* **2003**, *90* (7), 074302-1-4. https://doi.org/10.1088/0264-9381/20/6/701.
(122) Yang, S.; Khare, K.; Lin, P. C. Harnessing Surface Wrinkle Patterns in Soft Matter. *Adv. Funct. Mater.* **2010**, *20* (16), 2550–2564. https://doi.org/10.1002/adfm.201000034.
(123) Hutchinson, J. W.; Thouless, M. D.; Liniger, E. G. Growth and Configurational Stability of Circular, Buckling-Driven Film Delaminations. *Acta Metall. Mater.* **1992**, *40* (2), 295–308. https://doi.org/10.1016/0956-7151(92)90304-W.
(124) Yoo, P. J.; Suh, K. Y.; Park, S. Y.; Lee, H. H. Physical Self-Assembly of Microstructures by Anisotropic Buckling. *Adv. Mater.* **2002**, *14* (19), 1383–1387. https://doi.org/10.1002/1521-4095(20021002)14:19<1383::AID-ADMA1383>3.0.CO;2-D.
(125) Chan, E. P.; Crosby, A. J. Fabricating Microlens Arrays by Surface Wrinkling. *Adv. Mater.* **2006**, *18* (24), 3238–3242. https://doi.org/10.1002/adma.200601595.
(126) Jeong, H. E.; Kwak, M. K.; Suh, K. Y. Stretchable, Adhesion-Tunable Dry Adhesive by Surface Wrinkling. *Langmuir* **2010**, *26* (4), 2223–2226. https://doi.org/10.1021/la904290g.
(127) Harrison, C.; Stafford, C. M.; Zhang, W.; Karim, A. Sinusoidal Phase Grating Created by a Tunably Buckled Surface. *Appl. Phys. Lett.* **2004**, *85* (18), 4016–4018. https://doi.org/10.1063/1.1809281.
(128) Görrn, P.; Lehnhardt, M.; Kowalsky, W.; Riedl, T.; Wagner, S. Elastically Tunable Self-Organized Organic Lasers. *Adv. Mater.* **2011**, *23*, 869–872. https://doi.org/10.1002/adma.201003108.
(129) Khang, D.-Y.; Jiang, H.; Huang, Y.; Rogers, J. A. A Stretchable Form of Single-Crystal. *Science.* **2006**, *311*, 208–212. https://doi.org/10.1126/science.1121401.
(130) Bae, H. J.; Bae, S.; Park, C.; Han, S.; Kim, J.; Kim, L. N.; Kim, K.; Song, S. H.; Park, W.; Kwon, S. Biomimetic Microfingerprints for Anti-Counterfeiting Strategies. *Adv. Mater.* **2015**, *27* (12), 2083–2089. https://doi.org/10.1002/adma.201405483.
(131) Guvendiren, M.; Burdick, J. A. The Control of Stem Cell Morphology and

Differentiation by Hydrogel Surface Wrinkles. *Biomaterials* **2010**, *31* (25), 6511–6518. https://doi.org/10.1016/j.biomaterials.2010.05.037.
(132) Hoipkemeier-Wilson, L.; Schumacher, J. F.; Carman, M. L.; Gibson, A. L.; Feinberg, A. W.; Callow, M. E.; Finlay, J. A.; Callow, J. A.; Brennan, A. B. Antifouling Potential of Lubricious, Micro-Engineered, PDMS Elastomers against Zoospores of the Green Fouling Alga Ulva (Enteromorpha). *Biofouling* **2004**, *20* (1), 53–63. https://doi.org/10.1080/08927010410001662689.
(133) Efimenko, K.; Finlay, J.; Callow, M. E.; Callow, J. A.; Genzer, J. Development and Testing of Hierarchically Wrinkled Coatings for Marine Antifouling. *ACS Appl. Mater. Interfaces* **2009**, *1* (5), 1031–1040. https://doi.org/10.1021/am9000562.
(134) Stafford, C. M.; Harrison, C.; Beers, K. L.; Karim, A.; Amis, E. J.; Vanlandingham, M. R.; Kim, H. C.; Volksen, W.; Miller, R. D.; Simonyi, E. E. A Buckling-Based Metrology for Measuring the Elastic Moduli of Polymeric Thin Films. *Nat. Mater.* **2004**, *3* (8), 545–550. https://doi.org/10.1038/nmat1175.
(135) Genzer, J.; Groenewold, J. Soft Matter with Hard Skin: From Skin Wrinkles to Templating and Material Characterization. *Soft Matter* **2006**, *2* (4), 310–323. https://doi.org/10.1039/b516741h.
(136) Rodriguez-Hernandez, J. Wrinkled Interfaces: Taking Advantage of Surface Instabilities to Pattern Polymer Surfaces. *Prog. Polym. Sci.* **2015**, *42*, 1–41. https://doi.org/10.1016/j.progpolymsci.2014.07.008.
(137) Bowden, N.; Brittain, S.; Evans, A. G.; Hutchinson, J. W.; Whitesides, G. M. Spontaneous Formation of Ordered Structures in Thin Films of Metals Supported on an Elastomeric Polymer. *Nature* **1998**, *393*, 146–149.
(138) Bowden, N.; Huck, W. T. S.; Paul, K. E.; Whitesides, G. M. The Controlled Formation of Ordered, Sinusoidal Structures by Plasma Oxidation of an Elastomeric Polymer. *Appl. Phys. Lett.* **1999**, *75* (17), 2557–2559. https://doi.org/10.1063/1.125076.
(139) Chandra, D.; Crosby, A. J. Self-Wrinkling of UV-Cured Polymer Films. *Adv. Mater.* **2011**, *23* (30), 3441–3445. https://doi.org/10.1002/adma.201101366.
(140) Guvendiren, M.; Burdick, J. A.; Yang, S. Solvent Induced Transition from Wrinkles to Creases in Thin Film Gels with Depth-Wise Crosslinking Gradients. *Soft Matter* **2010**, *6* (22), 5795–5801. https://doi.org/10.1039/c0sm00317d.
(141) Huang, H.; Chung, J. Y.; Nolte, A. J.; Stafford, C. M. Characterizing Polymer Brushes via Surface Wrinkling. *Chem. Mater.* **2007**, *19* (26), 6555–6560. https://doi.org/10.1021/cm702456u.
(142) Singamaneni, S.; McConney, M. E.; Tsukruk, V. V. Spontaneous Self-Folding in Confined Ultrathin Polymer Gels. *Adv. Mater.* **2010**, *22* (11), 1263–1268. https://doi.org/10.1002/adma.200903052.
(143) Singamaneni, S.; McConney, M. E.; Tsukruk, V. V. Swelling-Induced Folding in Confined Nanoscale Responsive Polymer Gels. *ACS Nano* **2010**, *4* (4), 2327–2337. https://doi.org/10.1021/nn901886y.
(144) Ortiz, O.; Vidyasagar, A.; Wang, J.; Toomey, R. Surface Instabilities in Ultrathin, Cross-Linked Poly(N- Isopropylacrylamide) Coatings. *Langmuir* **2010**, *26* (22), 17489–17494. https://doi.org/10.1021/la1028146.

(145) Brooks, K.; Razavi, M. J.; Wang, X.; Locklin, J. Nanoscale Surface Creasing Induced by Post-Polymerization Modification. *ACS Nano* **2015**, *9* (11), 10961–10969. https://doi.org/10.1021/acsnano.5b04144.

CHAPTER II – SYNTHESIS OF THIOLACTONE POLYMER BRUSH SURFACES: EXPANDING THE DESIGN OF MULTIFUNCTIONAL SURFACES VIA SEQUENTIAL AND ORTHOGONAL REACTIONS

2.1 Introduction

The fabrication of advanced functional polymeric surfaces with well-defined chemical functionalities and complex patterns is critical for various applications, including biosensors,[1,2] antifouling[3] and antibacterial surfaces,[4,5] cell adhesion,[6] mechanical actuation,[7,8] and nanoparticle transduction.[9] However, precise control of the polymer brush architecture, chemical functionality and reactivity, and spatial orientation of functional groups throughout the interface still remains a significant challenge in polymer chemistry. A rapidly growing area to address the aforementioned issues involves post-polymerization modification (PPM) of polymer surfaces.[10–12] PPM is a process based on the polymerization of monomers carrying chemoselective handles that are inert under polymerization conditions, but can subsequently be converted into a broad range of functional groups. Thus, PPM serves as a powerful tool for tailoring the chemical and mechanical properties of polymer brush surfaces.[10–12] The orthogonality of "click" chemistries can be utilized in PPM reactions as a means to introduce multiple distinct functionalities to a surface in a one-pot fashion.[13] A number of "click" reactions have been exploited for surface modification, such as copper catalyzed azide-alkyne cycloadditions (CuAAC),[14–16] activated ester-amine reactions,[17–19] and thiol-based reactions.[20–24] Thiol-click reactions are valuable metal-free alternatives to the heavily exploited CuACC reactions; however, the high reactivity of thiol-containing monomers hinders their use in most polymerization techniques. Hence, there is a growing interest to

expand the thiol-click monomer "toolbox" that enable the immobilization of multifunctional chemistries onto solid substrates by exploiting efficient linking strategies.

In 2011, Du Prez and coworkers reported efficient one-pot multistep reactions based on γ-thiolactone (a cyclic thioester).[25] Thiolactone derivatives have since emerged as a powerful latent thiol functionality for the design of multifunctional materials via orthogonal modifications.[26–28] The thiolactone ring can undergo a nucleophilic ring-opening reaction with primary amines, liberating a thiol that can undergo thiol-coupling chemistries with alkenes, alkynes, maleimides, or acrylates. Thiolactone chemistry has two major advantages compared to other efficient activated-ester chemistries employed in PPM reactions. First, thiolactone reactions exhibit 100 % atom-efficiency since no atoms are wasted. In addition, this double modification strategy can be performed in an efficient one-pot reaction enhancing simple experiments and accelerated PPM reactions. Du Prez and others[29–31] have demonstrated the potential for thiolactone chemistry and the design for new polymeric architectures, with a recent focus on sequence-controlled polymers.[32] However, thiolactone chemistry remains an underutilized synthetic platform for polymer surfaces. In one example, Belbekhouche et al. grafted polythiolactones onto gold surfaces and employed reversible redox chemistry with the thiol moieties.[33] The lack of examples in literature exploiting thiolactone derivatives for surface-initiated polymerization and PPM reactions is surprising considering their potential for surface engineering.

Herein, we demonstrate a versatile post-polymerization modification strategy to synthesize multifunctional polymer brush surfaces based on poly(acrylamide-homocysteine thiolactone) (pAHT). pAHT is synthesized via radical-mediated microwave-assisted surface-initiated polymerization (μW-SIP).[34] Modification of the

brush surfaces with a library of amines generates a reactive thiol precursor, which is available to undergo a sequential base-catalyzed thiol-Michael reaction with functional acrylates and maleimides. Additionally, we employ a one-pot double modification reaction to demonstrate the versatility of thiolactone chemistry as a powerful PPM platform for polymer brush surfaces. X-ray photoelectron spectroscopy depth profile experiments provided key insight into the PPM efficiency (e.g. sequential versus one-pot reactions) of the pAHT brushes. Finally, we exploit reactive microcontact printing (μCP) with fluorescent post-modifiers to design multifunctional, micropatterned, fluorescent surfaces.

2.2 Experimental Section

2.2.1 Materials

D,L-homocysteine thiolactone hydrochloride (99 %) was purchased from Alfa Aesar and used as received. Triethylamine (TEA), 1,8-diazabicyclo(5.4.0)undec-7-ene (DBU), 2-hydroxylethyl acrylate (HEA), dansylcadaverine, 4-bromobenzylamine (BBA), ethanolamine (EA), and hexylamine (HA) were purchased from Sigma-Aldrich and used as received. *1H,1H*-Perfluoro-*N*-decyl acrylate (FA) was purchased from Gelest. Texas Red® C2 maleimide was purchased from Introgen. Silicon wafers (orientation <100>, native oxide) were purchased from University Wafer. The PDMS stamp (5 μm lines spaced by 10 μm) was purchased from Research Micro Stamps. An azo-based trichlorosilane initiator for surface-initiated polymerization was synthesized per literature procedures.[34,35]

2.2.2 Instrumentation and characterization

Ellipsometry measurements were carried out using a Gartner Scientific Corporation LSE ellipsometer with a 632.8 nm laser at 70° from the normal. Multiple thickness measurements were taken for each sample to determine the uncertainty in the measurements. Grazing-angle attenuated total reflectance FTIR (gATR-FTIR) analysis was carried out using a Thermo Scientific FTIR (Nicolet 8700) equipped with a VariGATR™ accessory (grazing angle 65°, germanium crystal; Harrick Scientific). Spectra were collected with a resolution of 4 cm^{-1} by accumulating a minimum of 128 scans per sample. All spectra were collected while purging the VariGATR™ attachment and FTIR instrument with nitrogen along the infrared beam path to minimize the peaks corresponding to atmospheric water and CO_2. Spectra were analyzed and processed using Omnic software. Static water contact angles (WCA) were measured using 6 μL water droplets on a Rame-hart goniometer. All μW-SIP reactions were carried out in a mono-mode micro-wave reactor (CEM Corporation Discover S Class) with a calibrated infrared temperature sensor in constant power mode with simultaneous cooling to maintain the desired temperature. XPS measurements were performed using a Kratos AXIS Ultra DLD Spectrometer (Kratos Analytical, Manchester, UK) with a monochromatic Al K X-ray source (1486.6 eV) operating at 150 W under 1.0 x 10^{-9} Torr. Measurements were performed in hybrid mode using electrostatic and magnetic lenses, and the pass energy of the analyzer was set at 20 eV for high-resolution spectra and 160 eV for survey scans, with energy resolutions of 0.1 eV and 0.5 eV, respectively. Generally, total acquisition times of 180 s and 440 s were used to obtain high-resolution and survey spectra, respectively. All XPS spectra were recorded using the Kratos Vision II software; data

files were translated to VAMAS format and processed using the CasaXPS software package (v. 2.3.12). Binding energies were calibrated with respect to C 1s at 285 eV. Depth profile experiments were performed using a Thermo-Fisher ESCALAB Xi+ X-ray photoelectron spectrometer with a monochromatic Al X-ray source (1486.6 eV). A 6000 eV cluster gun with a cluster size of 300 at a 0° incidence angle was rastered over a 2 mm x 2 mm area to create the depth profile. Depth profile spectra were recorded using the Thermo Scientific Avantage software; data files were translated to VGD format and processed using the Thermo Avantage v5. 9904 package. Fluorescent microscopy was conducted on a Zeiss LSM 710 laser confocal scanning microscope running Zen Black software and a λ = 405 nm and 633 nm argon laser.

2.2.3 Cleaning of silicon wafers

Silicon wafers were cut into 1 cm × 1 cm pieces and cleaned using the RCA procedure to remove organic residue and oxidize the surface of the wafer. The general recipe for RCA cleaning is 5 parts DI water, 1 part 27 % ammonium hydroxide, and 1 part 30 % hydrogen peroxide. DI water and ammonium hydroxide were added to a test tube and heated to 70 °C for 5 minutes, and then the test tube was removed from heat and hydrogen peroxide was added. The solution bubbled vigorously after 1-2 minutes, indicating that it was ready to use. The silicon wafer was transferred to the test tube and heated at 70 °C for 15 minutes. After 15 minutes, the wafer is removed from the solution and washed multiple times with DI water. Clean substrates were stored in an oven at 120 °C before initiator functionalization.

2.2.4 Immobilization of initiator onto silicon substrates

An azo-based trichlorosilane initiator was synthesized according to literature procedures.[35,36] Clean silicon substrates were transferred into a dry, septum sealed test tube containing a toluene solution of azo-initiator (4 mmol, 13 mL) and triethylamine (TEA) (0.2 mL). The immersion time was 1 h. Substrates were then removed, rinsed with toluene, methanol, and DI water and dried under a stream of nitrogen. If not used immediately, initiator functionalized substrates were stored in the dark at −20 °C in toluene.

2.2.5 Synthesis of thiolactone acrylamide (TlaM) monomer

Thiolactone acrylamide (TlAm) monomer was synthesized following a procedure reported by Reinicke and coworkers.[37] An ice-cooled solution of D,L-homocysteine thiolactone hydrochloride (5.0 g, 32.5 mmol) in H_2O/1,4-dioxane (1/1, 70 mL) was treated with $NaHCO_3$ (13.66 g, 162.7 mmol) and stirred for 30 minutes at 0 °C. Acryloyl chloride (5.8 g, 65.1 mmol) was added to the mixture dropwise and the reaction mixture was allowed to reach room temperature overnight. Brine (70 mL) was added and the mixture was extracted with EtOAc (3 x 150 mL). The collected organic fractions were dried with Na_2SO_4 and the solvent was removed. The crude residue was purified by recrystallization from dichloromethane, yielding TlAm as a white, crystalline solid (4.1 g, 82 %). ^{1}H NMR (300 MHz, DMSO-d_6) δ (ppm): 8.43-8.49 (*d*, NH), 6.05-6.30 (*m*, 2H), 5.60-5.68 (*dd*, 1H), 4.62-4.75 (*ddd*, 1H), 3.26-3.50 (*m*, 2H), 2.40-2.50 (*m*, 1H), 2.0-2.17(*m*, 1H). ^{13}C NMR (300 MHz, DMSO- d_6) δ (ppm): 205 (C=O), 165.0 (C=O), 131.5 (CH) 126.6 (CH_2), 58.2 (CH), 30.6 (CH_2), 27.5 (CH_2).

2.2.6 Microwave-assisted surface-initiated polymerization of pAHT brush

A substrate with the azo-based initiator was placed in a sealed microwave vial and purged with nitrogen. In a separate Schlenk tube, acrylamide homocysteine thiolactone monomer was dissolved in anhydrous DMSO (0. 5 M, 1 M, 1.5 M, and 2 M) and the solution was subjected to three freeze-pump-thaw cycles. For each polymerization, 1.5 mL of the degassed monomer solution was transferred via cannula into the microwave vial containing the substrate. Polymerizations were carried out in the DMSO solution, placed into the microwave reactor, and irradiated at a fixed power of 60 W for 15 minutes with simultaneous cooling to maintain the reaction temperature at 110 °C. The substrates were extensively sonicated in DMSO (e.g. 10 s cycles) to remove any physisorbed polymer from the surfaces. This washing process was continued until no change in brush thickness could be measured.

2.2.7 PPM of pAHT brush with amines

The pAHT brushes were post-modified with 4-bromobenzylamine (BBA), ethanolamine (EA), and hexylamine (HA). A pAHT substrate was placed in a solution of the amine (0.15 M) in DMSO with 3 equivalents of TEA in a sealed test tube under a nitrogen atmosphere. The reaction was allowed to react overnight to ensure completion. Reaction completion was determined by the disappearance of the cyclic thiolactone carbonyl group at 1669 cm^{-1} and a shift of the amide C=O stretch to lower wavenumbers (1649 cm^{-1}). The substrate was then removed, thoroughly rinsed with DMSO, and dried with nitrogen.

2.2.8 PPM of amine-modified pAHT brush with base catalyzed thiol-Michael reactions

All thiol-click reactions were performed under ambient air, temperature and humidity conditions. Base-catalyzed thiol-Michael reactions were conducted with *1H*,1*H*-perfluoro-*N*-decyl acrylate (FA), 2-(perfluorobutyl) ethyl acrylate (FEA), and 2-hydroxyethyl acrylate (HEA). Substrates were placed in a 0.15 M solution in acetone with DBU (0.022 mol L^{-1}) unless stated otherwise (e.g. DMSO solvent for HEA). Reactions were conducted overnight, only to ensure complete reaction. Reaction completion was determined by ellipsometry measurements (e.g. no further increase in brush thickness). The brushes were thoroughly rinsed with acetone, DMSO, and dried with a stream of nitrogen.

2.2.9 pAHT one-pot double modification reactions

A pAHT substrate was placed in a solution of amine (0.15 M) and acrylate (0.15 M) in DMSO with DBU (0.022 mol L^{-1}). Reactions were conducted overnight, only to ensure complete reaction. Reaction completion was determined by ellipsometry measurement (e.g. no further increase in brush thickness). The brushes were thoroughly rinsed with acetone, DMSO and dried with a stream of nitrogen.

2.2.10 Post-polymerization modification via reactive microcontact printing

A thiolactone brush was placed in a solution of dansylcadaverine (12 mM) in EtOH with DBU (10 mM) for 15 h to ensure full conversion. Then, a freshly oxidized PDMS stamp was inked with Texas Red® C2 maleimide (25 mM) in EtOH for 1 min, dried with nitrogen, and pressed onto the polymer brush surface for 1 h. The patterned surface was thoroughly rinsed and sonicated in EtOH.

2.3 Results and Discussion

2.3.1 Synthesis of pAHT polymer brush surface

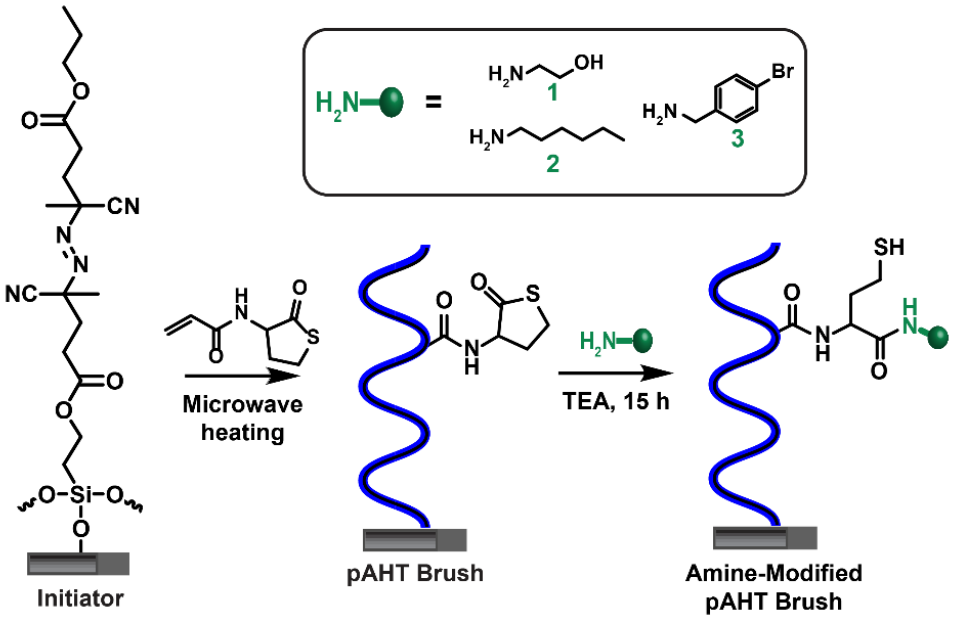

Scheme 2.1 Synthesis of pAHT brushes (≈ 40nm) and post-modification with amines: (1) ethanolamine (EA), (2) hexylamine (HA), and (3) 4-bromobenzylamine (BBA).

The thiolactone acrylamide monomer used for polymerization was prepared by reacting acryloyl chloride with *D,L*-homocysteine thiolactone hydrochloride.[37] Scheme 2.1 shows the synthetic strategy for the preparation of poly(acrylamide-homocysteine thiolactone) (pAHT) brushes via microwave-assisted surface-initiated polymerization (μW-SIP) from an azo-based silane initiator on a silicon substrate.[34] The average thickness of the azo-based initiator layer was 2.2 ± 0.1 nm as measured by ellipsometry. The pAHT brushes were synthesized via μW-assisted conventional free-radical polymerization since it is a simple and well-studied route to design polymer brush surfaces.[34] Polymerizations were carried out in dimethyl sulfoxide (DMSO) under

constant microwave power (60 W) with simultaneous cooling to maintain the reaction temperature at 110 °C.

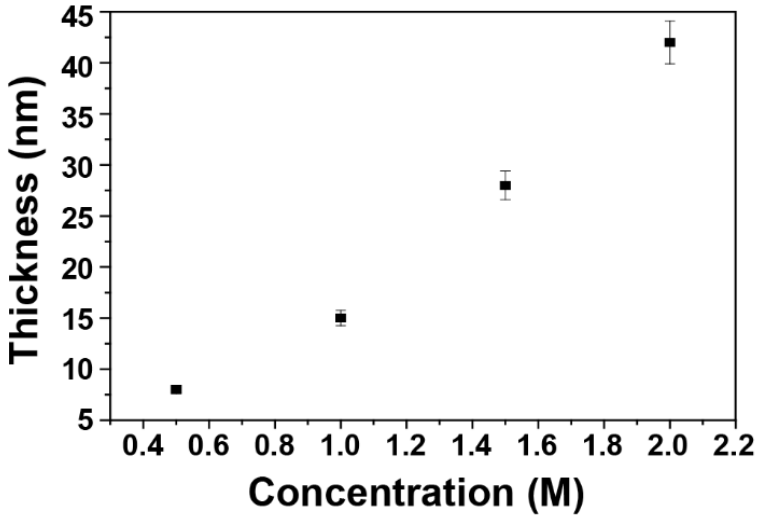

Figure 2.1 Brush thickness versus monomer concentration for pAHT brush surfaces (DMSO, 60 W, 110 °C, 15 minutes).

pAHT polymer brush thickness as a function of thiolactone acrylamide monomer concentration was investigated for the μW-SIP process. For conventional free radical SIP, the relationship between brush thickness and monomer concentration at a constant reaction time generally exhibits a linear relationship.[17] However, for μW-SIP, Guo et al. observed linear and nonlinear relationships between film thickness and monomer concentration, depending on the polarity of the monomer and solvent, respectively.[34] For example, when utilizing a polar monomer in a non-polar solvent (or vice versa) there is an interplay between monomer concentration and the change in polarity of the monomer/solvent reaction mixture that influences brush thickness. At low monomer concentrations, the polymer brush thickness is governed by the low concentration and the relatively non-polar reaction mixture, which decreases the ability of microwave radiation to excite polar molecules. At higher monomer concentrations, the high polarity of the

reaction mixture absorbs microwave radiation more efficiently, leading to minimal brush growth. This discrepancy leads to a nonlinear relationship between brush film thickness and monomer concentration. Conversely, when using a polar monomer in a polar solvent, the change in polarity of the monomer/solvent mixture with increasing monomer concentration is negligible, and μW-SIP exhibits a traditional relationship between brush thickness and monomer concentration. Thus, the polar nature of both the thiolactone acrylamide monomer and the solvent (DMSO) lead to a traditional linear relationship between brush thickness and monomer concentration (Figure 2.1). Hereafter, pAHT brushes with a target brush thickness of approximately 40 nm were synthesized and employed for post-polymerization modification (PPM) reactions. The chemical composition of the pAHT brush was characterized using gATR-FTIR and XPS. Figure 2.2a shows the gATR-FTIR spectrum for pAHT with a broad peak at 1669 cm^{-1} attributed to an overlap of the carbonyl stretch of the five-membered thiolactone ring and the amide I group.[28,38] The peak at 1536 cm^{-1} is indicative of the amide II N-$H_{bending}$ stretching vibration.[39]

2.3.2 Post-polymerization modification and sequential click reactions

The pAHT brush provides a versatile platform for modular post-polymerization modification (PPM) reactions with primary amines. Three amines were selected for PPM; ethanolamine (EA), 4-bromobenzylamine (BBA), and hexylamine (HA) (Scheme 2.1). Modification reactions were conducted in DMSO in the presence of triethylamine (TEA) under a nitrogen atmosphere. The progress of the PPM reaction was monitored by gATR-FTIR through the disappearance of the cyclic thiolactone carbonyl group at 1669 cm^{-1} (Figure 2.2a) and a shift of the amide C=O stretch to lower wavenumbers (1649 cm^{-1})

(Figure 2.2b-c). Furthermore, brushes modified with EA exhibit a broad peak centered at 3300 cm^{-1} consistent with the hydroxy group (Figure 2.2b) and sharp peaks at 2864 cm^{-1} and 2931 cm^{-1} attributed to the HA aliphatic C-H groups (Figure 2.2c). The formation of the thiol upon aminolysis could not be monitored by gATR-FTIR due to a weak S-H stretching vibration in the region of 2540-2600 cm^{-1}.[39] Surface wettability changed with varying amine modifier functionality. For example, the water contact angle (WCA) of the unmodified pAHT brush decreased from 55.6 ± 1.7° to 44.2 ± 1.3° upon modification with ethanolamine due to the incorporation of the hydroxy moiety. Similarly, the pAHT brush modified with hexylamine became more hydrophobic (WCA = 76.8 ± 1.8°) after modification due the aliphatic C-H groups. In the case of the pAHT-BBA modified brush, this sequence of reactions provides elemental handles that X-ray photoelectron spectroscopy (XPS) can readily probe to follow the PPM reaction and will be discussed in later sections.

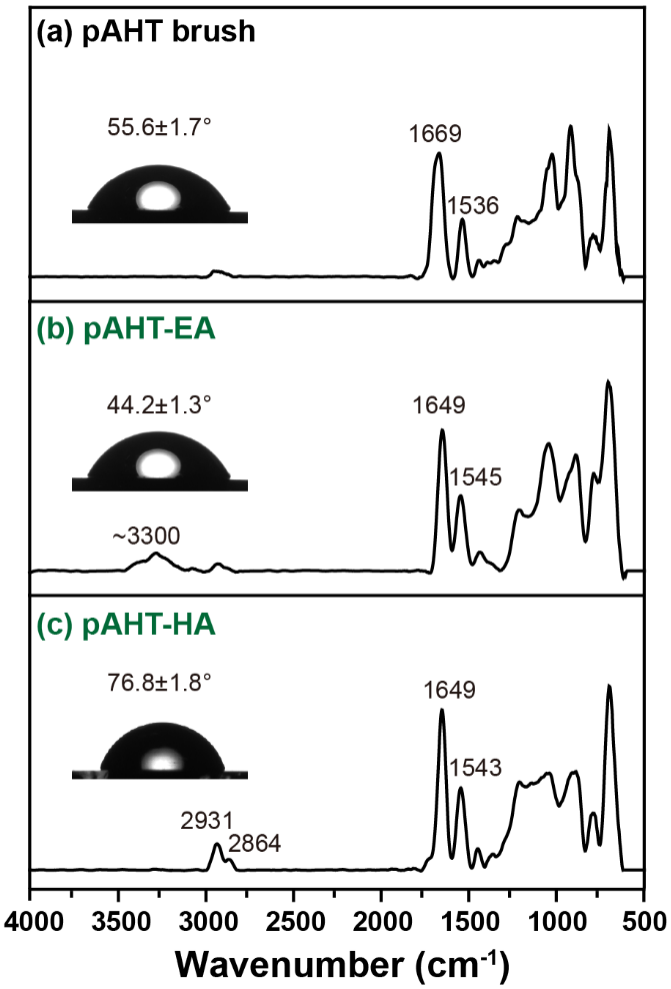

Figure 2.2 gATR-FTIR of (a) pAHT brush and pAHT brush modified with (b) EA and (c) HA. Inset images show the static water contact angle for each surface.

The modification of pAHT with various amines increases the molecular weight of the repeat units, resulting in an increase in polymer brush thickness. The thickness values of the pAHT brush before and after PPM were measured using ellipsometry and the results are summarized in Table 2.1. Equation 1 describes the relationship between polymer brush thickness (T), the molecular weight of the polymer repeat unit (M), and the mass density (ρ) of the polymer brush before and after modification,[17]

$$\frac{T_2}{T_1} = \frac{M_2 \rho_1}{M_1 \rho_2} \qquad \text{Equation 1}$$

where the subscripts 1 and 2 represent the unmodified and amine-modified pAHT brush, respectively. Assuming equivalent mass density of the pAHT brush before and after PPM, Equation 1 becomes Equation 2, where k denotes conversion and M_{PPM} represents the molecular weight of the post-modifier that reacts on the polymer brush chain, respectively.

$$\frac{T_2}{T_1} = \frac{M_2}{M_1} = \frac{M_1 + kM_{PPM}}{M_1} \qquad \text{Equation 2}$$

Rearrangement of Equation 2 allows the amine conversion k to be calculated according to Equation 3,

$$k = \frac{M_1}{M_{PPM}}\left(\frac{T_2}{T_1} - 1\right) \qquad \text{Equation 3}$$

and the results are shown in Table 2.1. Modification of pAHT with EA and HA modifiers increased the brush thickness from approximately 38 nm and 37 nm to 52 and 60 nm after PPM, respectively, which indicates the thiolactone aminolysis reaction proceeds to > 98 % conversion. PPM with BBA increased the brush thickness from 30 nm to 42 nm modification, resulting in a 35 % thiolactone conversion. The lower conversion observed for BBA could be attributed to the stereo-electronic properties of the primary amine. Similar results have been observed by Espeel et al.[28]

Table 2.1 Brush thickness and conversion of the unmodified pAHT brush, amine-modified pAHT, sequential thiol-functionalized pAHT, and one-pot double modification of pAHT brush surfaces.

pAHT Modified Brush	Thickness (nm)			Amine conversion (%)	Thiol conversion (%)
	pAHT unmodified	pAHT after aminolysis	pAHT after thiol-ene		
EA-FEA	38 ± 0.2	52 ± 0.1	72 ± 0.2	98 ± 2	40 ± 2
EA-FEA one-pot	30 ± 0.1	-	91 ± 0.1	-	91 ± 2
HA-HEA	37 ± 0.1	60 ± 0.1	70 ± 0.1	99 ± 3	70 ± 2
HA-HEA one-pot	40 ± 0.1	-	87 ± 0.3	-	92 ± 2
BBA-FA	30 ± 0.1	42 ± 0.2	69 ± 0.2	35 ± 2	41 ± 1
BBA-FA one-pot	30 ± 0.1	-	100 ± 0.3	-	74 ± 2

After post-modification with amines, the exposed thiol moieties serve as reactive handles for thiol-mediated click reactions. As illustrated in Scheme 2.2, base catalyzed thiol-Michael modifications were exploited with electron deficient alkenes using 1,8-diazabicyclo(5.4.0)undec-7-ene (DBU) as the catalyst. Three acrylates were selected for the thiol-Michael PPM reactions; *1H,1H*-perfluoro-*N*-decyl acrylate (FA), 2-(perfluorobutyl)ethyl acrylate (FEA), and 2-hydroxyethyl acrylate (HEA).

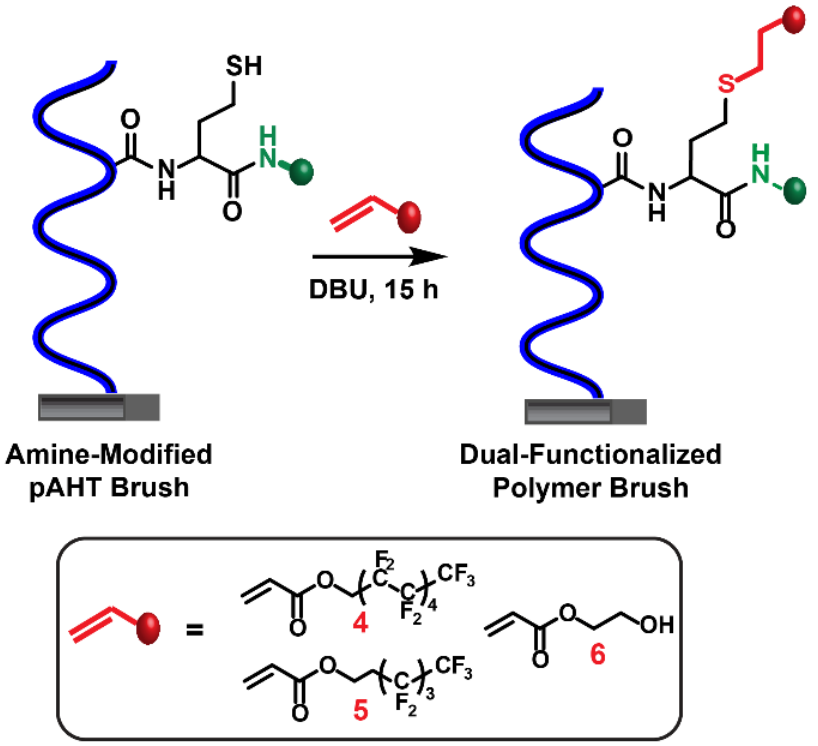

Scheme 2.2 Amine-modified pAHT brush and subsequent thiol-Michael addition with acrylates (4) 1*H*, 1*H*-perfluoro-*N*-decyl acrylate (FA), (5) 2-(perfluorobutyl)ethyl acrylate (FEA), and (6) 2-hydroxyethyl acrylate (HEA).

Figure 2.3a-b shows the FTIR spectrum for the following reactions: pAHT-EA followed by sequential reaction with FEA, and pAHT-HA followed by sequential reaction with HEA, respectively. pAHT-EA brushes modified with FEA show peaks around 1226 cm^{-1} and 1136 cm^{-1} consistent with the C-F stretch (Figure 2.3a). Furthermore, pAHT-HA modified brushes reacted with HEA show a broad peak at 3400 cm^{-1} consistent with the hydroxyl group of HEA (Figure 2.3b). All spectra show peaks around 1731 cm^{-1} which correspond to the ester C=O stretch. Static WCA experiments were conducted for each brush modification and are shown as insets in Figure 2.3. The expected changes in wettability are associated with each functionality moiety. For example, surfaces modified with FEA exhibited hydrophobic wetting characteristics

(WCA = 91.7 ± 2.3°) due to the fluorinated functional groups and surfaces modified with HEA exhibited hydrophilic wetting characteristics (WCA = 52.2 ± 1.3°) due to the hydroxy moieties.

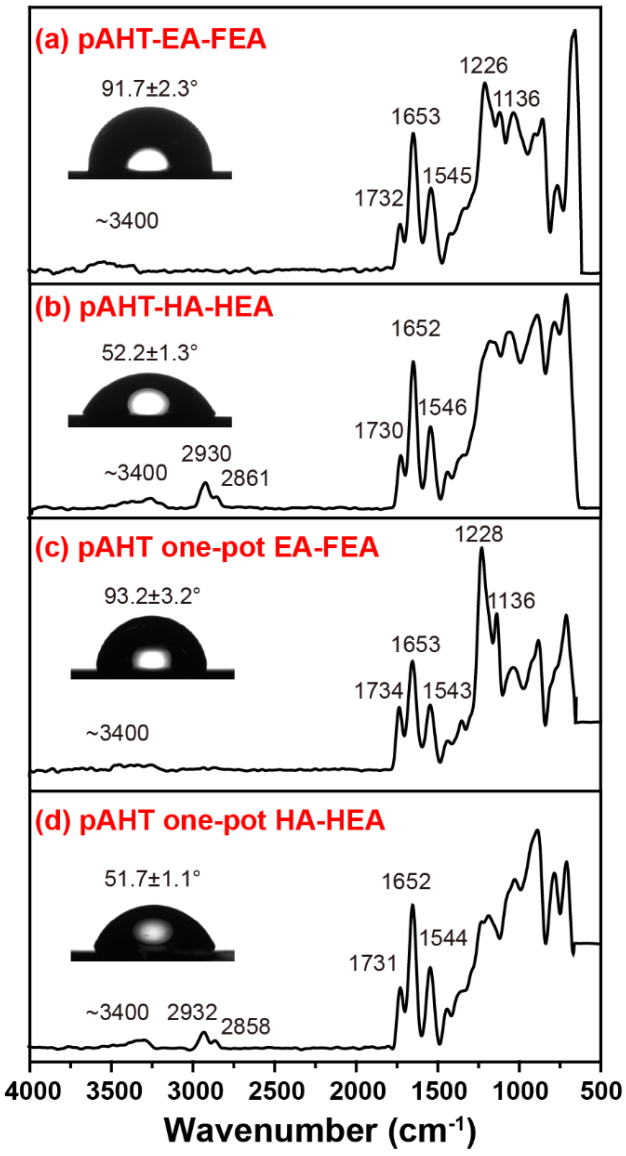

Figure 2.3 gATR-FTIR of amine-modified pAHT brush and sequential thiol-ene modification with (a) FEA and (b) HEA. One-pot double pAHT modification with (c) EA/FEA and (d) HA/HEA. Inset images show the static water contact angle.

Thiol-Michael conjugation conversions calculated from the increase in brush thickness after the sequential modification are summarized in Table 2.1. Sequential PPM of pAHT-EA brushes with FEA resulted in a change in thickness from 52 nm to 72 nm, indicating a 40 % thiol conversion. PPM of pAHT-HA brushes with HEA exhibited a change in thickness from 60 nm to 70 nm, resulting in a 70 % thiol conversion. Modification of pAHT-BBA brushes with FA increased the brush thickness from 42 nm to 69 nm, indicating the thiol-ene reaction proceeded to 41 %. Lower conversions for the thiol-ene reactions could be attributed to low miscibility of the FA and FEA perfluoroalkyl chain with the thiol-modified brush.[40] Furthermore, the low thiol-ene conversions can be attributed to the steric bulkiness of the amine-modified pAHT brush, which hinders the acrylates from reacting with the free thiols.[41,42]

To complement the gATR-FTIR data, XPS was utilized to characterize the products of the pAHT aminolysis reaction with BBA and subsequent thiol-ene reaction with FA. Figure 2.4 shows the survey and corresponding high-resolution spectra for the S2p, Br3d, and F1s for the pAHT brush post-modified with BBA and sequential thiol-Michael addition with FA. As shown in Figure 2.4a, peaks at C1s (285 eV), O1s (531 eV), N1s (400 eV), S2s (229 eV), and S2p (163.4 eV) confirms successful μW-SIP of pAHT. After μW-SIP, the pAHT brush was post-modified with BBA; the XPS spectrum of this surface showed characteristic peaks associated with the bromine (Br3d, 70 eV; Br3p, 182 eV; Br3s, 257 eV, Figure 2.4b). The pAHT-BBA modified brush was then exposed to a base-catalyzed thiol-Michael reaction with FA. The XPS spectrum for the pAHT-BBA brush modified with FA exhibited a characteristic F1s peak at 698 eV (Figure 2.4c).

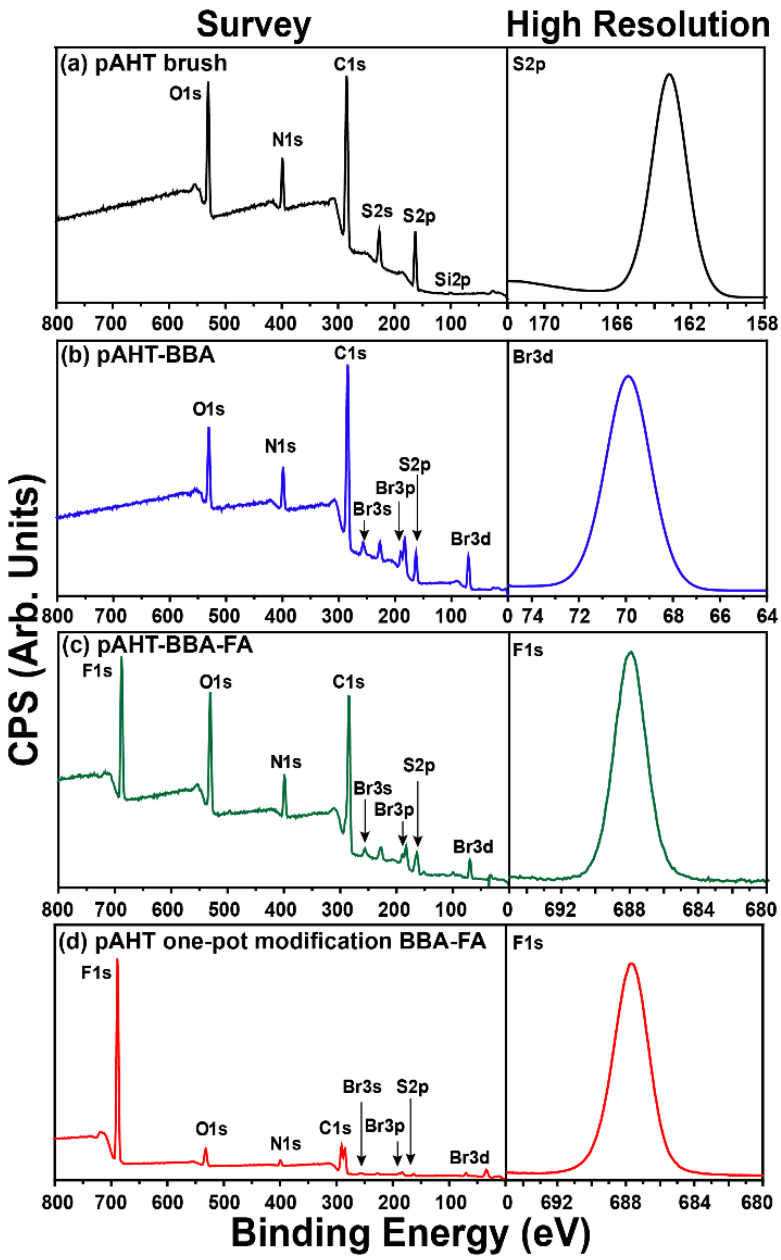

Figure 2.4 Survey and S2p, Br3d, and F1s high-resolution XPS spectra for (a) pAHT brush, (b) pAHT brush modified with 4-bromobenzyl amine (BBA), (c) pAHT-BBA clicked with *1H,1H*-perfluoro-*N*-decyl acrylate (FA), and (d) pAHT one-pot double modification with BBA and FA.

Next, depth profiling with argon ion cluster sputtering was performed to investigate the pAHT brush homogeneity and PPM efficiency (e.g. sequential versus one-pot reactions). Depth profile experiments were conducted using a 6000 eV cluster gun

with a cluster size of 300 at a 0° incidence angle. Generally, XPS depth profile experiments at a 0° incidence angle result in a lower depth resolution, which may effectively smear the atomic concentration profiles.[43,44] The atomic concentrations were recorded as a function of sputter time. Sputter time was converted to depth (nm) with knowledge of the sputter rate and the overall brush thickness for each sample. Figure 2.5a shows the depth profile for the unmodified pAHT brush, where the chemical composition of the S2p remains relatively constant for the full thickness of the pAHT brush. The C1s and Si2p intersection are indicative of the polymer brush/silicon substrate interface. For the pAHT-BBA brush, the Br3d atomic percent as a function of depth indicates that the distribution of BBA is largely homogenous throughout the modified brush (Figure 2.5b), which indicates that BBA readily reacts with the pAHT brush. The relatively low atomic composition (~ 2 %) of Br3d and a brush/silicon interface at approximately 40 nm is attributed to the low aminolysis conversion observed in Table 2.1. Upon sequential modification of pAHT-BBA with FA, the F1s peak exhibited a 10 % atomic concentration (Figure 2.5c). The low atomic percent could be attributed to the steric bulkiness of the BBA-modified pAHT brush, which limits the FA from reacting with the thiol to quantitative conversion.[41,42] Furthermore, the F1s atomic composition as a function of depth indicates the distribution of FA is homogenous throughout the modified brush surface.

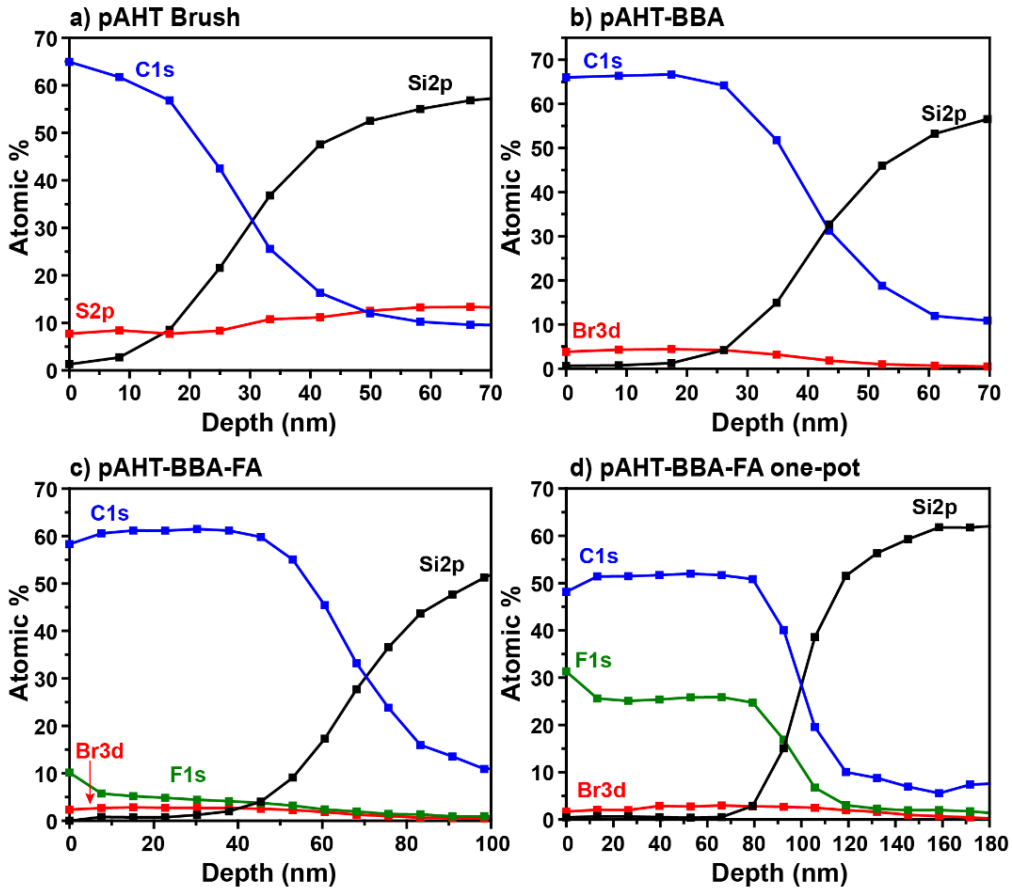

Figure 2.5 Depth profiles of (a) unmodified pAHT, (b) pAHT-BBA, (c) pAHT-BBA-FA, and (d) one-pot modification of pAHT with BBA-FA. C1s, Si2p, S2p, Br3d, and F1s atomic percent as a function of brush depth.

2.3.3 One-pot double modification for dual-functionalized pAHT brush surfaces

After investigating the sequential PPM reactions of pAHT brush surfaces, we exploited the efficacy of one-pot reactions for a simple route to produce dual-functional polymer brush surfaces. We demonstrate the applicability of the one-pot double modification using the chemistries previously described. Specifically, we subjected a pAHT substrate to individual solutions of EA/FEA (1:1), HA/HEA (1:1), and BBA/FA (1:1) with DBU under nitrogen for 15 h, respectively (Scheme 2.3). The one-pot double modification reactions were characterized via gATR-FTIR and XPS. Figure 2.3 shows

the gATR-FTIR spectra for the dual-functionalized pAHT brush surfaces for the pAHT-EA-FEA and pAHT-HA-HEA brush scaffolds. Figure 2.3c shows a broad centered peak at 3400 cm^{-1} corresponding to the hydroxy group of EA and a peak at 1205 cm^{-1} attributed to the C-F stretch of the FEA group. Figure 2.3d shows a broad centered peak at 3400 cm^{-1} corresponding to the hydroxy group of HEA and sharp peaks at 2937 cm^{-1} and 2858 cm^{-1} attributed to the HA aliphatic C-H groups. The one-pot double modification conversions are summarized in Table 2.1. The one-pot reactions result in a substantial increase in brush thickness compared to the sequential PPM reactions with near quantitative conversions (> 91 %). The one-pot double modification of pAHT with EA-FEA exhibited a change in thickness from 30 nm to 91 nm, resulting in a 91 % conversion, compared to a 40 % conversion for the sequential reactions. Furthermore, the pAHT-HA-HEA one-pot reaction resulted in a change in thickness from 40 nm to 87 nm, indicating a 92 % conversion, compared to the 70 % conversion for the sequential PPM reaction. The products of the pAHT-BBA-FA one-pot reaction resulted in a change in thickness from 30 nm to 100 nm, resulting in a 74 % conversion, compared to the 41 % conversion for the sequential reactions.

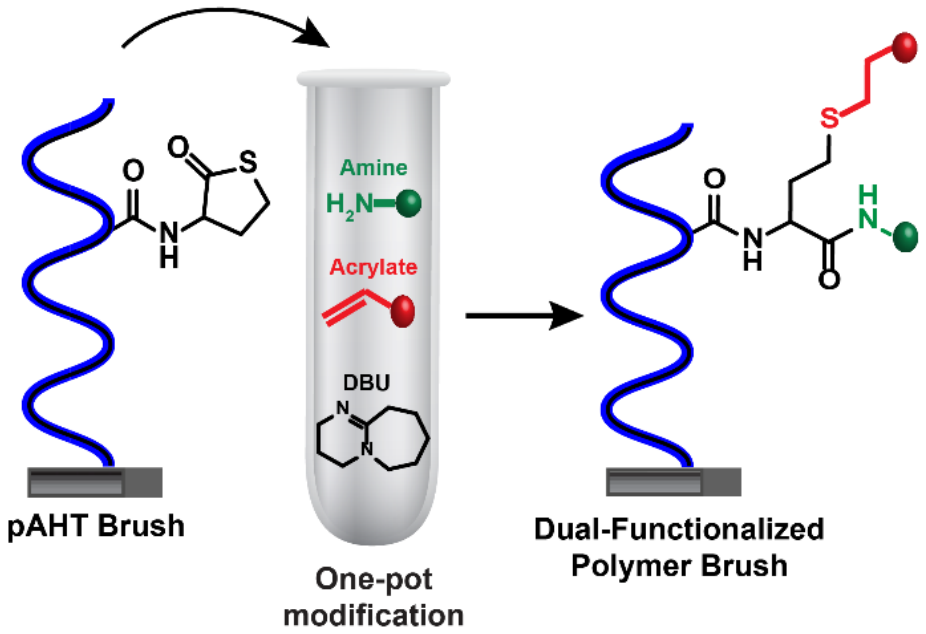

Scheme 2.3 One-pot double modification of pAHT brush via amine-thiol-ene conjugation to design dual functionalized polymer brush surfaces.

The products of the pAHT-BBA-FA one-pot double modification were followed via XPS. Figure 2.4d shows the characteristic bromine (Br3d, 70 eV; Br3p, 182 eV; Br3s, 257 eV) and fluorine peaks (F1s, 698 eV), indicating a successful one-pot double modification reaction. In addition, the depth profile of the one-pot reaction showed a substantial increase in F1s atomic composition (~ 30 %, Figure 2.5d) compared to the sequential modification reaction (~ 10%, Figure 2.5c). The difference in XPS depth profiles between the sequential and one-pot double modification reactions corroborates the conversion data in Table 2.1. We hypothesize that during the sequential PPM reaction, the bulky BBA side chains on the pAHT brush hinders the bulky FA post-modifiers from reacting with the accessible thiol groups.[41,42] Whereas, during the one-pot PPM reaction, the swollen pAHT brush allows an enhanced diffusion of both post-modifiers throughout the brush structure, thereby increasing the accessibility of the thiol

moieties formed upon aminolysis. Hence, we postulate that the increased availability of thiols increases the probability of the FA molecules to undergo thiol-ene reactions, resulting in a higher thiol-ene conversion. This hypothesis can be investigated by quantifying the F1s:Br3d atomic ratio of the sequential PPM and one-pot modification reactions, respectively. For example, Table 2.2 shows distinct differences in the F1s and Br3d atomic ratios of the pAHT-BBA-FA sequential and one-pot PPM reactions. The pAHT-BBA-FA sequential modified brush exhibited a F1s and Br3d atomic % of 81.26 % and 18.74 %, respectively. From these values, the F1s:Br3d atomic ratio is 4.33:1 and the normalized ratio of F1s:Br3d is 1:4.38 (e.g. 19 fluorine atoms per every FA molecule as shown in Scheme 2.2). These results indicate that there is approximately one FA post-modifier per four pAHT-BBA repeat units. Therefore, the F1s:Br3d ratio explains the lower F1s atomic % observed in the pAHT-BBA-FA sequential PPM depth profile in Figure 2.5c. Conversely, the pAHT-BBA-FA one-pot modification exhibited an F1s and Br3d atomic % of 94.95 % and 5.05 %, respectively. The atomic % values result in an atomic F1s:Brd ratio of 18.99:1 and a normalized F1s:Br3d ratio of 1:1 for the one-pot reaction, indicating that there is one FA molecule per every pAHT-BBA repeat unit. Thus, the 1:1 F1s:Br3d ratio supports the higher F1s atomic % in the one-pot modified pAHT-BBA-FA brush depth profile observed in Figure 2.5d.

Table 2.2 Atomic %, atomic ratios, and normalized ratios of F1s and Br3d in the pAHT-BBA-FA sequential and one-pot PPM reactions

pAHT-modified Brush	F1s Atomic %	Br3d Atomic %	F1s:Br3d Atomic Ratio	F1s:Br3d Normalized Ratio[a]
pAHT-BBA-FA sequential	81.26	18.74	4.33:1	1:4.38
pAHT-BBA-FA one-pot	94.95	5.05	18.99:1	1:1

[a]19 fluorine atoms in FA according to scheme 2.2

More importantly, these results validate the influence of steric constraints during the post-polymerization modification reaction, which dictates the overall through-thickness brush composition.[41,42] These observations provide further evidence that the one-pot double modification reaction serves as a more efficient approach than the sequential modification reaction to prepare multi-functional pAHT brush architectures.

2.3.4 Patterning pAHT brush surfaces

Polymeric materials which exhibit spatially defined, complex chemistries and morphologies are advantageous in applications including cell selective adhesion,[45,46] microfluidics,[47] and organic solar cell devices.[48] In particular, microcontact printing (μCP) represents a straightforward, low-cost technique to design micro- and nanostructured surfaces.[49] Here, we demonstrate the pAHT brush platform to design micropatterned surfaces via reactive μCP using two different fluorescent dyes, one bearing a primary amine and the other a maleimide functionality. First, the pAHT brush was fully post-modified with a primary amine, dansylcadaverine, to install the dye and liberate the thiol moiety. After thorough washing, a PDMS stamp (5 μm lines spaced by

10 μm) was inked with Texas Red C2 maleimide (10 mM) in EtOH, dried with nitrogen, and placed in contact with the surface for 1 h (Figure 2.6a). After the functionalization via μCP, the substrate was sonicated in EtOH and the patterned surface was investigated using confocal microscopy. Excitation of dansylcadaverine at 405 nm revealed a fully modified pAHT brush surface (Figure 2.6b). The faint patterned lines in Figure 2.6b may be due to secondary excitation of Texas Red by the dansylcadaverine fluorescence, which overlaps with the wavelength of light known to excite Texas Red. The inset image in Figure 2.6b shows a pAHT brush fully modified with dansylcadaverine without functionalization of Texas Red via μCP. Changing the excitation wavelength to 633 nm resulted in the observation of horizontal stripes caused by the fluorescence of Texas Red C2 maleimide (Figure 2.6c). When both dyes were excited simultaneously, the surface exhibits patterns with high resolution and fidelity (Figure 2.6d), demonstrating the efficiency of the thiol-ene modification.

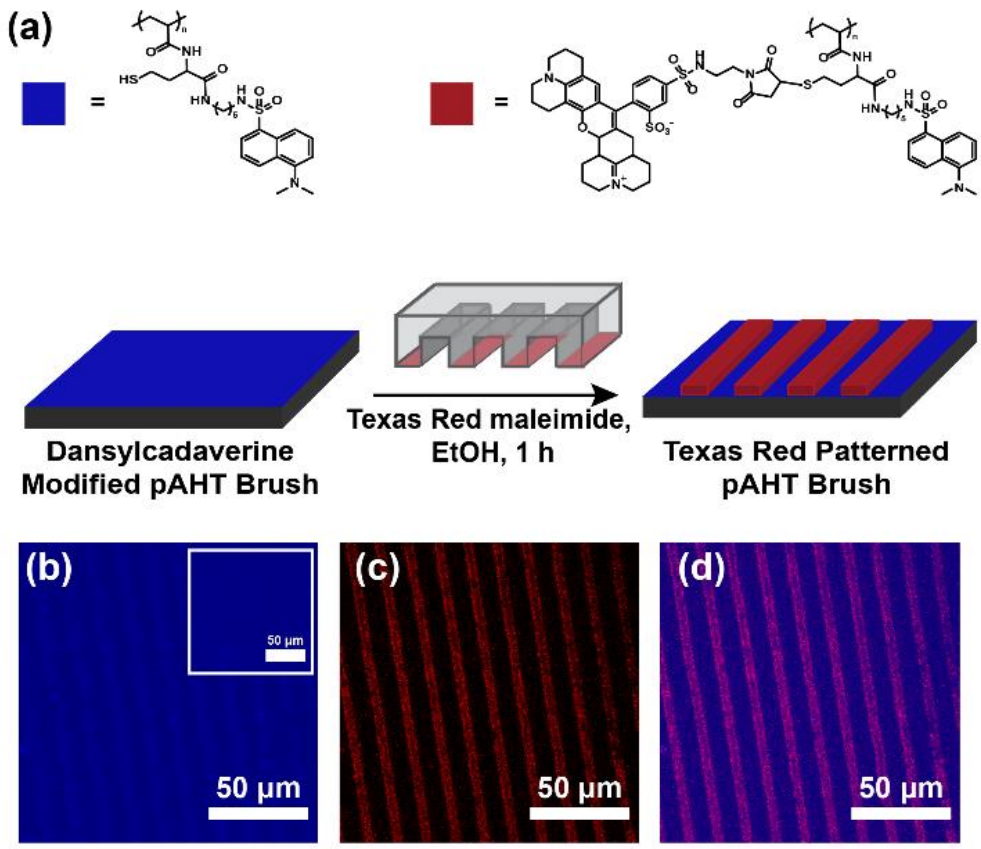

Figure 2.6 (a) Microcontact printing Texas Red C2 maleimide on the dansylcadaverine-modified pAHT brush. Fluorescent microscopy images of dansylcadaverine-modified pAHT brush and sequential patterning with Texas Red. Excitation of (b) dansylcadaverine at 405 nm (the inset image depicts a pAHT brush modified with dansylcadaverine without patterning of Texas Red) (c) Texas Red at 633 nm, and (d) both dyes.

2.4 Conclusions

In this work, we have demonstrated the synthesis and post-polymerization modification of poly(acrylamide-homocysteine thiolactone) (pAHT) brushes using sequential and one-pot amine-thiol-ene conjugation reactions. Amine-modified brushes generated reactive thiol precursors, which upon thiol-Michael addition provided multifunctional brush surfaces. Depth profile experiments conducted via XPS provided insight into the pAHT brush composition and PPM efficiency (e.g. sequential versus one-

pot reactions). In particular, the depth profiles showed a substantial difference between the F1s atomic composition of the sequential (~ 10 %) versus the one-pot (~ 30 %) modification. These results demonstrate the efficiency of the thiolactone one-pot double modification as a powerful PPM platform. Furthermore, we showed the thiol-containing pAHT brush surfaces readily serve as a modular PPM platform using reactive μCP to produce well-defined micropatterned surfaces. Future work will thoroughly explore the aminolysis and thiol-ene kinetics and other thiol-click chemistries (e.g. thiol-disulfide exchange). Ultimately, the pAHT brush platform offers an attractive approach for the design of complex brush architectures and offer an array of possibilities in polymer surface science applications.

2.5 Acknowledgments

This work was supported by the National Science Foundation (DMR-1056817). We thank Michael Blanton for help with confocal microscopy. CMR acknowledges support from the NSF Graduate Research Fellowship Program (DGE-1445151) and traineeship support from the NSF NRT program "Interface" (DGE-1449999) through the University of Southern Mississippi. XPS measurements were conducted at the Materials Science and Engineering Division, National Institute of Standards and Technology.

2.6 References

(1) Li, M.; Myers, E. B.; Tang, H. X.; Aldridge, S. J.; McCaig, H. C.; Whiting, J. J.; Simonson, R. J.; Lewis, N. S.; Roukes, M. L. Nanoelectromechanical Resonator Arrays for Ultrafast, Gas-Phase Chromatographic Chemical Analysis. *Nano Lett.* **2010**, *10* (10), 3899–3903. https://doi.org/10.1021/nl101586s.

(2) Kurosawa, S.; Aizawa, H.; Abidin, Z. Synthesis of Tethered-Polymer Brush by Atom Transfer Radical Polymerization from a Plasma-Polymerized-Film-Coated Quartz Crystal Microbalance and Its Application for Immunosensors. *Biosens. Bioelectron.* **2004**, *20*, 1165–1176. https://doi.org/10.1016/j.bios.2004.06.034.

(3) Morgese, G.; Gombert, Y.; Ramakrishna, S. N.; Benetti, E. M. Mixing Poly(Ethylene Glycol) and Poly(2-Alkyl-2-Oxazoline)s Enhances Hydration and Viscoelasticity of Polymer Brushes and Determines Their Nanotribological and Antifouling Properties. *ACS Appl. Mater. Interfaces* **2018**, *10* (48), 41839–41848. https://doi.org/10.1021/acsami.8b17193.

(4) Yan, S.; Shi, H.; Song, L.; Wang, X.; Liu, L.; Luan, S.; Yang, Y.; Yin, J. Nonleaching Bacteria-Responsive Antibacterial Surface Based on a Unique Hierarchical Architecture. *ACS Appl. Mater. Interfaces* **2016**, *8* (37), 24471–24481. https://doi.org/10.1021/acsami.6b08436.

(5) Yan, S.; Luan, S.; Shi, H.; Xu, X.; Zhang, J.; Yuan, S.; Yang, Y.; Yin, J. Hierarchical Polymer Brushes with Dominant Antibacterial Mechanisms Switching from Bactericidal to Bacteria Repellent. *Biomacromolecules* **2016**, *17* (5), 1696–1704. https://doi.org/10.1021/acs.biomac.6b00115.

(6) Takahashi, H.; Matsuzaka, N.; Nakayama, M.; Kikuchi, A.; Yamato, M.; Okano, T. Terminally Functionalized Thermoresponsive Polymer Brushes for Simultaneously Promoting Cell Adhesion and Cell Sheet Harvest. *Biomacromolecules* **2012**, *13* (1), 253–260. https://doi.org/10.1021/bm201545u.

(7) Abu-Lail, N. I.; Kaholek, M.; LaMattina, B.; Clark, R. L.; Zauscher, S. Micro-Cantilevers with End-Grafted Stimulus-Responsive Polymer Brushes for Actuation and Sensing. *Sensors Actuators, B Chem.* **2006**, *114* (1), 371–378. https://doi.org/10.1016/j.snb.2005.06.003.

(8) Zhou, F.; Biesheuvel, P. M.; Choi, E. Y.; Shu, W.; Poetes, R.; Steiner, U.; Huck, W. T. S. Polyelectrolyte Brush Amplified Electroactuation of Microcantilevers. *Nano Lett.* **2008**, *8* (2), 725–730. https://doi.org/10.1021/nl073157z.

(9) Santer, S.; Rühe, J. Motion of Nano-Objects on Polymer Brushes. *Polymer (Guildf).* **2004**, *45* (25), 8279–8297. https://doi.org/10.1016/j.polymer.2004.09.085.

(10) Galvin, C. J.; Genzer, J. Applications of Surface-Grafted Macromolecules Derived from Post-Polymerization Modification Reactions. *Prog. Polym. Sci.* **2012**, *37* (7), 871–906. https://doi.org/10.1016/j.progpolymsci.2011.12.001.

(11) Arnold, R. M.; Huddleston, N. E.; Locklin, J. Utilizing Click Chemistry to Design Functional Interfaces through Post-Polymerization Modification. *J. Mater. Chem.* **2012**, *22* (37), 19357–19365. https://doi.org/10.1039/c2jm31708g.

(12) Arnold, R. M.; Patton, D. L.; Popik, V. V.; Locklin, J. A Dynamic Duo: Pairing Click Chemistry and Postpolymerization Modification to Design Complex

Surfaces. *Acc. Chem. Res.* **2014**, *47* (10), 2999–3008. https://doi.org/10.1021/ar500191m.
(13) Wong, C.-H.; Zimmerman, S. C. Orthogonality in Organic, Polymer, and Supramolecular Chemistry: From Merrifield to Click Chemistry. *Chem. Commun.* **2013**, *49* (17), 1679-1695. https://doi.org/10.1039/c2cc37316e.
(14) Hudalla, G. A.; Murphy, W. L. Immobilization of Peptides with Distinct Biological Activities onto Stem Cell Culture Substrates Using Orthogonal Chemistries. *Langmuir* **2010**, *26* (9), 6449–6456. https://doi.org/10.1007/s10439-011-0452-9.Engineering.
(15) Zhang, S.; Vi, T.; Luo, K.; Koberstein, J. T. Kinetics of Polymer Interfacial Reactions: Polymer Brush Formation by Click Reactions of Alkyne End-Functional Polymers with Azide-Functional Substrates. *Macromolecules* **2016**, *49* (15), 5461–5474. https://doi.org/10.1021/acs.macromol.6b01220.
(16) Kolb, H. C.; Finn, M. G.; Sharpless, K. B. Click Chemistry: Diverse Chemical Function from a Few Good Reactions. *Angew. Chemie - Int. Ed.* **2001**, *40* (11), 2004–2021. https://doi.org/10.1002/1521-3773(20010601)40:11<2004::AID-ANIE2004>3.0.CO;2-5.
(17) Murata, H.; Prucker, O.; Rühe, J. Synthesis of Functionalized Polymer Monolayers from Active Ester Brushes. *Macromolecules* **2007**, *40* (15), 5497–5503. https://doi.org/10.1021/ma0624550.
(18) Brooks, K.; Yatvin, J.; McNitt, C. D.; Reese, R. A.; Jung, C.; Popik, V. V.; Locklin, J. Multifunctional Surface Manipulation Using Orthogonal Click Chemistry. *Langmuir* **2016**, *32* (26), 6600–6605. https://doi.org/10.1021/acs.langmuir.6b01591.
(19) Brooks, K.; Razavi, M. J.; Wang, X.; Locklin, J. Nanoscale Surface Creasing Induced by Post-Polymerization Modification. *ACS Nano* **2015**, *9* (11), 10961–10969. https://doi.org/10.1021/acsnano.5b04144.
(20) Buhl, M.; Tesch, M.; Lamping, S.; Moratz, J.; Studer, A.; Ravoo, B. J. Preparation of Functional Alternating Polymer Brushes and Their Orthogonal Surface Modification through Microcontact Printing. *Chem. Eur. J.* **2017**, *23* (25), 6042–6047. https://doi.org/10.1002/chem.201603565.
(21) Rahane, S. B.; Hensarling, R. M.; Sparks, B. J.; Stafford, C. M.; Patton, D. L. Synthesis of Multifunctional Polymer Brush Surfaces via Sequential and Orthogonal Thiol-Click Reactions. *J. Mater. Chem.* **2012**, *22* (3), 932–943. https://doi.org/10.1039/C1JM14762E.
(22) Hensarling, R. M.; Hoff, E. A.; Leblanc, A. P.; Guo, W.; Rahane, S. B.; Patton, D. L. Photocaged Pendent Thiol Polymer Brush Surfaces for Postpolymerization Modifications via Thiol-Click Chemistry. *J. Polym. Sci. Part A Polym. Chem.* **2013**, *51* (5), 1079–1090. https://doi.org/10.1002/pola.26468.
(23) Hensarling, R. M.; Doughty, V. A.; Chan, J. W.; Patton, D. L. "Clicking" Polymer Brushes with Thiol-Yne Chemistry: Indoors and Out. *J. Am. Chem. Soc.* **2009**, *131* (41), 14673–14675. https://doi.org/10.1021/ja9071157.
(24) Sparks, B. J.; Ray, J. G.; Savin, D. A.; Stafford, C. M.; Patton, D. L. Synthesis of Thiol-Clickable and Block Copolypeptide Brushes via Nickel-Mediated Surface Initiated Polymerization of α-Amino Acid N-Carboxyanhydrides (NCAs). *Chem.*

Commun. **2011**, *47* (22), 6245-6247. https://doi.org/10.1039/c1cc11534k.
(25) Espeel, P.; Goethals, F.; Du Prez, F. E. One-Pot Multistep Reactions Based on Thiolactones: Extending the Realm of Thiol-Ene Chemistry in Polymer Synthesis. *J. Am. Chem. Soc.* **2011**, *133* (6), 1678–1681. https://doi.org/10.1021/ja1098098.
(26) Espeel, P.; Du Prez, F. E. One-Pot Multi-Step Reactions Based on Thiolactone Chemistry: A Powerful Synthetic Tool in Polymer Science. *Eur. Polym. J.* **2015**, *62*, 247–272. https://doi.org/10.1016/j.eurpolymj.2014.07.008.
(27) Espeel, P.; Goethals, F.; Stamenović, M. M.; Petton, L.; Du Prez, F. E. Double Modular Modification of Thiolactone-Containing Polymers: Towards Polythiols and Derived Structures. *Polym. Chem.* **2012**, *3* (4), 1007-1015. https://doi.org/10.1039/c2py00565d.
(28) Espeel, P.; Goethals, F.; Driessen, F.; Nguyen, L.-T. T.; Du Prez, F. E. One-Pot, Additive-Free Preparation of Functionalized Polyurethanes via Amine–thiol–ene Conjugation. *Polym. Chem.* **2013**, *4* (8), 2449-2456. https://doi.org/10.1039/c3py00004d.
(29) Espeel, P.; Du Prez, F. E. One-Pot Double Modification of Polymers Based on Thiolactone Chemistry. *Adv. Polym. Sci.* **2015**, *269*, 105–132.
(30) Langlais, M.; Coutelier, O.; Destarac, M.; Imrcp, L.; Toulouse, U. De; Umr, C.; Sabatier, U. P.; Narbonne, D. Thiolactone-Functional Reversible Deactivation Radical Polymerization Agents for Advanced Macromolecular Engineering. *Macromolecules* **2018**, *51* (11), 4315–4324. https://doi.org/10.1021/acs.macromol.8b00770.
(31) Kubo, T.; Easterling, C. P.; Olson, R. A.; Sumerlin, B. S. Synthesis of Multifunctional Homopolymers *via* Sequential Post-Polymerization Reactions. *Polym. Chem.* **2018**, 13–15. https://doi.org/10.1039/C8PY01055B.
(32) Driessen, F.; Du Prez, F. E.; Espeel, P. Precision Multisegmented Macromolecular Lineups: A Display of Unique Control over Backbone Structure and Functionality. *ACS Macro Lett.* **2015**, *4* (6), 616–619. https://doi.org/10.1021/acsmacrolett.5b00231.
(33) Belbekhouche, S.; Reinicke, S.; Espeel, P.; Du Prez, F. E.; Eloy, P.; Dupont-Gillain, C.; Jonas, A. M.; Demoustier-Champagne, S.; Glinel, K. Polythiolactone-Based Redox-Responsive Layers for the Reversible Release of Functional Molecules. *ACS Appl. Mater. Interfaces* **2014**, *6* (24), 22457-22466. https://doi.org/10.1021/am506489j.
(34) Guo, W.; Hensarling, R. M.; LeBlanc, A. L.; Hoff, E. A.; Baranek, A. D.; Patton, D. L. Rapid Synthesis of Polymer Brush Surfaces via Microwave-Assisted Surface-Initiated Radical Polymerization. *Macromol. Rapid Commun.* **2012**, *33* (9), 863–868. https://doi.org/10.1002/marc.201100829.
(35) Patton, D. L.; Page, K. A.; Xu, C.; Genson, K. L.; Fasolka, M. J.; Beers, K. L. Measurement of Reactivity Ratios in Surface-Initiated Radical Copolymerization. *Macromolecules* **2007**, *40*, 6017–6020.
(36) Patton, D. L.; Page, K. A.; Hoff, E. A.; Fasolka, M. J.; Beers, K. L. A Robust and High-Throughput Measurement Platform for Monomer Reactivity Ratios from Surface-Initiated Polymerization. *Polym. Chem.* **2012**, *3* (5), 1174–1181. https://doi.org/10.1039/c2py20023f.

(37) Reinicke, S.; Espeel, P.; Stamenović, M. M.; Du Prez, F. E. One-Pot Double Modification of p(NIPAAm): A Tool for Designing Tailor-Made Multiresponsive Polymers. *ACS Macro Lett.* **2013**, *2* (6), 539–543. https://doi.org/10.1021/mz4002222.
(38) Montolio, S.; Zagorodko, O.; Porcar, R.; Isabel Burguete, M.; Luis, S. V.; Tenhu, H.; García-Verdugo, E. Poly(Acrylamide-Homocysteine Thiolactone) as a Synthetic Platform for the Preparation of Polymeric Ionic Liquids by Post Ring-Opening-Orthogonal Modifications. *Polym. Chem.* **2017**, *8* (33), 4789–4797. https://doi.org/10.1039/C7PY01067B.
(39) Socrates, G. *Infrared and Raman Characteristic Group Frequencies*, 3rd ed.; Wiley, 2001.
(40) Guo, W.; Xiong, L.; Reese, C. M.; Amato, D. V.; Thompson, B. J.; Logan, P. K.; Patton, D. L. Post-Polymerization Modification of Styrene-Maleic Anhydride Copolymer Brushes. *Polym. Chem.* **2017**, *8* (44), 6778–6785. https://doi.org/10.1039/c7py01659j.
(41) Schüwer, N.; Geue, T.; Hinestrosa, J. P.; Klok, H. A. Neutron Reflectivity Study on the Postpolymerization Modification of Poly(2-Hydroxyethyl Methacrylate) Brushes. *Macromolecules* **2011**, *44* (17), 6868–6874. https://doi.org/10.1021/ma201069d.
(42) Schuh, C.; Rühe, J. Penetration of Polymer Brushes by Chemical Nonidentical Free Polymers. *Macromolecules* **2011**, *44* (9), 3502–3510. https://doi.org/10.1021/ma102410z.
(43) Pamler, W.; Wildenauer, E.; Mitwalsky, A. Improved Depth Resolution in Auger Depth Profiles of TiN Thin Films by Optimized Sputtering Parameters. *Surf. Interface Anal.* **1990**, *15*, 621–626.
(44) Hofman, S. Sputter-Depth Profiling for Thin-Film Analysis. *Phil. Trans. R. Soc. Lond. A* **2004**, *362*, 55–75.
(45) Broderick, A. H.; Azarin, S. M.; Buck, M. E.; Palecek, S. P.; Lynn, D. M. Fabrication and Selective Functionalization of Amine-Reactive Polymer Multilayers on Topographically Patterned Microwell Cell Culture Arrays. *Biomacromolecules* **2011**, *12* (6), 1998–2007. https://doi.org/10.1021/bm200296a.
(46) Tang, Z.; Akiyama, Y.; Okano, T. Temperature-Responsive Polymer Modified Surface for Cell Sheet Engineering. *Polymers (Basel).* **2012**, *4* (3), 1478–1498. https://doi.org/10.3390/polym4031478.
(47) Tsougeni, K.; Petrou, P. S.; Papageorgiou, D. P.; Kakabakos, S. E.; Tserepi, A.; Gogolides, E. Controlled Protein Adsorption on Microfluidic Channels with Engineered Roughness and Wettability. *Sensors Actuators, B Chem.* **2012**, *161* (1), 216–222. https://doi.org/10.1016/j.snb.2011.10.022.
(48) Na, S. I.; Kim, S. S.; Jo, J.; Oh, S. H.; Kim, J.; Kim, D. Y. Efficient Polymer Solar Cells with Surface Relief Gratings Fabricated by Simple Soft Lithography. *Adv. Funct. Mater.* **2008**, *18* (24), 3956–3963. https://doi.org/10.1002/adfm.200800683.
(49) Gates, B. D.; Xu, Q.; Stewart, M.; Ryan, D.; Willson, C. G.; Whitesides, G. M. New Approaches to Nanofabrication: Molding, Printing, and Other Techniques. *Chem. Rev.* **2005**, *105* (4), 1171–1196. https://doi.org/10.1021/cr030076o.

CHAPTER III – BUCKLING INSTABILITIES IN POLYMER BRUSH SURFACES VIA POST-POLYMERIZATION MODIFICATION

3.1 Introduction

Buckling instabilities (wrinkles, creases, folds) are universal phenomena observed in natural and synthetic systems over a wide range of length scales. These instabilities can be tailored to define the shape, morphology, and function of complex systems - as exemplified by nature in the wrinkling of skin[1] or folding of brain tissue.[2] In polymeric films, stresses beyond a critical strain can trigger deformations in the film, results in interfacial delamination and fracture, which ultimately leads to undesirable applications.[3] However, more recently, strain-induced wrinkling of polymer thin films has emerged as a powerful approach to design surfaces with complex patterns at multiple length scales.[4] Recently, researchers have focused on exploiting this methodology to engineer surfaces for applications, including advanced adhesion,[5–8] tunable wettability,[9,10] antifouling,[11,12] flexible electronics,[14,15] microlens arrays,[16] diffraction gratings,[17,18] microcontact printing,[19] open-channel microfluidics,[21] anti-counterfeit technologies,[22] and various others.[23–25]

Buckling instabilities are manifested from an in-plane compression (i.e., mechanical, thermal, or osmotic) of a bilayer film composed of a thin, high-modulus film bonded to semi-infinite, low-modulus foundation. The wrinkle wavelength is dictated by the thickness of the top film and the film/substrate Young's modulus ratio, whereas the wrinkle amplitude is related to the thickness of the top film and the applied strain. Manipulating wrinkle wavelength and amplitude for specific applications requires careful selection of these parameters. Researchers have demonstrated various methods to tune the

modulus ratio of the stiff layer and underlying substrate, including metal deposition,[17,26] UV/ozone oxidation,[27] photoinduced cross-linking,[28,29] and surface-grafting techniques.[30] However, these methods have focused primarily on the fabrication of thin films with microscale morphologies on soft, deformable substrates (e.g., elastomers). Relatively few studies have focused on approaches to induce buckling instabilities in ultrathin (i.e., <100 nm) polymer films attached to rigid substrates.[31–33]

Post-polymerization modification (PPM) of polymer brushes is a powerful platform for tailoring the chemical and mechanical properties of surfaces.[34] The extended chain conformation of brushes has specific implications for the PPM process, where the high osmotic pressure and reduced chain conformational entropy disfavor the penetration of reactive modifiers into the brush.[35,36] Thus, the penetration depth and the through-thickness compositional homogeneity of the brush resulting from the PPM process are ultimately dependent on (i) the reaction conditions (solvent quality, reaction efficiency time), (ii) the tethered brush factors (grafting density and brush thickness), and (iii) the physical properties of the reactive molecule (molecular mass and steric bulk). Indeed, Klok et al. demonstrated via neutron reflectometry[36] and X-ray photoelectron spectroscopy[37] that increases in brush thickness, tethered brush grafting density, and molecular mass of the reactive post-modifier result in decreased depths of penetration and increased through-thickness brush heterogeneity. Intentional manipulation of PPM parameters provides an opportunity to design polymer brush structures with through thickness material properties profiles that fulfill the requirements for nanoscale buckling within ultrathin films on rigid substrates but has rarely been reported.

Recently, Brooks et al.[38] demonstrated a method to engineer nanoscale crease morphologies in ultrathin poly(pentafluorophenyl acrylate) (pPFPA) brushes using PPM via reactive microcontact printing with an amine-terminated polymer. Confinement of the pPFPA brush during the PPM process led to a substantial compressive stress, which was relieved to form the creased morphologies. This approach was expanded to fabricate creased morphologies using reactive diffusion of a viscous amine-terminated polymer solution to provide confinement.[39]

Herein, we report a simple PPM approach to engineer ultrathin poly(styrene-*alt*-maleic anhydride) (pSMA) brush surfaces with tunable wrinkled morphologies. We cross-link pSMA brushes under poor solvent conditions to limit the post-modification reaction to the near surface region of the brush, where reaction time dictates the ultimate thickness of the cross-linked surface region. Subsequent exposure of the selectively cross-linked brush surface to good solvent conditions generates an in-plane compressive stress arising from a mismatch between lateral and perpendicular swelling directions within the brush. The compressive stress causes an out-of-plane deformation of the untethered surface resulting in the observed wrinkled morphologies. Characterization of the PPM kinetics via ellipsometry and through thickness composition profile via time-of-flight secondary ion mass spectroscopy (ToF-SIMS) provided key insight into parameters influencing the buckling behavior.

3.2 Experimental Section

3.2.1 Materials

Maleic anhydride (MA), acetonitrile, cystamine dihydrochloride, triethylamine, tris(2-carboxylethyl) phosphine hydrochloride (TCEP), propylamine, hexylamine,

phosphate-buffered saline (PBS) solution were purchased from Sigma-Aldrich and were used as received. Styrene (Sty) was purchased from Sigma-Aldrich and was purified by passing through an alumina column to remove inhibitor before use. Silica wafers (orientation <100>, native oxide) were purchased from University Wafer. Plasma cleaning of silicon substrates was done on a plasma cleaner from Harrick Plasma.

3.2.2 Instrumentation and Characterization

To determine the swelling ratio of the cystamine-modified brush in acetonitrile, thickness measurements were conducted on a single angle (70°)/single wavelength (633 nm) ellipsometer (Gartner Scientific Corporation LSE) using a liquid cell with glass windows mounted at 70°. The thickness of swollen brush was calculated using a multilayer model consisting of Si, SiO_2, initiator, and a homogeneous swollen polymer brush. The refractive index (RI) of the swollen polymer layer was estimated using a linear effective medium approximation of the dry pSMA brush and solvent. Ellipsometry measurements were also conducted using a spectroscopic ellipsometer (JA Woollam M-2000U) coupled with a 5-mL horizontal liquid cell attachment with a 75° incidence angle. The experimental data was analyzed using JA Woolam CompleteEASE software. A three-layer model with a ambient liquid (nD = 1.344), a Cauchy layer for the polymer brush layer, a silicon oxide layer, and a bulk silicon layer was employed. The optical constants of the silicon crystal and the surface oxide were taken from literature, while the optical constants and thickness of the brush layer were allowed to vary in order to minimize the mean squared error. The optical constants for the polymer brush (Cauchy) layer were constrained in between the optical constants calculated for the dry brush layer measured from air and the optical constants for the pure solvent. The CompleEASE

software package includes an additional fit parameter to take into surface roughness that was used to improve the fit quality. Comparable swelling ratio data was obtained from both instruments. Grazing angle attenuated total reflection FTIR (gATR-FTIR) analysis was carried out using a Thermo Scientific FTIR (Nicolet 8700) equipped with a VariGATR accessory (grazing angle 65°, germanium crystal; MCT detector, Harrick Scientific). Spectra were collected with a resolution of 4 cm^{-1} and 128 scans per sample. All spectra were collected while purging the VariGATR attachment and FTIR instrument with nitrogen along the infrared beam path to minimize the peaks corresponding to atmospheric moisture and CO_2. Spectra were analyzed and processed using Omnic software and OriginPro. Atomic force microscopy (AFM) was performed using a Bruker Dimension Icon instrument. AFM height images were collected in tapping mode (in air) to obtain thin film morphology. The polymer brush samples were scanned using RTESPA-300 probes (from Bruker) with a nominal spring constant of 40 N/m. The AFM height images were analyzed using the SPIP software. The wrinkle wavelengths were obtained from the radial averaged cross-section of fast Fourier transform (FFT) of the height image. Static water contact angles of polymer brush surfaces were measured using 6 μL water droplets on a Rame-hart goniometer. Time-of-Flight Secondary Ion Mass Spectrometry (ToF-SIMS) measurements were performed at the Oak Ridge National Lab (ORNL) to characterize the through-thickness distribution of cystamine within the polymer brush. The experiments were conducted using ION.TOF5 mass spectrometer with Bi-ion primary gun (30 keV, 30 nA, 200 μm × 200 μm scanning region, 5 μm spot size) as the ionization source and a sputtering Ar ion-cluster gun (cluster size ~2000 ions, 5 keV, 4 nA, sputtering region 400 μm × 400 μm, spot size ~20 μm). The secondary ions

were collected by a ToF detector in both positive detection modes with resolution m/Δm~2000-4000. Si^+, $C_3H_3^+$, H_3S^+ ions were used to identify carbon, sulfur and silicon component within the samples.

3.2.3 Surface-initiated polymerization of pSMA brush

Functionalization of silicon surfaces with an azo-based trichlorosilane initiator was utilized and it was synthesized following literature procedures.[40,41] Silicon substrates were cleaned and functionalized with the azo-based initiator following the procedures in the previous chapter. A substrate with the azo-based initiator was placed in a sealed test tube and purged with nitrogen. In another test tube, styrene (0.40 mL, 0.36 g) and maleic anhydride (0.40 g) were dissolved in anhydrous acetonitrile (4 mL) and the solution was freeze-pump-thawed to remove oxygen. The degassed solution was then transferred via cannula into the test tube that contained the initiator-immobilized substrate. The test tube was heated at 95 °C for various times to obtain polymer brushes of different thickness (i.e. 40 nm, 80 nm, 120 nm). After polymerization, pSMA brush-modified substrates were removed from the solution, cleaned by rinsing and sonicating in the acetonitrile solution to get rid of any physisorbed polymer and dried with nitrogen.

3.2.4 PPM of pSMA substrates using cystamine under poor solvent conditions

Cystamine dihydrochloride (40 mg, 0.18 mmol) and TEA (40 μL, 29 mg, 0.29 mmol) were dissolved in 4 mL of deionized water. A pSMA brush surface was placed in the cystamine solution at discrete reaction times (from 30 s to 3 h). After PPM, the post-modified pSMA substrate was thoroughly rinsed with DI water and dried with a flow of nitrogen.

3.2.5 PPM of pSMA brush with cystamine dihydrochloride under good solvent conditions

Cystamine dihydrochloride (0.40 mg, 1.8 μmol) and TEA (0.40 μL, 0.29 mg, 2.9 μmol) were dissolved in 4 mL of solvent mixture that contains 50% of DI water and 50% of acetonitrile. A substrate with pSMA brush on the surface was placed in the cystamine solution for 30 s. After PPM, the post-modified pSMA substrate was thoroughly rinsed with DI water and dried with a flow of nitrogen.

3.2.6 PPM of pSMA substrates using mono-amines under aqueous conditions

Hexylamine (0.40 μL, 0.31 mg, 3.1μmol) was added to 4 mL of DI water. A pSMA brush-modified substrate was placed in the hexylamine solution at 30 s and 150 s. The post-modified pSMA substrates were thoroughly rinsed with DI water and dried with a stream of nitrogen. The post-modification of pSMA brush using propylamine (0.24 μL, 0.17 mg, 2.9 μmol) was carried out in 4 mL of DI water.

3.2.7 Reduction of cystamine modified pSMA brush

A cystamine-modified pSMA brush substrate was placed in a solution of TCEP (60 mg, 0.21 mmol) in 6 mL of acetonitrile: PBS solvent mixture (50:50 by volume) in a sealed test tube. The TCEP solution was under constant nitrogen purging for 16 h. The substrate was then taken out of the solution, rinsed with DI water and dried with a flow of nitrogen.

3.2.8 Oxidation of thiols to disulfide

Iodine (32 mg) was dissolved in H_2O_2 (3 mL) and MeCN (3mL). The reduced cystamine-modified pSMA brush was placed in the solution in a sealed test tube for 16 h.

The substrate was then taken out of the solution, sonicated in DI water, and swelled in MeCN for 1 h to reform the wrinkled morphologies.

3.2.9 Grafting density of pSMA

The grating density of pSMA on silica substrates was calculated using equation 1. In which Γ is the grafting density, L is the polymer brush thickness, ρ is bulk density, N_A is the Avogadro number and M_n is the number relative molecular mass of the free polymer of SMA determined by GPC. We make the assumption that the molecular mass of the polymer brush and free polymer are the same. For a given sample with a thickness of 83 nm, number-average molecular mass (M_n) was 31167 g/mol and PDI 2.4. Grafting density Γ was calculated to be 1.7 chains/nm^2.

$$\Gamma = \frac{L\rho N_A}{M_n} \qquad \text{Equation 1}$$

3.2.10 Calculation of anhydride conversion based on thickness measurements

The thickness values of pSMA brush samples before and after cystamine modification were measured using ellipsometry. The modification of the pSMA brush with cystamine increases the molar mass of the repeat units and results in an increase in brush thickness. Equation 2 describes the relationship between polymer brush thickness, *H*, molecular weight of polymer repeat unit, *M*, and the mass density, ρ, of polymer brush before and after modification, [49]

$$\frac{H_f}{H_o} = \frac{M_f \rho_o}{M_o \rho_f} \qquad \text{Equation 2}$$

where the subscripts o and f denote the unmodified and cystamine-modified polymer brush, respectively. Assuming equivalent mass density of the polymer brush before and after post-modification, Equation 2 becomes Equation 3, where *k* represents conversion

and M_{PPM} denotes the molecular weight of the modifier that reacts onto the polymer chain, respectively.

$$\frac{H_f}{H_o} = \frac{M_f}{M_o} = \frac{M_o + kM_{PPM}}{M_o} \qquad \text{Equation 3}$$

At full conversion, (k =100%), the molecular mass of modifier, M_{PPM}, was calculated to be 135.06 g/mol, based on Equation 3. The calculated M_{PPM} is less than the molecular weight of cystamine (152.28 g/mol) which can be attributed to the cystamine molecules that react with polymer brush by two amines. The percentage of cystamine as cross-linker, x, was calculated to be 12.7%, following Equation 4,

$$x = \frac{M_{cystamine} - M_{PPM}}{M_{PPM}} \qquad \text{Equation 4}$$

in which $M_{cystamine}$ is the MW of cystamine (152.28 g/mol). The amount of cystamine serving as cross-linkers can only be estimated at full anhydride conversion. Further, it is not possible to distinguish between inter- and intramolecular reactions. The anhydride conversion k can be calculated according to Equation 5

$$k = \frac{M_o}{M_{PPM}}\left(\frac{H_f}{H_o} - 1\right) \qquad \text{Equation 5}$$

3.3 Results and Discussion

3.3.1 Synthesis of pSMA Polymer Brush

For this work, we employed poly(styrene-*alt*-maleic anhydride) (pSMA) as a reactive polymer brush scaffold. pSMA is easily obtained from commodity monomers and is highly reactive towards primary amines for facile post-polymerization modification reactions. Alternating pSMA brushes were synthesized via surface-initiated polymerization of a 54:46 styrene:maleic anhydride monomer feed from an azo-initiator modified silicon substrates. It is well-known that styrene and maleic anhydride monomers

form nearly perfect alternating copolymers under most free-radical polymerization conditions. Polymerizations occurred at 95 °C to produce pSMA brushes with an average thickness of approximately 80 nm. Following extraction, the surfaces showed a typical featureless brush morphology with 6.6 nm root-mean-squared (RMS) roughness, as determined via atomic force microscopy (AFM) (See Appendix B for Figure B.1). The pSMA brush chemical composition and hydrolytic stability were measured by grazing-angle attenuated total reflection Fourier transform infrared spectroscopy (gATR-FTIR). Peaks at 1454 cm^{-1} and 1494 cm^{-1} are attributed to the aromatic styrene moiety, whereas peaks at 1781 cm^{-1} and 1857 cm^{-1} are indicative of the five-membered anhydride ring (Figure B.3a).[39-40] As shown in Figure B.2, the anhydride exhibited minimal hydrolysis in air at room temperature and when immersed in deionized water at 60 °C for 60 min. The hydrophobicity of the pSMA brush surfaces (92° water contact angle, Figure B.1) likely contributes to the observed stability by limiting diffusion of water into the brush – an important point that we exploited for controlled PPM of the brush.

3.3.2 Post-polymerization Modification (PPM) of pSMA with Cystamine Dihydrochloride

Poly(styrene-*alt*-maleic anhydride) brushes were post-modified with cystamine dihydrochloride in the presence of triethylamine under aqueous conditions. Alswieleh and co-workers recently demonstrated the use of solvent quality to spatially control cross-linking within a brush surface; cross-linking in good solvent provided homogeneous cross-linking throughout the brush, whereas poor solvents resulted in cross-linking primarily at the polymer/air interface.[42] Similarly, in our system, poor solvent conditions for the post-modification are postulated to collapse the brush structure and initially limit

the cystamine cross-linking reaction to the exposed brush interface. If the amine−anhydride reaction is fast relative to diffusion of the cystamine into the brush (a good assumption under poor solvent conditions), then the post-modification may be expected to proceed in a front-like process as depicted in Scheme 3.1. Under such conditions, reaction time would serve as a facile parameter to control the penetration depth of the cystamine and, consequently, the depth of the cross-linked surface region within the brush. This hypothesis can be easily investigated by monitoring the PPM reaction kinetics and the resulting through thickness compositional brush profiles, as discussed in the following section.

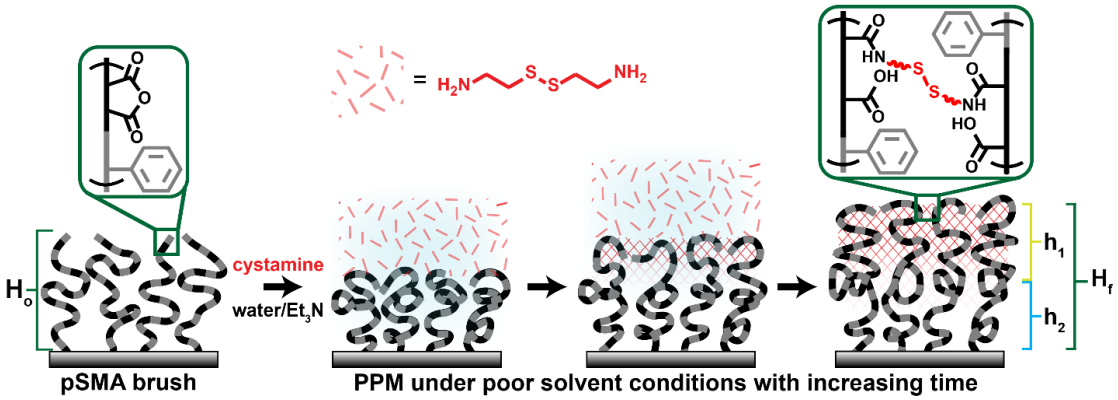

Scheme 3.1 Synthetic route to post-polymerization modification of pSMA brushes with cystamine under poor solvent (aqueous) conditions. Cystamine partially cross-links the brush in a front-like process, forming a cystamine-modified "skin" thickness (h_1) and an unmodified "substrate thickness" (h_f). Final brush thickness after PPM and drying is denoted as H_f.

pSMA brushes with an initial dry thickness (H_o = 80 nm) were post-modified with cystamine dihydrochloride in the presence of triethylamine under aqueous conditions at discrete reaction times per Scheme 3.1. The diamine−anhydride reaction serves to partially cross-link the brush and results in the formation of amide−acid moieties along the backbone (see FTIR, Figure B.3b). An increase in molecular mass of

repeat units modified with cystamine results in an increase in the overall brush thickness.[43] The difference in brush thickness before and after PPM was used to calculate the anhydride conversion according to the equation:

$$\frac{H_f}{H_0} = \frac{M_f \rho_0}{M_0 \rho_f}$$

where H represents dry brush thickness, ρ is bulk density, and M is the molecular mass of the repeat unit. The subscripts denote the unmodified (0) and cystamine-modified (f) states of the pSMA brush. Here, we assume that the grafting density of chains before and after modification remains constant and the change in bulk density is negligible.[43] Anhydride conversion was also determined using FTIR based on the change in area of the anhydride peak absorption (Figure B.4). Figure 3.1 shows the anhydride conversion versus time for the cystamine post-modification obtained by ellipsometry and FTIR under aqueous conditions. As shown, both methods are in good agreement. Under aqueous conditions, the amine−anhydride modification was relatively slow with conversion plateauing at approximately 90% at 3600 s. Under poor solvent conditions, one can assume that the pSMA brush exists in a collapsed state posing a barrier to the diffusion of cystamine into the brush. Consequently, the number of accessible anhydrides to cystamine is limited by the rate of cystamine diffusion into the polymer brush. Under these conditions, the PPM reaction rate is independent of the total number of unreacted anhydride groups within the polymer brush; thus, the PPM process would be expected to follow pseudo-zero-order kinetics. The linear region (0−1200 s, Figure 3.1) in the conversion versus time plot suggests that the PPM reaction indeed proceeds with pseudo-zero-order kinetics under poor solvent conditions. In contrast, >96% anhydride

conversion was achieved within 60 s with PPM under good solvent conditions (e.g. 50:50 v/v% acetonitrile:water) as shown in Figure B.5. With the pSMA brush well-solvated in acetonitrile, the PPM reaction follows pseudo-first-order kinetics. Similar kinetic trends have been well described by others for PPM of polymer brushes under good solvent conditions.[44,45]

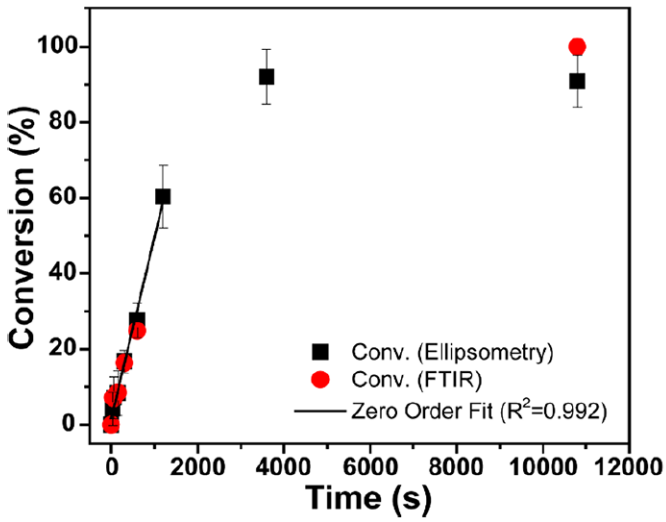

Figure 3.1 Anhydride conversion versus cystamine reaction time for pSMA brush (H_o = 80 nm) under poor solvent conditions.

ToF-SIMS analysis with argon ion cluster sputtering was utilized to depth-profile the through-thickness composition of the pSMA brush as a function of cystamine post-modification time. The intensities of the $C_3H_3^+$ (m/z = 39), H_3S^+ (m/z = 35), and Si^+ (m/z = 28) secondary ions - characteristic of the pSMA brush backbone, cystamine modifier, and silicon substrate, respectively - were recorded as a function of sputtering time.[46] Sputter time was converted to depth (nm) using knowledge of the overall brush thickness and sputter rate for each sample. The polymer brush/silicon substrate interface was determined using the intersection of the $C_3H_3^+$ and Si^+ profiles.[47] Total brush thickness values determined from the $C_3H_3^+$ and Si^+ intersection are in good agreement with total

brush thickness values obtained from ellipsometry (Table B.1). The thickness of the cystamine-modified brush region (h_1) was approximated from the depth at which the H_3S^+ ion intensity reached 50% of its maximum value. Figure 3.2a shows the secondary ion profiles of an unmodified pSMA brush. A constant $C_3H_3^+$ intensity was observed for the full thickness of the pSMA brush. The absence of cystamine within the unmodified brush is indicated by the noise level H_3S^+ intensities observed throughout the brush thickness. The secondary ion profiles for cystamine-modified pSMA brushes post-modified under aqueous conditions with reaction times at 60 s (2.4% conversion), 300 s (15.6% conversion), and 600 s (30.1% conversion) are shown in Figure 3.2b-e, respectively. At short PPM times, H_3S^+ ions were primarily observed near the polymer/air interface with intensities that quickly decay to noise levels with increasing depth. The H_3S^+ profiles show a progressively deeper penetration of cystamine into the pSMA brush with increasing PPM time. At extended cystamine modification times or high anhydride conversion (3600 s, 88% conversion), a relatively constant H_3S^+ ion intensity was observed throughout the brush thickness, indicating the modification reaction eventually penetrates the full thickness of the brush. In contrast, Figure 3.2f shows the ToF-SIMS profile for a pSMA brush modified with a low concentration cystamine solution (0.45 mmol/L) for 30 s under good solvent conditions. The anhydride conversion for this sample was ~26%. The H_3S^+ profile shows that cystamine is distributed throughout the full brush thickness despite having a much shorter cystamine modification time than any of the samples modified under poor solvent conditions. PPM under good solvent conditions swells the brush, enabling rapid diffusion of the modifier

into the brush and broader access to anhydride groups throughout the brush. These conditions result in a more homogeneous modified brush composition profile.

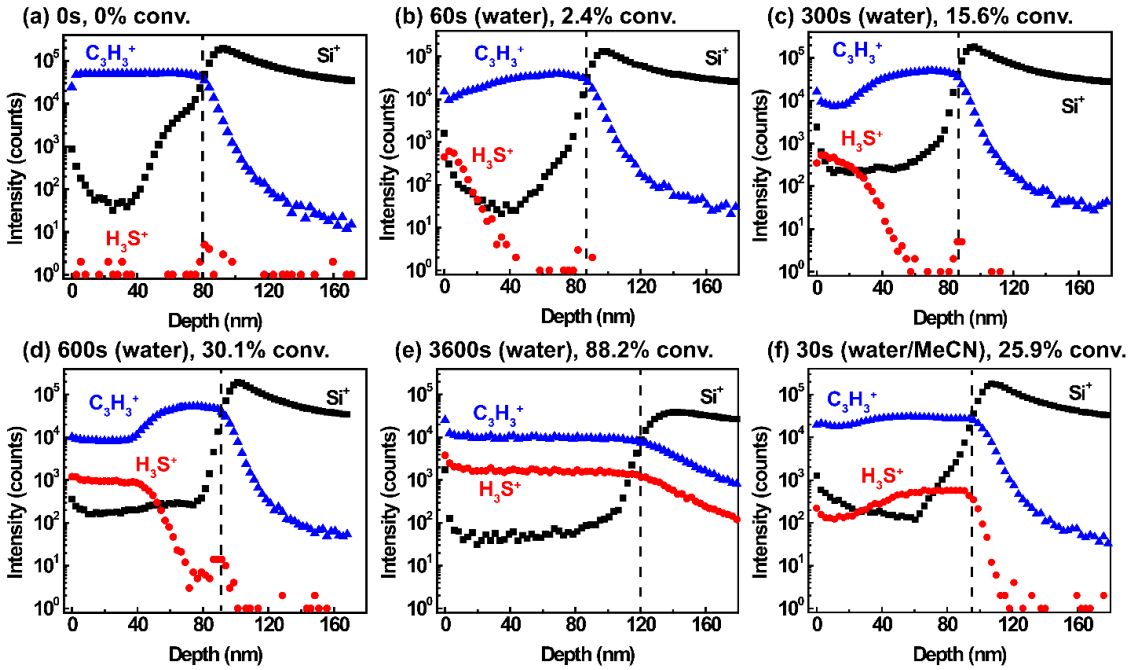

Figure 3.2 Secondary ion intensity−sputtering time profiles of unmodified and cystamine-modified pSMA brush samples. (a) 80 nm unmodified pSMA brush, cystamine-modified pSMA under aqueous conditions for (b) 60, (c) 300, (d) 600, and (e) 3600 s. (f) Cystamine-modified pSMA brush under good solvent conditions. Anhydride conversion values are shown for each PPM time point. The vertical dashed line indicates the silicon/brush interface.

To further illustrate the trends for PPM of pSMA brushes with cystamine under poor solvent conditions, we generated kinetic plots using the fractional thickness of the pSMA brush penetrated by cystamine (h_1/H_f) obtained from ToF-SIMS. Figure 3.3a shows h_1/H_f versus PPM time. The h_1/H_f ratio scales linearly with PPM time up to 1200 s and then deviates from linearity at longer reaction times - a trend that is in qualitative agreement with PPM kinetics obtained by ellipsometry and FTIR, as previously described (Figure 3.1). The fractional thickness modified by cystamine shows a similar dependence on anhydride conversion (Figure 3.3b).

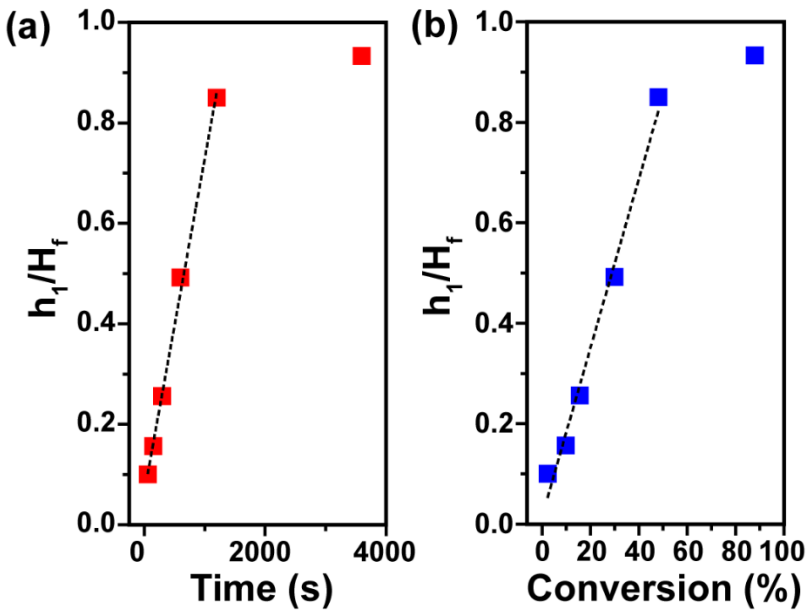

Figure 3.3 Ratio of cystamine-modified thickness (h_1) to total brush thickness (H_f) versus (a) cystamine modification time and (b) anhydride conversion. (H_o = 80 nm).

With insight from kinetics and depth profiling, we return to the postulation of a front-like post-modification process under poor solvent conditions to describe an empirical relationship between anhydride conversion and brush thickness parameters (e.g., h_1, h_2, and H_f). For example, post-modification of a pSMA brush to near-quantitative conversion results, on average, in a 66% increase in thickness (H_o = 77.9 nm, H_f = 129.8 nm, or 1.66H_o) after modification. Assuming a frontal modification reaction, we can now divide the brush into two distinct regions: a cystamine-modified "skin" layer of thickness $h_1$and the remaining unmodified brush layer of thickness h_2 (Scheme 3.1). Using this model, we can then define h_1 as (1.66H_o)k, h_2 as $H_o(1-k)$, and H_f as h_1 + h_2 where k is conversion. Employing these relationships, a pSMA brush with H_o = 84.5 nm and k = 9.9% results in predicted values for h_1 = 13.8 nm, h_2 = 76.1 nm, and H_f = 89.9 nm. The predicted values are in good agreement with the actual measured values of

h_1 = 13.5 nm, h_2= 76.5 nm, and H_f= 90.0 nm obtained from ToF-SIMS. These data along with additional examples are summarized in Table B.2. The empirical equations proposed and the ToF-SIMS depth profile data collectively support our postulation that the cystamine modification reaction under poor solvent conditions occurs as a frontal process. Additionally, these observations provide further evidence that reaction time and anhydride conversion serve as handles to control the penetration depth of cystamine and, consequently, the depth of the cross-linked surface region within the brush.

3.3.3 Buckling Instability in Cystamine-Modified pSMA Brush Surfaces

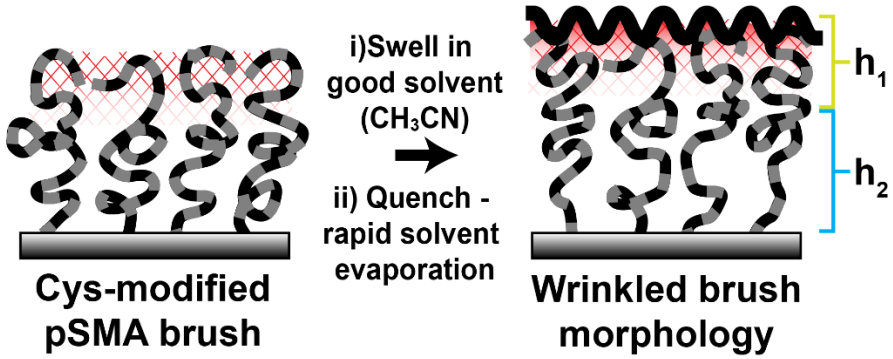

Scheme 3.2 Synthetic route to wrinkled polymer brush surfaces. Cystamine-modified pSMA brush surfaces were exposed to good solvent conditions (acetonitrile) to induce a wrinkled brush morphology. The length scale of wrinkle wavelength and brush thickness are not drawn to scale.

Figure 3.4a shows the tapping-mode AFM height images for pSMA brushes following PPM with cystamine dihydrochloride/TEA in water at various anhydride conversions. At each conversion point, a typical featureless brush morphology (RMS roughness: 6.6 nm) was observed that was unchanged in comparison to the unmodified pSMA brush morphology. Next, we exposed the series of cystamine-modified pSMA brushes to good solvent conditions (acetonitrile) to induce swelling as illustrated in Scheme 3.2. Figure 3.4b shows the brush morphologies after swelling in acetonitrile for

60 min. The brush wrinkling patterns that developed upon swelling show a clear dependence on the anhydride conversion, transitioning from small scale random labyrinths at low conversions (7.1%) to larger scale labyrinths at higher conversions (31.2%). In general, wrinkles were not observed in cystamine-modified brush samples with anhydride conversions >40% (Figure B.6). It is important to note that AFM imaging was conducted in the dry state after rapid evaporation of acetonitrile under a stream of nitrogen. It is expected that the pSMA polymer brush rapidly traverses the glass transition temperature (typical pSMA T_g > 120 °C) upon solvent evaporation, trapping the observed wrinkle morphologies in the dry state. Similar arguments have supported the observation of trapped buckled morphologies in surface-confined poly(*N*-isopropylacrylamide) gels.[33,48] The swelling response of polymer brushes relies on several interdependent parameters including grafting density, molecular mass, chemical nature of the polymer chains, and solvent quality.[49] In the present system, the brush swelling response is also influenced by the extent of cross-linking. Since the pSMA brushes were cross-linked under poor solvent conditions, subsequent exposure to a good solvent likely generates a swelling mismatch between the lateral and perpendicular directions, where the in-plane swelling constraint may be attributed to both attachment of chains to the substrate and to extent of cross-linking. As the brush expands more in the direction normal to the substrate relative to the constrained lateral direction, an in-plane compressive stress is generated. At a critical degree of swelling, the imposed compressive stress causes an out of plane deformation of the untethered surface, resulting in the observed wrinkled morphologies. To define the critical degree of swelling that results in surface wrinkling, we determined the swelling ratio (α) of the cystamine-modified pSMA brushes as a

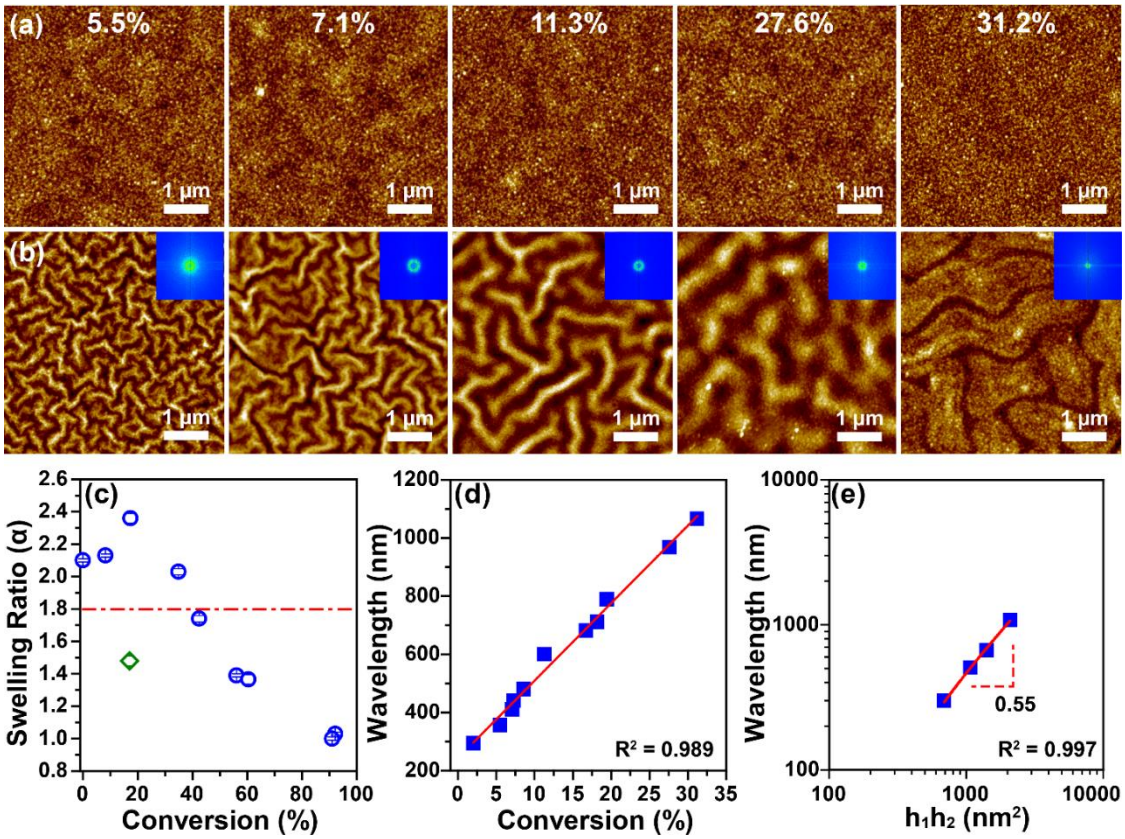

Figure 3.4 AFM height images of pSMA brushes (H_o= 80 nm) following (a) reaction with cystamine and (b) subsequent exposure to good solvent (acetonitrile) conditions. (c) Swelling ratio versus anhydride conversion for cystamine-modified pSMA brushes. The horizontal line represents the critical swelling ratio. (d) Wavelength versus anhydride conversion. (e) Fit of the wrinkling wavelength as a function of $h_1 h_2$ demonstrating that the scaling relationship $\lambda \sim (h_1 h_2)^{1/2}$ adequately describes the brush system.

function of anhydride conversion using *in situ* ellipsometry. The swelling ratio is defined as the thickness of cross-linked brush (swollen thickness in acetonitrile) to that of the dry cross-linked brush (prior to swelling). Figure 3.4c shows the relationship between swelling ratio and conversion for the pSMA brushes modified with cystamine under poor solvent conditions. The swelling ratio of an unmodified pSMA brush was ~2.1. At anhydride conversions <20%, an increase in the swelling ratio was observed that may be attributed to an increase in brush/solvent compatibility due to the contribution of carboxylic acid functional groups formed upon reaction of the maleic anhydride with

cystamine. At anhydride conversions >30%, a gradual decrease in swelling ratio was observed as the extent of cross-linking begins to dominate the swelling behavior. The critical swelling ratio, below which the compressive stress is insufficient to induce surface buckling, was found to be ~1.8 (~40% anhydride conversion) - a critical value that is consistent with other reports from the literature.[50] Referring back to the ToF-SIMS depth profiles, the critical swelling ratio can be correlated to a h_1/H_f ratio of approximately 0.6. Additionally, we considered if the distribution or depth profile of cross-links within the pSMA brush influenced the swelling behavior and, consequently, the propensity to undergo surface buckling. As illustrated in Figure 3.2f, pSMA brushes post-modified with cystamine under good solvent conditions at short reaction times resulted in the distribution of cystamine throughout the full brush thickness. At comparable anhydride conversions, pSMA brushes modified under good solvent conditions exhibited lower swelling ratios (e.g., $\alpha = 1.48$ at 17% conversion, Figure 3.4c) than brushes modified under poor solvent conditions (e.g., $\alpha = 2.4$ at 17% conversion). When cross-linked under good solvent conditions, the swelling ratio was consistently below the critical α of 1.8; thus, buckling was not observed in these samples (Figure B.7). These results suggest that the cross-link profile influences the swelling ratio and the ability of the brushes to undergo buckling; however, an alternative explanation should also be considered to explain the absence of wrinkles when cross-linked under good solvent conditions. Namely, following the Flory−Rehner formalism, reswelling the cross-linked brush in the same solvent employed for cross-linking would return a zero-osmotic stress state - conditions that would not induce surface instabilities.[51]

The wavelengths of the wrinkled morphologies were measured by taking the radial average of the AFM 2D FFT power spectra. The 2D power spectrum represents the power distribution of the wrinkled morphology based on the relationship between the frequency and space domain.[52] The smaller circular distribution is correlated to a larger wrinkle wavelength. As shown in Figure 3.4d, the observed wrinkle wavelength (λ) scales linearly with anhydride conversion. Linear scaling relationships between wrinkle wavelength and film thickness are well-established and have been described for multiple film constructs. Here, we consider a rigid-on-soft multilayer construct consisting of a cystamine-modified "skin" layer (h_1) and an unmodified brush "substrate" layer (h_2) that is in turn covalently grafted to a rigid silicon support (h_{Si}), where $h_{Si} \gg h_2 > h_1$. For such constructs, scaling can be described as $\lambda \sim (h_1 h_2)^{1/2}(E_{h_1} E_{h_2})^{1/6}$, where E_{h_1} and E_{h_2} are the Young's moduli of the cystamine-modified "skin" layer and the unmodified "substrate" layer, respectively.1,[53–55]As shown in Figure 3.4e, the observed dependence of the wrinkle wavelength on the $h_1$and h_2 thicknesses is adequately described by the scaling relation $\lambda \sim (h_1 h_2)^{1/2}$. Although we lack the ability to determine the modulus of the individual "skin" and "substrate" regions within the brush - values that would enable further quantitative validation to the model - our current observations are in qualitative agreement with the scaling relationship predicted by the general bilayer film model. More importantly, these observations demonstrate that wrinkle wavelength and morphology can be judiciously tuned by controlling the brush profile via post-polymerization modification under poor solvent conditions.

3.3.4 Monofunctional Amine Modified pSMA Brush Surface

The importance of employing a cross-linker such as cystamine to facilitate the formation and stabilization of the wrinkled brush surfaces was illustrated through several control experiments. First, pSMA brushes were modified with two different monofunctional amines (e.g., propylamine and hexylamine) under identical aqueous conditions as used for cystamine. Despite the similar chain length of cystamine and hexylamine, using monofunctional amines as post-modifiers did not lead to the formation of wrinkles regardless of PPM reaction time or conversion (Figure 3.5). Brushes modified with primary amines undergo swelling but lack the cross-links necessary to generate the mismatch in lateral and perpendicular swelling. Thus, the compressive stress required for buckling is absent.

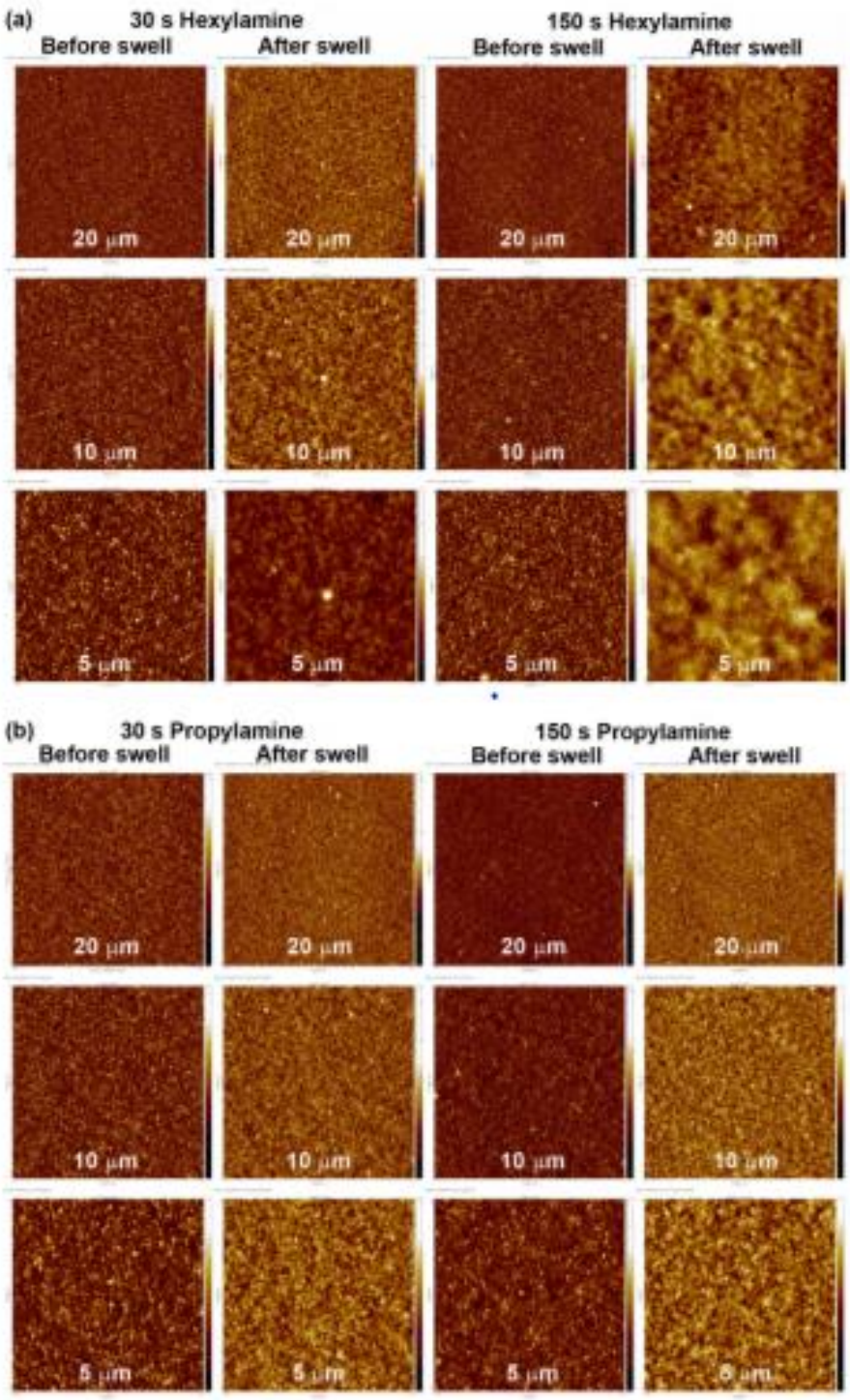

Figure 3.5 AFM images of pSMA brushes post-modified with monofunctional amines using identical reaction conditions as used for cystamine: (a) hexylamine and (b) propylamine. As shown, wrinkles were not observed after swelling in acetonitrile.

3.3.5 Effect of Polymer Brush Thickness

After investigating the parameters that govern buckling instabilities in pSMA brush surfaces, we further studied the influence of initial pSMA brush thickness on the observed wrinkled morphologies. The initial experiments previously described were performed with an initial brush thickness, H_o = 80 nm. To elucidate the influence of brush thickness on wrinkled morphologies, a library of pSMA brushes with increasing brush thickness was synthesized by changing polymerization time at a constant monomer concentration and temperature (95 °C).[35,56] Hereafter, pSMA brushes with an average target thickness of 40 nm and 120 nm were prepared and employed for the following experiments.

3.3.6 Buckling Instabilities in 40 nm pSMA Brush Surfaces

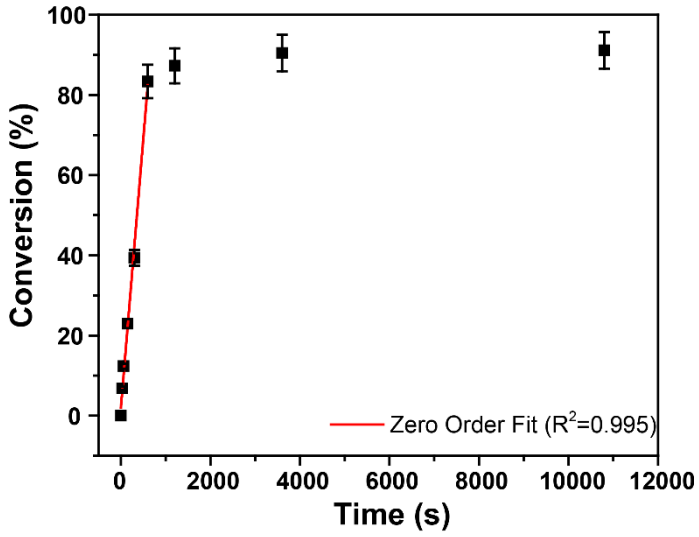

Figure 3.6 Anhydride conversion versus cystamine reaction time for pSMA brush (H_o = 40 nm) under poor solvent conditions.

pSMA brushes (H_o = 40 nm) were synthesized as previously described (e.g. 54:46 styrene:maleic anhydride at 95 °C). After polymerization, pSMA surfaces were post-modified with cystamine dihydrochloride under aqueous conditions at discrete reaction

times. The conversion versus reaction time plot for the cystamine modification of the pSMA brush is shown in Figure 3.6. The change in brush thickness was measured by ellipsometry and used to calculate anhydride conversion as a function of reaction time. Anhydride conversion greater than 80% was achievable within 1000 s with conversion plateauing at approximately 90% around 1200s. The linear region (0-1000 s, Figure 3.6) in the conversion versus time displays pseudo-zero-order kinetics. The lower pSMA brush thickness led to a faster anhydride conversion compared to the 80 nm pSMA brush scaffold (Figure 3.1). A lower pSMA brush thickness and grafting density allow an increase in the accessibility of the maleic anhydride moieties of the polymer backbone, resulting in faster PPM kinetics. Similar results have been observed by Schüwer et al.[36]

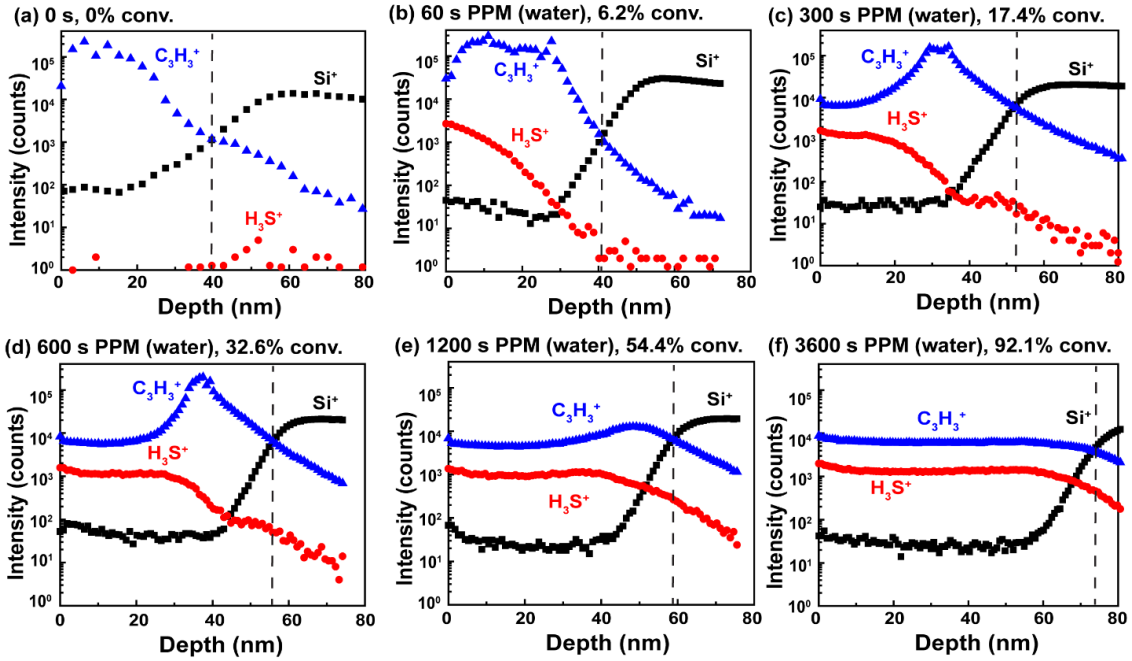

Figure 3.7 Secondary ion intensity−sputtering time profiles of unmodified and cystamine-modified pSMA brush samples. (a) 40 nm unmodified pSMA brush, cystamine-modified pSMA under aqueous conditions for (b) 60, (c) 300, (d) 600, (e) 1200 s, and (f) 3600 s. Anhydride conversion values are shown for each PPM time point. The vertical dashed line indicates the silicon/brush interface.

ToF-SIMS analysis was employed to obtain depth-profiles of the 40 nm pSMA brushes as a function of cystamine modification time. Figure 3.7a shows the secondary ion profiles of an unmodified pSMA brush. The depth profiles for the cystamine-modified pSMA brushes post-modified under aqueous conditions with reaction times at 60 s (6.2 % conversion), 300 s (17.4% conversion), and 600 s (32.6 % conversion) are shown in Figure 3.7b-d. Shorter PPM reaction times show H_3S^+ ions primarily at the polymer/air interface. The H_3S^+ ions show a deeper penetration of cystamine into the pSMA brush surface with longer PPM reaction times. At longer reaction times and higher anhydride conversions (Figure 3.7e-f), a relatively constant H_3S^+ ion intensity was observed throughout the brush structure. Figure 3.7f shows cystamine penetrating the full thickness of the brush at quantitative anhydride conversion (> 92.1 %).

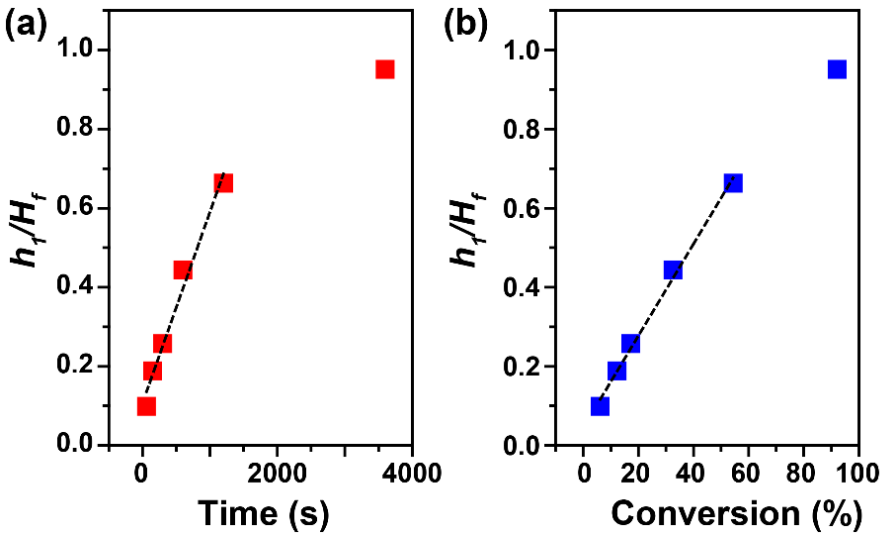

Figure 3.8 Ratio of cystamine-modified thickness (h_1) to total brush thickness (H_f) versus (a) cystamine modification time and (b) anhydride conversion. (H_o = 40 nm).

From the ToF-SIMS data, we calculated the cystamine-modified "skin" thickness (h_1) and final post-modified brush thickness (H_f) from the expression previously derived, assuming a frontal modification reaction. From these values, we generated kinetics plots

using the fractional thickness of the pSMA brush penetrated by cystamine (h_1/H_f) as a function of cystamine PPM reaction time (Figure 3.8a) and anhydride conversion (Figure 3.8b). The h_1/H_f ratio scales linearly with PPM time (up to 1000 s) and conversion (up to 55%) and then deviates at longer times and higher conversion – similar to the kinetics obtained by ellipsometry (Figure 3.6).

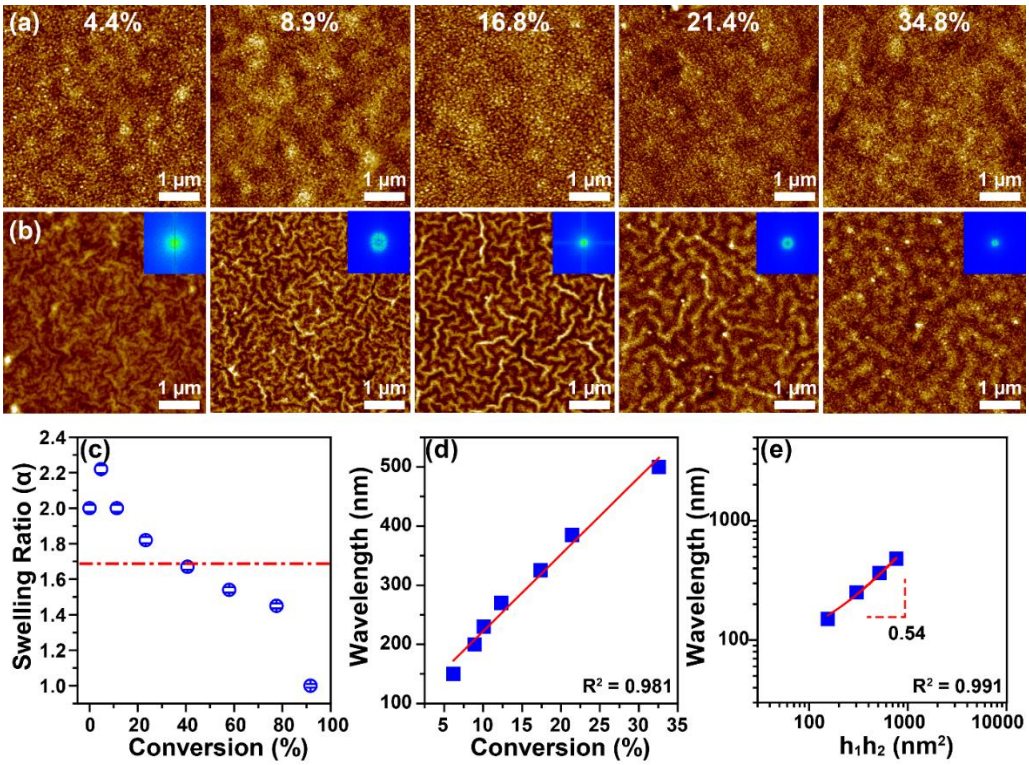

Figure 3.9 AFM height images of pSMA brushes (H_o = 40 nm) following (a) reaction with cystamine and (b) subsequent exposure to good solvent conditions. (c) Swelling ratio versus anhydride conversion. The horizontal line represents the critical swelling ratio. (d) Wavelength versus anhydride conversion. (e) Fit of wrinkle wavelength as a function of h_1h_2 demonstrating that the scaling relationship $\lambda \sim (h_1h_2)^{1/2}$ adequately describes the brush system.

After investigation of the through-thickness brush composition, the pSMA brushes were swelled in acetonitrile for 60 min to form the wrinkled morphologies. The AFM height images of the pSMA brushes show the featureless morphology prior to

swelling (Figure 3.9a) and labyrinth wrinkles after exposure to acetonitrile (Figure 3.9b). The inset images in Figure 3.9b are the 2D FFT power spectra, which were utilized to calculate the wrinkle wavelength. The swelling ratio (Figure 3.9c) and wrinkle wavelength (Figure 3.9d) were investigated as a function of conversion. The swelling ratio of the unmodified brush was ~ 2, with a critical swelling ratio ~1.7 (~ 40% anhydride conversion). The critical swelling ratio correlated to a h_1/H_f ratio of approximately 0.5. These values are consistent with the 80 nm pSMA brush surface. As expected, the wrinkle wavelength scales linearly with anhydride conversion (Figure 3.9d). The wrinkle wavelength ranges from approximately 150-500 nm. The smaller wrinkle morphologies are attributed to the smaller initial pSMA brush thickness. As shown in Figure 3.9e, wrinkle wavelength scales with the cystamine-modified thickness layer and the unmodified layer, $\lambda \sim (h_1 h_2)^{1/2}$, as previously derived for a rigid-on-soft multilayer construct. Thus, a lower cystamine-modified "skin" thickness and unmodified brush thickness resulted in a smaller wrinkle wavelength for the 40 nm pSMA brushes.

3.3.7 Buckling Instabilities in 120 nm pSMA Brush Surfaces

pSMA brush surfaces (H_o = 120 nm) were post-modified with cystamine under aqueous conditions at discrete reaction times. The conversion versus time plot for the cystamine modification of the pSMA brush is shown in Figure 3.10. For the 120 nm brushes, 80% conversion is reached at approximately 10000 seconds, whereas it was achievable within 1000s for the 40 nm pSMA brush and 3600 s for the 80 nm pSMA brush, respectively. Thus, an increase in brush thickness results in slower anhydride conversions due to larger steric constraints of the thicker polymer brushes.[33] These

kinetics studies demonstrate a method to judiciously control anhydride conversion based on polymer brush thickness.

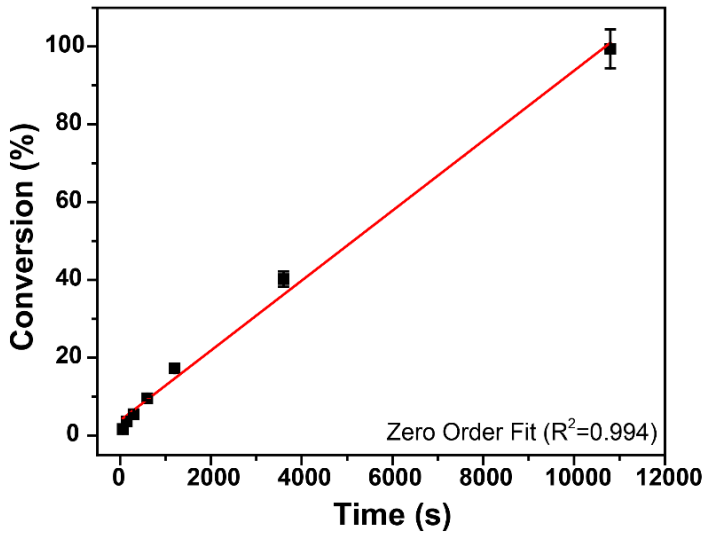

Figure 3.10 Anhydride conversion versus cystamine reaction time for pSMA brush (H_o = 120 nm) under poor solvent conditions.

ToF-SIMS analysis was employed to obtain depth-profiles of the 120 nm pSMA brushes as a function of cystamine modification time. Figure 3.11a shows the secondary ion profiles of an unmodified pSMA brush. The depth profiles for the cystamine-modified pSMA brushes post-modified under aqueous conditions with reaction times at 60 s (2.8% conversion), 300 s (5.5% conversion), 600 s (9.6% conversion), 1200 s (17.2% conversion), and 3600 s (40.2% conversion) are shown in Figure 3.11b-f. Shorter PPM reaction times show H_3S^+ ions primarily at the polymer/air interface. As expected, the H_3S^+ ions show a deeper penetration of cystamine into the pSMA brush surface with longer PPM reaction time.

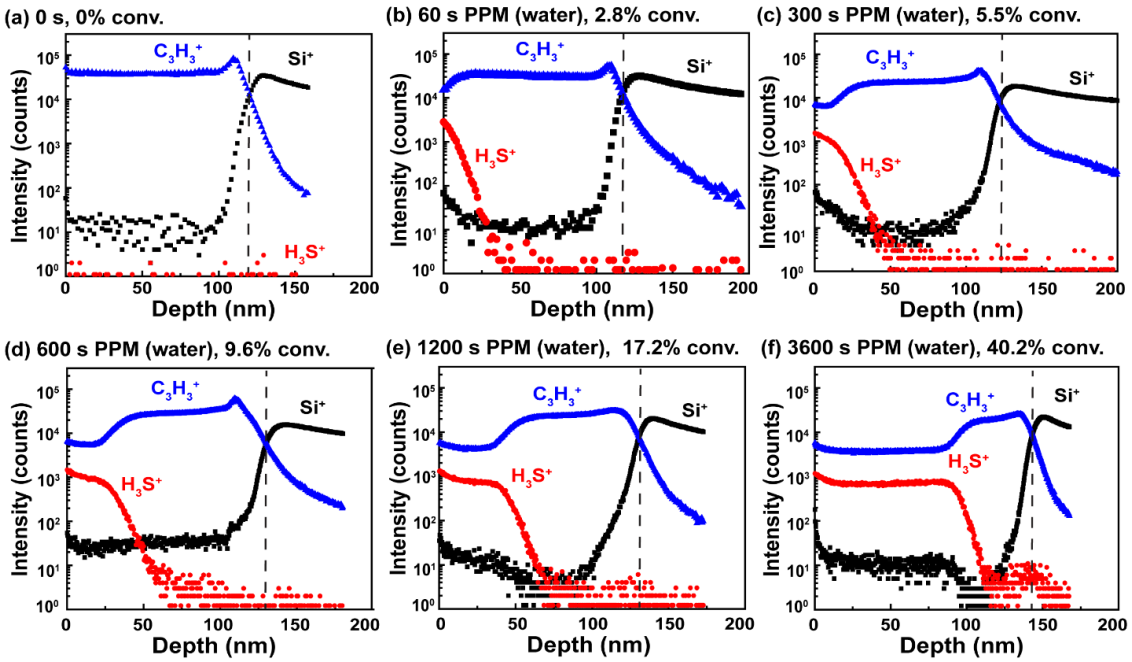

Figure 3.11 Secondary ion intensity−sputtering time profiles of unmodified and cystamine-modified pSMA brush samples. (a) 120 nm unmodified pSMA brush, cystamine-modified pSMA under aqueous conditions for (b) 60, (c) 300, (d) 600, (e) 1200 s, and (f) 3600 s. Anhydride conversion values are shown for each PPM time point. The vertical dashed line indicates the silicon/brush interface.

From the ToF-SIMS data, we calculated the cystamine-modified "skin" thickness (h_1) and final post-modified brush thickness (H_f) from the expression previously derived, assuming a frontal modification reaction. These values were used to generate kinetic plots using the fractional thickness of the pSMA brush penetrated by cystamine (h_1/H_f) as a function of cystamine PPM reaction time (Figure 3.12a) and anhydride conversion (Figure 3.12b). The h_1/H_f ratio scales linearly with PPM time (up to 4000 s) and conversion (up to 40%) and then deviates at longer times and higher conversion – similar to the kinetics obtained by ellipsometry for the 40 nm (Figure 3.6) and 80 nm (Figure 3.1) brush surfaces.

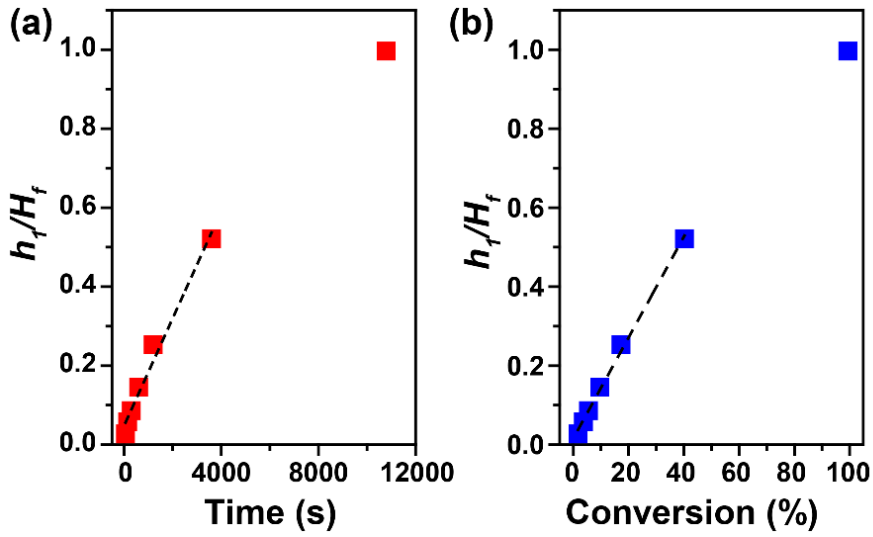

Figure 3.12 Ratio of cystamine-modified thickness (h_1) to total brush thickness (H_f) versus (a) cystamine modification time and (b) anhydride conversion. (H_o = 120 nm).

After investigation of the through-thickness brush composition, the pSMA brushes were swelled in acetonitrile for 60 min to form the wrinkled morphologies. The AFM height images of the pSMA brushes show the featureless morphology prior to swelling (Figure 3.13a) and labyrinth wrinkles after exposure to acetonitrile (Figure 3.13b). The swelling ratio (Figure 3.13c) and wrinkle wavelength (Figure 3.13d) were investigated as a function of anhydride conversion. The swelling ratio of the unmodified brush was ~ 1.8, with a critical swelling ratio ~1.7 (~ 40% anhydride conversion). This value is consistent with the 40 nm and 80 nm pSMA brush surfaces, indicating that anhydride conversions greater than ~ 40% do not induce surface buckling. The critical swelling ratio correlated to a h_1/H_f ratio of approximately 0.55, corroborating the previous data. As expected, the wrinkle wavelength scales linearly with anhydride conversion (Figure 3.13d). The wrinkle wavelength ranges from approximately 250 nm to 2.5 μm. As shown in Figure 3.13e, wrinkle wavelength scales with the cystamine-modified layer and unmodified layer, $\lambda \sim (h_1 h_2)^{1/2}$, with a slope of 0.46. As expected,

the higher cystamine-modified “skin” thickness and unmodified brush thickness values, compared to the 40 nm and 80 nm pSMA brushes, resulted in the largest wrinkle wavelengths.

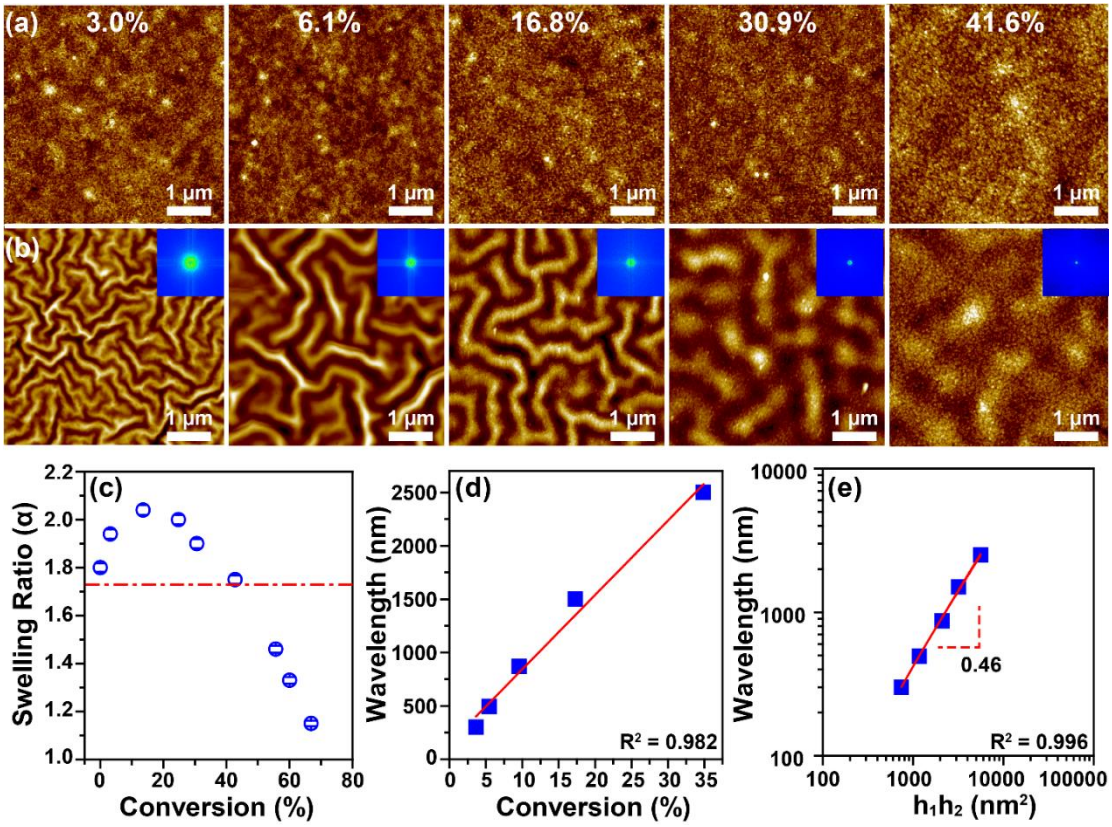

Figure 3.13 AFM height images of pSMA brushes (H_o= 120 nm) following (a) reaction with cystamine and (b) subsequent exposure to good solvent conditions. (c) Swelling ratio versus anhydride conversion. The horizontal line represents the critical swelling ratio. (d) Wavelength versus anhydride conversion. (e) Fit of wrinkle wavelength as a function of $h_1h_2$demonstrating that the scaling relationship $\lambda \sim (h_1h_2)^{1/2}$ adequately describes the brush system.

3.3.8 Redox-Driven Wrinkled Morphologies

Dynamic control of wrinkled morphologies has gained significant attention in the fields of smart surface adhesion,[5] wettability,[57] responsive microfluidic channels,[58] recycled templates,[59] and stretchable electronics.[15] Numerous methods to control wrinkle patterns have been exploited using reversible Diels-Alder chemistry,[60] visible[61] and near-

infrared light,[62] and redox chemistry.[63] Herein, we take advantage of the disulfide linkage in cystamine dihydrochloride as a handle to exploit reversible redox-driven wrinkle release and formation.

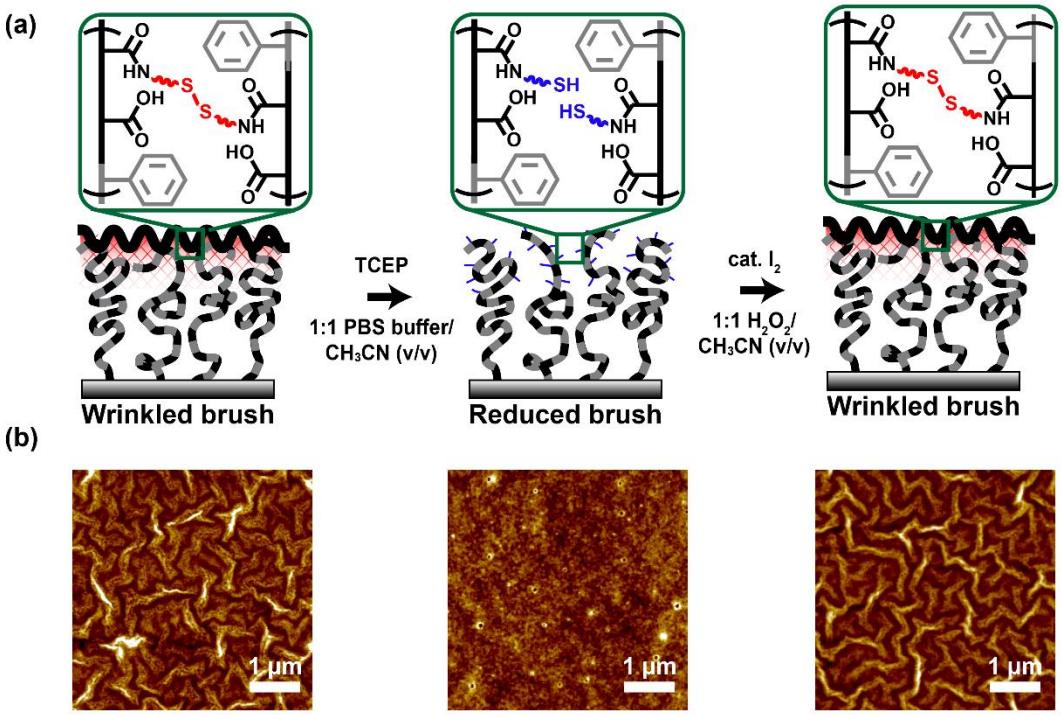

Figure 3.14 (a) Schematic illustration of disulfide reduction with TCEP to release wrinkles and sequential oxidation with I_2 to reform the disulfide bond and wrinkled morphology. (b) AFM height images of the wrinkled brush, reduced brush with TCEP, and wrinkled brush with I_2.

First, a wrinkled pSMA brush (H_o = 80 nm, λ ~ 300 nm) is subjected to reducing conditions (e.g., tris(2-carboxyethyl)phosphine (TCEP) in phosphate buffer), as illustrated in Figure 3.14a. Reduction of the disulfide linkage resulted in the release of the wrinkled morphologies and the formation of a featureless brush morphology, as shown in Figure 3.14b. The appearance of thiol functional groups within the brush following the TCEP reduction was confirmed by FTIR (S−H stretch, 2650 cm^{-1}, Figure B.3c). After the TCEP reduction, the free thiol moieties were oxidized (e.g., I_2 and 1:1 H_2O_2/MeCN by

volume) to reform the disulfide linkages. Upon reformation of the cystamine-modified "skin" layer and subsequent swelling, resulted in the reformation of the wrinkled morphologies. Furthermore, there were no obvious changes in the wrinkle wavelength (λ ~ 310 nm) after the reversible redox reaction. This result points to an opportunity to engineer brush surfaces with dynamic buckling behavior, where wrinkle formation and release are dictated via an external stimulus (e.g. redox chemistry).

3.4 Conclusion

In summary, we demonstrate a simple post-polymerization modification approach to engineer ultrathin polymer brush surfaces with tunable wrinkled morphologies. Cross-linking pSMA brushes under poor solvent conditions limits the post-modification reaction to the near surface region of the brush, where reaction time dictates the ultimate thickness of the cross-linked surface region. Exposure of the selectively cross-linked brush surface to good solvent conditions generates an in-plane compressive stress arising from a mismatch between lateral and perpendicular swelling directions within the brush. Above a critical swelling ratio of ~ 1.7-1.8 for pSMA brushes with an initial thickness of ($H_o = 40$ nm, 80 nm, and 120 nm), the imposed compressive stress causes an out-of-plane deformation of the untethered surface resulting in the observed wrinkled morphologies. The brush morphology can be tailored from nanoscale labyrinth-like wrinkles to microscale labyrinth-like wrinkles simply by manipulating the cross-linking time, while wrinkle wavelength scales according to $\lambda \sim (h_1 h_2)^{1/2}$. The initial pSMA brush thickness dictates anhydride conversion and the final wrinkle wavelength. Judicious manipulation of brush thickness allows control over the final observed wrinkled morphologies. Furthermore, we demonstrate a method to dynamically tune

wrinkled morphologies by reversible redox chemistry. We anticipate this simple approach will provide new routes to engineer ultrathin brush surfaces with complex functionality and morphology for a variety of applications.

3.5 Acknowledgments

CMR acknowledges support from the NSF Graduate Research Fellowship Program (DGE-1445151) and traineeship support from the NSF NRT program "Interface" (DGE-1449999) through the University of Southern Mississippi. The acquisition of the AFM instrumentation used in this work was enabled via partial funding from the Office of Naval Research (Award N00014-07-1-1057). The ToF-SIMS measurements were supported by a Rapid Access User Proposal for the Center for Nanophase Materials Sciences at Oak Ridge National Lab. We thank Dr. Olga Ovchinnikova, Dr. Anton Ievlev, and Dr. Bradley Lokitz for assistance with the ToF-SIMS measurements and data analysis.

3.6 References

(1) Cerda, E.; Mahadevan, L. Geometry and Physics of Wrinkling. *Phys. Rev. Lett.* **2003**, *90* (7), 074302. https://doi.org/10.1088/0264-9381/20/6/701.

(2) Tallinen, T.; Chung, J. Y.; Rousseau, F.; Girard, N.; Lefevre, J.; Mahadevan, L. On the Growth and Form of Cortical Convolutions. *Nat. Phys.* **2016**, *12*, 588–593.

(3) Hutchinson, J. W.; Thouless, M. D.; Liniger, E. G. Growth and Configurational Stability of Circular, Buckling-Driven Film Delaminations. *Acta Metall. Mater.* **1992**, *40* (2), 295–308. https://doi.org/10.1016/0956-7151(92)90304-W.

(4) Genzer, J.; Groenewold, J. Soft Matter with Hard Skin: From Skin Wrinkles to Templating and Material Characterization. *Soft Matter* **2006**, *2* (4), 310–323. https://doi.org/10.1039/b516741h.

(5) Chan, E. P.; Smith, E. J.; Hayward, R. C.; Crosby, A. J. Surface Wrinkles for Smart Adhesion. *Adv. Mater.* **2008**, *20* (4), 711–716. https://doi.org/10.1002/adma.200701530.

(6) Davis, C. S.; Crosby, A. J. Mechanics of Wrinkled Surface Adhesion. *Soft Matter* **2011**, *7* (11), 5373–5381. https://doi.org/10.1039/c1sm05146f.

(7) Davis, C. S.; Martina, D.; Creton, C.; Lindner, A.; Crosby, A. J. Enhanced Adhesion of Elastic Materials to Small-Scale Wrinkles. *Langmuir* **2012**, *28* (42), 14899–14908. https://doi.org/10.1021/la302314z.

(8) Jeong, H. E.; Kwak, M. K.; Suh, K. Y. Stretchable, Adhesion-Tunable Dry Adhesive by Surface Wrinkling. *Langmuir* **2010**, *26* (4), 2223–2226. https://doi.org/10.1021/la904290g.

(9) Li, Y.; Dai, S.; John, J.; Carter, K. R. Superhydrophobic Surfaces from Hierarchically Structured Wrinkled Polymers. *ACS Appl. Mater. Interfaces* **2013**, *5* (21), 11066–11073. https://doi.org/10.1021/am403209r.

(10) Zhang, Z.; Zhang, T.; Zhang, Y. W.; Kim, K. S.; Gao, H. Strain-Controlled Switching of Hierarchically Wrinkled Surfaces between Superhydrophobicity and Superhydrophilicity. *Langmuir* **2012**, *28* (5), 2753–2760. https://doi.org/10.1021/la203934z.

(11) Efimenko, K.; Finlay, J.; Callow, M. E.; Callow, J. A.; Genzer, J. Development and Testing of Hierarchically Wrinkled Coatings for Marine Antifouling. *ACS Appl. Mater. Interfaces* **2009**, *1* (5), 1031–1040. https://doi.org/10.1021/am9000562.

(12) Hoipkemeier-Wilson, L.; Schumacher, J. F.; Carman, M. L.; Gibson, A. L.; Feinberg, A. W.; Callow, M. E.; Finlay, J. A.; Callow, J. A.; Brennan, A. B. Antifouling Potential of Lubricious, Micro-Engineered, PDMS Elastomers against Zoospores of the Green Fouling Alga Ulva (Enteromorpha). *Biofouling* **2004**, *20* (1), 53–63. https://doi.org/10.1080/08927010410001662689.

(13) Wagner, S.; Lacour, S. P.; Jones, J.; Hsu, P. H. I.; Sturm, J. C.; Li, T.; Suo, Z. Electronic Skin: Architecture and Components. *Phys. E* **2004**, *25*, 326–334. https://doi.org/10.1016/j.physe.2004.06.032.

(14) Khang, D.-Y.; Jiang, H.; Huang, Y.; Rogers, J. A. A Stretchable Form of Single-Crystal Silicon for High-Performance Electronics on Rubber Substrates. *Science* **2006**, *311*, 208–212. https://doi.org/10.1126/science.1121401.

(15) Chan, E. P.; Crosby, A. J. Fabricating Microlens Arrays by Surface Wrinkling. *Adv. Mater.* **2006**, *18* (24), 3238–3242. https://doi.org/10.1002/adma.200601595.
(16) Bowden, N.; Brittain, S.; Evans, A. G.; Hutchinson, J. W.; Whitesides, G. M. Spontaneous Formation of Ordered Structures in Thin Films of Metals Supported on an Elastomeric Polymer. *Nature* **1998**, *393*, 146–149. https://doi.org/10.1038/30193
(17) Harrison, C.; Stafford, C. M.; Zhang, W.; Karim, A. Sinusoidal Phase Grating Created by a Tunably Buckled Surface. *Appl. Phys. Lett.* **2004**, *85* (18), 4016–4018. https://doi.org/10.1063/1.1809281.
(18) Meitl, M. A.; Zhu, Z. T.; Kumar, V.; Lee, K. J.; Feng, X.; Huang, Y. Y.; Adesida, I.; Nuzzo, R. G.; Rogers, J. A. Transfer Printing by Kinetic Control of Adhesion to an Elastomeric Stamp. *Nat. Mater.* **2006**, *5* (1), 33–38. https://doi.org/10.1038/nmat1532.
(19) Khare, K.; Zhou, J.; Yang, S. Tunable Open-Channel Microfluidics on Soft Poly(Dimethylsiloxane) (PDMS) Substrates with Sinusoidal Grooves. *Langmuir* **2009**, *25* (21), 12794–12799. https://doi.org/10.1021/la901736n.
(20) Bae, H. J.; Bae, S.; Park, C.; Han, S.; Kim, J.; Kim, L. N.; Kim, K.; Song, S. H.; Park, W.; Kwon, S. Biomimetic Microfingerprints for Anti-Counterfeiting Strategies. *Adv. Mater.* **2015**, *27* (12), 2083–2089. https://doi.org/10.1002/adma.201405483.
(21) Rodriguez-Hernandez, J. Wrinkled Interfaces: Taking Advantage of Surface Instabilities to Pattern Polymer Surfaces. *Prog. Polym. Sci.* **2015**, *42*, 1–41. https://doi.org/10.1016/j.progpolymsci.2014.07.008.
(22) Yang, S.; Khare, K.; Lin, P. C. Harnessing Surface Wrinkle Patterns in Soft Matter. *Adv. Funct. Mater.* **2010**, *20* (16), 2550–2564. https://doi.org/10.1002/adfm.201000034.
(23) Chen, D.; Yoon, J.; Chandra, D.; Crosby, A. J.; Hayward, R. C. Stimuli-Responsive Buckling Mechanics of Polymer Films. *J. Polym. Sci. Part B Polym. Phys.* **2014**, *52* (22), 1441–1461. https://doi.org/10.1002/polb.23590.
(24) Das, A.; Banerji, A.; Mukherjee, R. Programming Feature Size in the Thermal Wrinkling of Metal Polymer Bilayer by Modulating Substrate Viscoelasticity. *ACS Appl. Mater. Interfaces* **2017**, *9* (27), 23255–23262. https://doi.org/10.1021/acsami.7b08333.
(25) Bowden, N.; Huck, W. T. S.; Paul, K. E.; Whitesides, G. M. The Controlled Formation of Ordered, Sinusoidal Structures by Plasma Oxidation of an Elastomeric Polymer. *Appl. Phys. Lett.* **1999**, *75* (17), 2557–2559. https://doi.org/10.1063/1.125076.
(26) Chandra, D.; Crosby, A. J. Self-Wrinkling of UV-Cured Polymer Films. *Adv. Mater.* **2011**, *23* (30), 3441–3445. https://doi.org/10.1002/adma.201101366.
(27) Guvendiren, M.; Burdick, J. A.; Yang, S. Solvent Induced Transition from Wrinkles to Creases in Thin Film Gels with Depth-Wise Crosslinking Gradients. *Soft Matter* **2010**, *6* (22), 5795–5801. https://doi.org/10.1039/c0sm00317d.
(28) Huang, H.; Chung, J. Y.; Nolte, A. J.; Stafford, C. M. Characterizing Polymer Brushes via Surface Wrinkling. *Chem. Mater.* **2007**, *19* (26), 6555–6560. https://doi.org/10.1021/cm702456u.

(29) Singamaneni, S.; McConney, M. E.; Tsukruk, V. V. Spontaneous Self-Folding in Confined Ultrathin Polymer Gels. *Adv. Mater.* **2010**, *22* (11), 1263–1268. https://doi.org/10.1002/adma.200903052.
(30) Singamaneni, S.; McConney, M. E.; Tsukruk, V. V. Swelling-Induced Folding in Confined Nanoscale Responsive Polymer Gels. *ACS Nano* **2010**, *4* (4), 2327–2337. https://doi.org/10.1021/nn901886y.
(31) Ortiz, O.; Vidyasagar, A.; Wang, J.; Toomey, R. Surface Instabilities in Ultrathin, Cross-Linked Poly(N- Isopropylacrylamide) Coatings. *Langmuir* **2010**, *26* (22), 17489–17494. https://doi.org/10.1021/la1028146.
(32) Arnold, R. M.; Patton, D. L.; Popik, V. V.; Locklin, J. A Dynamic Duo: Pairing Click Chemistry and Postpolymerization Modification to Design Complex Surfaces. *Acc. Chem. Res.* **2014**, *47* (10), 2999–3008. https://doi.org/10.1021/ar500191m.
(33) Schuh, C.; Rühe, J. Penetration of Polymer Brushes by Chemical Nonidentical Free Polymers. *Macromolecules* **2011**, *44* (9), 3502–3510. https://doi.org/10.1021/ma102410z.
(34) Schüwer, N.; Geue, T.; Hinestrosa, J. P.; Klok, H. A. Neutron Reflectivity Study on the Postpolymerization Modification of Poly(2-Hydroxyethyl Methacrylate) Brushes. *Macromolecules* **2011**, *44* (17), 6868–6874. https://doi.org/10.1021/ma201069d.
(35) Barbey, R.; Laporte, V.; Alnabulsi, S.; Klok, H. Postpolymerization Modification of Poly(Glycidyl Methacrylate) Brushes: An XPS Depth-Profiling Study. *Macromolecules* **2013**, *46*, 6151–6158.
(36) Brooks, K.; Razavi, M. J.; Wang, X.; Locklin, J. Nanoscale Surface Creasing Induced by Post-Polymerization Modification. *ACS Nano* **2015**, *9* (11), 10961–10969. https://doi.org/10.1021/acsnano.5b04144.
(37) Brooks, K.; Razavi, M. J.; White, E. M.; Wang, X.; Locklin, J. The Formation and Evolution of Creased Morphologies Using Reactive Diffusion in Ultrathin Polymer Brush Platforms. *Adv. Mater. Interfaces* **2017**, *4* (13), 1–7. https://doi.org/10.1002/admi.201700084.
(38) Patton, D. L.; Page, K. A.; Xu, C.; Genson, K. L.; Fasolka, M. J.; Beers, K. L. Measurement of Reactivity Ratios in Surface-Initiated Radical Copolymerization. *Macromolecules* **2007**, *40*, 6017–6020.
(39) Patton, D. L.; Page, K. A.; Hoff, E. A.; Fasolka, M. J.; Beers, K. L. A Robust and High-Throughput Measurement Platform for Monomer Reactivity Ratios from Surface-Initiated Polymerization. *Polym. Chem.* **2012**, *3* (5), 1174–1181. https://doi.org/10.1039/c2py20023f.
(40) Murata, H.; Prucker, O.; Rühe, J. Synthesis of Functionalized Polymer Monolayers from Active Ester Brushes. *Macromolecules* **2007**, *40* (15), 5497–5503. https://doi.org/10.1021/ma0624550.
(41) Hasanzadeh, R.; Moghadam, P. N.; Samadi, N.; Asri-Rezaei, S. Removal of Heavy-Metal Ions from Aqueous Solution with Nanochelating Resins Based on Poly(Styrene-Alt-Maleic Anhydride). *J. Appl. Polym. Sci.* **2013**, *127* (4), 2875–2883. https://doi.org/10.1002/app.36793.
(42) Marquardt, F.-H. The Intensity of Carbonyl Bands in the Infrared Spectra of

Cyclic Anhydrides of Dicarboxylic Acids. *J. Chem. Soc. B.* **1966**, 1242–1243.
(43) Alswieleh, A. M.; Cheng, N.; Leggett, G. J.; Armes, S. P. Spatial Control over Cross-Linking Dictates the PH-Responsive Behavior of Poly(2-(Tert - Butylamino)Ethyl Methacrylate) Brushes. *Langmuir* **2014**, *30* (5), 1391–1400. https://doi.org/10.1021/la403666y.
(44) Arnold, R. M.; Sheppard, G. R.; Locklin, J. Comparative Aminolysis Kinetics of Different Active Ester Polymer Brush Platforms in Postpolymerization Modification with Primary and Aromatic Amines. *Macromolecules* **2012**, *45* (13), 5444–5450. https://doi.org/10.1021/ma3005839.
(45) Yatvin, J.; Brooks, K.; Locklin, J. SuFEx on the Surface: A Flexible Platform for Postpolymerization Modification of Polymer Brushes. *Angew. Chemie - Int. Ed.* **2015**, *54* (45), 13370–13373. https://doi.org/10.1002/anie.201506253.
(46) Cyriac, J.; Pradeep, T.; Kang, H.; Souda, R.; Cooks, R. G. Low-Energy Ionic Collisions at Molecular Solids. *Chem. Rev.* **2012**, *112* (10), 5356–5411. https://doi.org/10.1021/cr200384k.
(47) Navarro, M.; Benetti, E. M.; Zapotoczny, S.; Planell, J. A.; Vancso, G. J. Buried, Covalently Attached RGD Peptide Motifs in Poly(Methacrylic Acid) Brush Layers: The Effect of Brush Structure on Cell Adhesion. *Langmuir* **2008**, *24* (19), 10996–11002. https://doi.org/10.1021/la800999y.
(48) Tirumala, V. R.; Stafford, C. M.; Ocola, L. E.; Douglas, J. F.; Mahadevan, L. Geometric Control of Rippling in Supported Polymer Nanolines. *Nano Lett.* **2012**, *12* (3), 1516–1521. https://doi.org/10.1021/nl204306q.
(49) Biesalski, M.; Rühe, J. Scaling Laws for the Swelling of Neutral and Charged Polymer Brushes in Good Solvents. *Macromolecules* **2002**, *35* (2), 499–507. https://doi.org/10.1021/ma001776n.
(50) Han, Q.; Li, C.; Guan, Y.; Zhu, X. X.; Zhang, Y. Swelling-Induced Surface Instability of a Hydrogen-Bonded LBL Film. *Polymer (Guildf).* **2014**, *55* (9), 2197–2204. https://doi.org/10.1016/j.polymer.2014.03.015.
(51) Flory, P. J.; Rehner, J. Statistical Mechanics of Cross-Linked Polymer Networks II. Swelling. *J. Chem. Phys.* **1943**, *11* (11), 521–526. https://doi.org/10.1063/1.1723792.
(52) Park, H. G.; Jeong, H. C.; Jung, Y. H.; Seo, D. S. Control of the Wrinkle Structure on Surface-Reformed Poly(Dimethylsiloxane) via Ion-Beam Bombardment. *Sci. Rep.* **2015**, *5*, 1–8. https://doi.org/10.1038/srep12356.
(53) Huang, Z. Y.; Hong, W.; Suo, Z. Nonlinear Analyses of Wrinkles in a Film Bonded to a Compliant Substrate. *J. Mech. Phys. Solids* **2005**, *53* (9), 2101–2118. https://doi.org/10.1016/j.jmps.2005.03.007.
(54) Chan, E. P.; Lin, Q.; Stafford, C. M. Quantifying the Elasticity and Viscosity of Geometrically Confined Polymer Films via Thermal Wrinkling. *J. Polym. Sci. Part B Polym. Phys.* **2012**, *50* (22), 1556–1561. https://doi.org/10.1002/polb.23152.
(55) Vandeparre, H.; Léopoldès, J.; Poulard, C.; Desprez, S.; Derue, G.; Gay, C.; Damman, P. Slippery or Sticky Boundary Conditions: Control of Wrinkling in Metal-Capped Thin Polymer Films by Selective Adhesion to Substrates. *Phys. Rev. Lett.* **2007**, *99* (18), 2–5. https://doi.org/10.1103/PhysRevLett.99.188302.
(56) Prucker, O.; Rühe, J. Polymer Layers through Self-Assembled Monolayers of

Initiators. *Langmuir* **1998**, *14* (24), 6893–6898. https://doi.org/10.1021/la971035o.
(57) Cao, C.; Chan, H. F.; Zang, J.; Leong, K. W.; Zhao, X. Harnessing Localized Ridges for High-Aspect-Ratio Hierarchical Patterns with Dynamic Tunability and Multifunctionality. *Adv. Mater.* **2014**, *26* (11), 1763–1770. https://doi.org/10.1002/adma.201304589.
(58) Kim, H. S.; Crosby, A. J. Solvent-Responsive Surface via Wrinkling Instability. *Adv. Mater.* **2011**, *23* (36), 4188–4192. https://doi.org/10.1002/adma.201101477.
(59) Lee, S. G.; Kim, H.; Choi, H. H.; Bong, H.; Park, Y. D.; Lee, W. H.; Cho, K. Evaporation-Induced Self-Alignment and Transfer of Semiconductor Nanowires by Wrinkled Elastomeric Templates. *Adv. Mater.* **2013**, *25* (15), 2162–2166. https://doi.org/10.1002/adma.201203687.
(60) Hou, H.; Yin, J.; Jiang, X. Reversible Diels–Alder Reaction To Control Wrinkle Patterns: From Dynamic Chemistry to Dynamic Patterns. *Adv. Mater.* **2016**, *28* (41), 9126–9132. https://doi.org/10.1002/adma.201602105.
(61) Zong, C.; Zhao, Y.; Ji, H.; Han, X.; Xie, J.; Wang, J.; Cao, Y.; Jiang, S.; Lu, C. Tuning and Erasing Surface Wrinkles by Reversible Visible-Light-Induced Photoisomerization. *Angew. Chemie - Int. Ed.* **2016**, *55* (12), 3931–3935. https://doi.org/10.1002/anie.201510796.
(62) Li, F.; Hou, H.; Yin, J.; Jiang, X. Near-Infrared Light–responsive Dynamic Wrinkle Patterns. *Sci. Adv.* **2018**, *4* (4), 1–9. https://doi.org/10.1126/sciadv.aar5762.
(63) Xie, J.; Zong, C.; Han, X.; Ji, H.; Wang, J.; Yang, X.; Lu, C. Redox-Switchable Surface Wrinkling on Polyaniline Film. *Macromol. Rapid Commun.* **2016**, *37* (7), 637–642. https://doi.org/10.1002/marc.201500700.

CHAPTER IV – QUANTIFYING STRAIN VIA BUCKLING INSTABILITIES IN SURFACE MODIFIED POLYMER BRUSHES

4.1 Introduction

Buckling instabilities lead to ubiquitous features in nature over a wide range of length scales (i.e. nanometer to meter). Common examples in everyday life are wrinkling in the skin, imperfectly cured coatings, and thin rigid materials expanding while being bound to a compliant polymer film.[1,2] In the buckling of thin films, the geometry is typically comprised of a thin, stiff coating (e.g. "skin" layer) adhered to a thick, compliant substrate. A compressive strain, arising from any one of a variety of stimuli (e.g. mechanical, thermal, or osmotic), can lead to a buckled or wrinkled morphology having a characteristic wrinkle wavelength and amplitude.[3] Significant efforts have focused on exploiting this approach to design surfaces for a wide range of applications in stretchable electronics,[4–6] tunable optics,[7–9] and anti-counterfeit technologies.[10] In addition to the vast number of ways to tune the resulting wrinkled morphology, these instabilities have also been used as a metrology platform for characterizing mechanical properties of thin films.[11–13]

Since the early work of buckled surfaces by Whitesides and coworkers,[14–16] there has been significant effort to develop a comprehensive physical understanding of the surface instability phenomena, particularly in thin polymer films. The mechanics of buckling or wrinkling relate the characteristic length scale of the instability (typically the wavelength) to the mechanical properties of the skin and substrate. Consequently, Stafford et al. developed metrologies to quantify properties of both skin and substrate, such as the elastic moduli,[7,17] residual stress,[18] and viscoelastic properties,[19] through

detailed measurement of the wrinkle wavelength and amplitude as a function of applied strain. These approaches have proven useful in characterizing a number of polymer films and other materials.[11] However, in some systems, the applied strain is unknown or unmeasurable, particularly in solvent swelling or thermally-induced wrinkling of bilayer films. For example, solvent-induced swelling of oxidized poly(dimethylsiloxane) (PDMS) leads to surface wrinkles due to differential swelling of the bilayer film.[20,21] Similarly, Chan et al. demonstrated thermal wrinkling of a polyhydroxystyrene film sandwiched between a silicon substrate and aluminum thin film superstrate.[13] The difference in coefficients of thermal expansion between the layers results in a compressive stress at the polymer-superstrate interface when heated to elevated temperatures.[19] Above a critical compressive stress, wrinkles develop on the superstrate surface. In both cases, the applied strain due to swelling or thermal contraction was unknown. Therefore, the ability to measure applied strain for systems where the strain is unknown may be integrated into buckling-based metrologies for investigating the mechanical properties of thin film systems. For example, knowledge of the applied strain may be useful to quantify other properties in buckled thin films (e.g. persistence lengths of aligned wrinkles).[22–24]

Ultrathin polymer brush films, in particular, are well-known for their unique physico-chemical properties; however, measuring the applied strain in buckled polymer brushes remains a significant challenge. For example, Huang et al. demonstrated thermal wrinkling of poly(2-hydroxyethyl methacrylate) polymer brushes tethered to a PDMS substrate.[25] Heating the bilayer above the glass transition temperature of the brush and cooling it back to room temperature placed the film under compressive stress,

inducing surface wrinkling. The critical temperature at which wrinkles were observed can be related to the critical strain necessary to induce wrinkling. Although they were able to determine the Young's modulus of the polymer brush/PDMS bilayer, the applied strain for this system was unknown.

In Chapter III, we reported a simple route to wrinkled poly(styrene-alt-maleic anhydride) (pSMA) brush surfaces via PPM techniques, where the wrinkle wavelength can be tuned using PPM reaction time and anhydride conversion.[26] PPM with a diamine modifier (cystamine) under poor solvent (aqueous) conditions limits cross-linking to the near surface region of the brush in a front-like process. This frontal modification reaction divides the brush into two distinct regions: a cystamine-modified "skin" thickness (h_1) and an unmodified thickness (h_2) that is covalently grafted to a rigid silicon support. Exposure to good solvent (acetonitrile) generated a compressive stress arising from a swelling mismatch between the perpendicular and lateral directions within the brush. Above a critical swelling ratio of 1.8, the stress causes an out-of-plane deformation of the untethered surfaces resulting in the observed wrinkled morphologies. From this work, we were able to establish a linear relationship between wrinkle wavelength (λ) and anhydride conversion. Furthermore, we established a linear scaling relationship for a rigid-on-soft multilayer construct, $\lambda \sim (h_1 h_2)^{1/2}(E_{h_1} E_{h_2})^{1/6}$, where E_{h_1} and E_{h_2} are the Young's moduli of the "skin" layer and unmodified layer, respectively.

Although we were able to quantify swelling ratios that result in the observed wrinkled morphologies, we lacked the ability to determine the applied swelling strain which led to the observed buckling instabilities. This measurement would be straightforward if we were able to determine the modulus of the "skin" and unmodified

regions within the brush individually. However, this remains a significant challenge in polymer brush surfaces, thus we derive an expression to deduce the compressive strain of wrinkled pSMA brushes by measuring cystamine-modified "skin" thickness, wrinkle wavelength, and wrinkle amplitude. First, we validate the derived expression using surface wrinkling of a prototypical model system, e.g., polystyrene (PS) film mounted onto a PDMS substrate. Next, we utilize the derived expression to quantify applied strain of wrinkled pSMA brush surfaces. Finally, knowledge of the applied strain allows us to make predictions about persistence lengths of aligned wrinkles via AFM lithography.

4.2 Experimental Section

4.2.1 Materials

Maleic anhydride (MA), acetonitrile, cystamine dihydrochloride, triethylamine, were purchased from Sigma-Aldrich and were used as received. Styrene (Sty) was purchased from Sigma-Aldrich and was purified by passing through an alumina column to remove inhibitor before use. Silica wafers (orientation <100>, native oxide) were purchased from University Wafer. Plasma cleaning of silicon substrates was done on plasma cleaner from Harrick Plasma.

4.2.2 Instrumentation and Characterization

Ellipsometry measurements were carried out using a Gartner Scientific Corporation LSE ellipsometer with a 632.8 nm laser at 70° from the normal. *In situ* ellipsometry measurements were carried out using a home-build liquid cell with windows normal to the direction of the incident light. The *in situ* measurements were conducted for 60 min. Refractive indices (RI) of swollen polymer brushes were estimated using a linear effective medium approximation based on the RI of dry polymer and solvent. The

RI of solvent acetonitrile was 1.339. Thickness measurements of PS films were measured using reflectance interferometry (minimum of 10 measurements per sample). Measurements were conducted using a Model F20 Filmetrics interferometer at the National Institute of Standards and Technology (NIST). A Jetlight (Model 342) ultraviolet-ozone cleaner was used at NIST to oxidize the PS surfaces and induce surface hydrophilicity. Atomic force microscopy (AFM) was performed using a Bruker Dimension Icon instrument. AFM height images were collected in tapping mode (in air) to obtain thin film morphology. The polymer brush samples were scanned using RTESPA-300 probes (from Bruker) with a spring constant of 40 N/m. The AFM height images were analyzed using the SPIP software. The wrinkle wavelengths were obtained from the radial averaged cross-section of the 2D fast Fourier transform (FFT) power spectrum of the height image. The 2D FFT power spectrum converts the wrinkle pattern from a spatial frequency domain to a spatial domain. The wrinkle amplitudes were calculated from the spectral RMS amplitude values of an AFM image. Specifically, a line section analysis was performed on each image using Nanoscope Analysis software with an average of 20 line sections was utilized to minimize error in the measurement. AFM lithography was performed on the same instrument with Aspire CT300-10 probe with a spring constant of 40 N/m in contact mode (in air). The persistence lengths were measured using a previously reported procedure.[20,27,28] In brief, persistence lengths were measured by drawing contour lengths using the "freehand line tool" in ImageJ 1.51a[29] software. The contour lengths were smoothed using the weighted average of five contiguous coordinates. Ten contours were drawn for each image. Tangent vectors were

drawn separated by a distance s along the contour length. The angle (θ) between the tangent vectors was measured and persistence length ξ was calculated according to:

$$\langle \cos(\theta(s)) \rangle = e^{-s/2\xi}$$

where $\langle \cos(\theta(s)) \rangle$ is the average cosine of the θ between the tangent vectors. Three angles between the tangent vectors were measured for each contour, resulting in 30 total measurements. The results were averaged to obtain the final averaged persistence length for each AFM image.

4.2.3 Surface-Initiated Polymerization of pSMA Brush

An azo-based trichlorosilane initiator was used and it was synthesized following literature procedures.[30,31] Silicon substrates were cleaned and functionalized with the azo-based initiator following the procedures reported in the previous chapters. An oxygen free solution containing styrene (1.0 mL, 0.91 g, 8.7 mmol), maleic anhydride (1.0 g, 10.2 mol) and anhydrous acetonitrile (10.0 mL) was prepared and was transferred into a test tube that contains an initiator modified silicon substrate under nitrogen protection. The test tube was heated at 95 °C for various times to obtain polymer brushes of different thickness. After heating, the pSMA substrate was thoroughly rinsed with acetonitrile and dried under a flow of nitrogen.

4.2.4 PPM of pSMA Brush with Cystamine Dihydrochloride under Aqueous Conditions

Cystamine dihydrochloride (40 mg, 0.18 mmol) and triethylamine (40 μL, 29 mg, 0.29 mmol) were dissolved in 4.0 mL of DI water. A substrate with pSMA brush on the surface was placed in the cystamine solution at discrete reaction times (from 30 s to 3 h).

After PPM, the polymer brush substrate was thoroughly rinsed with DI water and dried with a flow of nitrogen.

4.2.5 Calculation of Brush Thickness Parameters

Cystamine post-modification of a pSMA brush to near-quantitative conversion (k) results in a 66% increase in thickness (H_0 = 77.9 nm, H_f= 129.8 nm, or 1.66H_0). Assuming the post-modification reactions occurs in a front-like process, the brush is divided into two distinct regimes: a cystamine-modified "skin" layer (h_1) and an unmodified brush layer (h_2). Using this model, we can establish the following relationships, where the cystamine-modified skin thickness layer is

$$h_1 = (1.66H_0)k$$

the unmodified thickness layer is

$$h_2 = H_0(1 - k)$$

and the final total brush thickness is

$$H_f = h_1 + h_2$$

Utilizing these relationships, a pSMA brush ($H_0 = 84.5$) and conversion of 9.9% results in predicted values for $h_1 = 13.8$ nm, $h_2 = 76.1$ nm and $H_f = 89.9$ nm.

4.2.6 Sample Preparation for Wrinkling

The following sample preparation and wrinkle measurements for the PS on PDMS model system were performed at NIST. PDMS was prepared by mixing Sylgard 184 at a ratio of 20:1 by mass of base to cross-linker, casting onto a large glass plate, allowing the PDMS pre-polymer to flow and level overnight at room temperature, and final curing at 75 °C for 2 h in a convection oven. Then, 25 mm × 75 mm coupons were

cut out and clamped onto a custom-built strain-stage.[32] A 5 % pre-strain (50 mm to 52.5 mm) was applied to the PDMS coupon by elongation using a strain stage.

Separately, a silicon wafer (silicon 100, University Wafers) was cleaned in an ultraviolet light-ozone chamber for 20 min to render the surface hydrophilic. Poly(styrene sulfonate) (PSS) was spin coated onto the wafer from distilled water, followed by spin coating of atactic PS (Aldrich, M_w= 2.80 x 10^5, M_w/M_n = 3.07) from toluene. The PSS layer was used as a sacrificial layer to facilitate expedient film transfer. The thickness of the initial PSS layer and the total film thickness (PSS+PS) was measured by spectral reflectometry (Filmetrics F-20), and the PS thickness was taken to be the difference between the two measured values. The spin-coated wafer was then diced to form clean, fresh edges, and placed onto the pre-stressed PDMS substrate. The strain stage was immersed in water, releasing the film from the silicon wafer and thus transferring it to PDMS. The entire stage is removed and gently dried with nitrogen. The strain stage was placed under an AFM for *in situ* measurements of wavelength and amplitude. For this study, a displacement increment of 0.25 mm was used, corresponding to a strain increment of ≈0.5%. A total of ten 0.25 mm increments were exploited for the *in situ* measurements.

4.3 Results and Discussion

4.3.1 Calculating Compressive Strain of Wrinkled PS on PDMS

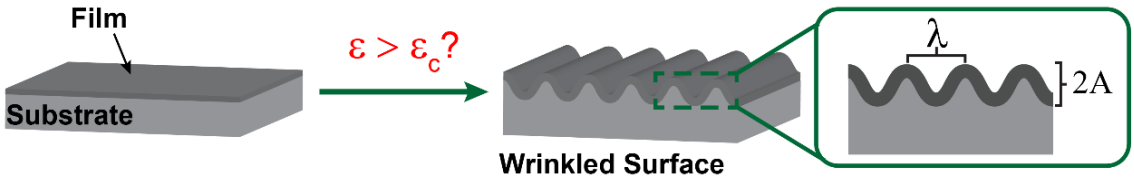

Scheme 4.1 Schematic illustration of wrinkles developing in a bilayer film (e.g. stiff, thin film bonded to a thick, compliant substrate). λ and A represent the wrinkle wavelength and amplitude. The applied strain (ε) above the critical strain (ε_c) is unknown.

The derived expression to deduce the applied compressive strain is validated using the prototypical bilayer system (e.g. stiff, thin film bonded to a thick, compliant substrate) as shown in Scheme 4.1. Although the wrinkled pSMA brush system represents a confined system, this bilayer model system is used as a first approximation to establish the following derivation. When a small uniaxial compressive strain, ε, above a critical strain, ε_c, is applied to the bilayer film, the system wrinkles and the wrinkling wavelength λ can be expressed as[24,33]

$$\lambda = 2\pi h_1 \left(\frac{\bar{E}_1}{3\bar{E}_2}\right)^{1/3} \qquad \text{Equation 1}$$

where h is the thickness, $\bar{E} = E/(1-v^2)$ is the plane-strain modulus, E is the Young's modulus, and v is Poisson's ratio. The subscripts *1* and *2* denote the PS film and the underlying PDMS substrate, respectively. Once a wrinkle wavelength is established, further strain is accommodated by increasing the wrinkle amplitude, A.

$$A^2 = {h_1}^2 \left(\frac{\varepsilon}{\varepsilon_c} - 1\right) \qquad \text{Equation 2}$$

The critical strain can be expressed as[34,35]

$$\varepsilon_c = \frac{1}{4}\left(\frac{3\bar{E}_2}{\bar{E}_1}\right)^{2/3} \qquad \text{Equation 3}$$

Equation 1 and 3 can be combined to give

$$\varepsilon_c = \frac{\pi^2 h_1^2}{\lambda^2} \qquad \text{Equation 4}$$

which can then be substituted into equation 2 to yield an expression relating applied compressive strain (ε), wrinkle wavelength (λ), wrinkle amplitude (A), and skin thickness (h_1):

$$\varepsilon = \frac{\pi^2}{\lambda^2}(A^2 + h_1^2) \qquad \text{Equation 5}$$

To the best of our knowledge, this relationship has yet to be established in the literature. The expression given in equation 5 will allow us to deduce the applied strain without any prior knowledge of the modulus ratio between the film and the substrate, as this ratio is embedded in the wrinkle wavelength. This is critical in the polymer brush system, as the modulus of the modified skin layer and the underlying brush layer are difficult to assess in any quantitative fashion.

In this work, we utilize poly(styrene) (PS) supported on a soft elastic substrate of poly(dimethylsiloxane) (PDMS) as a model system (Scheme 4.2a) to validate equation 5. The PS on PDMS system was chosen since there has been significant work on this bilayer construct.[18,32,36] Furthermore, this bilayer film exhibits a reasonable critical strain ($\varepsilon \sim 1.1$ %) given the modulus ratio (e.g. PDMS has an elastic modulus of ≈ 1.8 MPa and a Poisson's ratio of 0.50, and PS has a modulus of ≈ 3.7 GPa and a Poisson's ratio of 0.33).[18,37] The tackiness of PDMS also facilitates easy film transfer of PS, which makes this an attractive model system for wrinkling. The PDMS substrate was clamped onto a

strain stage and pre-strained by elongating 5 %. The PS/PDMS bilayer was prepared by transferring a spin cast PS film from a silicon wafer to a pre-strained PDMS substrate using aqueous immersion.[7,11,32] Three PS films were prepared with thicknesses of 96 nm, 110 nm, and 158 nm and transferred to the pre-strained PDMS substrate, individually. After film transfer, the wrinkling instability was initiated by incrementally releasing the pre-strain on the PDMS, resulting in compression of the attached polymer film. The strain stage was placed under an atomic force microscope (AFM) for *in situ* measurements of wavelength and amplitude. For this study, a displacement increment of 0.25 mm was used, corresponding to a strain increment of ≈ 0.5%. A total of ten increments were exploited for the *in situ* measurements.

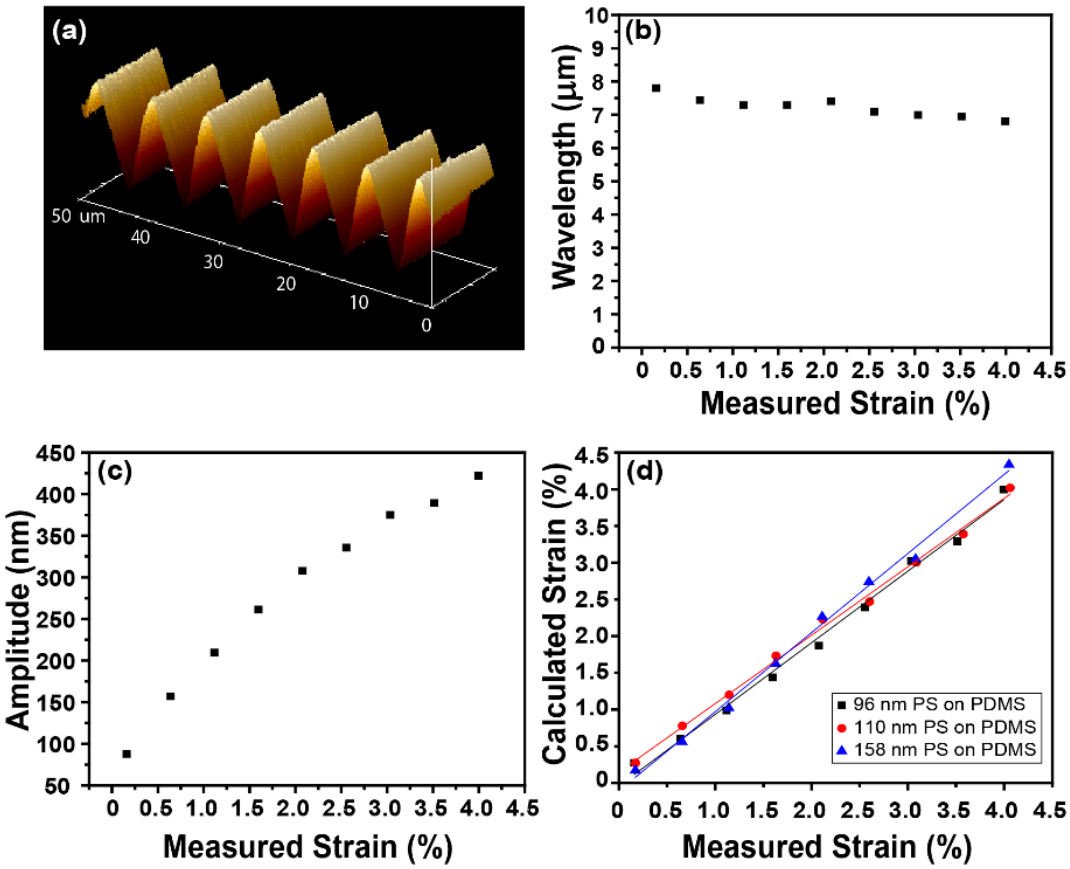

Figure 4.1 (a) AFM image of PS (h_1= 96 nm) on PDMS wrinkled at 2.1 % compressional strain. (b) Wavelength and (c) amplitude as a function of applied strain for 96 nm PS on PDMS. (d) Calculated versus measured applied strain for PS thicknesses (h_1) of 96 nm, 110 nm, and 158 nm.

Figure 4.1a shows an AFM micrograph for PS (h_1 = 96 nm) on PDMS at 2.1 % compressional strain. Figure 4.1b shows that wavelength remains relatively constant as a function of strain (by equation 1, λ is independent of ε). However, the amplitude can be seen to grow non-linearly with strain ($A \sim \varepsilon^{1/2}$, equation 2), increasing to 422 nm at 4 % strain (Figure 4.1c). The relationship between wavelength, amplitude and strain for the 110 nm and 158 nm PS on PDMS are provided in Appendix C. From these data (e.g. λ, A, h_1), we utilized equation 5 to calculate the applied compressive strain and compared it to the measured strain for all three bilayer films. However, it is important to note that we must also account for the presence of a residual stress/strain from spin-coating PS into this calculation. Chung et al.[18] quantified that approximately 30 MPa stress occurs when PS films were prepared via spin-coating. The 30 MPa residual stress (σ_R) correlates to a 0.8 % residual strain (ε_R),

$$\sigma_R = \bar{E}_f \varepsilon_R \qquad \text{Equation 6}$$

where $\bar{E}_f$ is approximately 4.14 GPa for the PS film. The residual strain arises from the fact that spin-coating is inherently a non-equilibrium process and some amount of residual stress/strain is trapped in the film after spin coating.[38,39] During the spin-coating process, the polymer film vitrifies and solidifies when the polymer solution reaches ambient temperature. During the solidification process, there is a large volume change that occurs and this leads to the generation of tensile residual stress in the plane of the coating. Therefore, we take into account the 0.8 % residual strain that occurs when spin-coating PS films and account for it in our calculation of applied compressive strain. After accounting for 0.8 % residual strain in our analysis, we showed that the calculated strain versus measured strain are in excellent agreement (Figure 4.1d). The close agreement

between the calculated and measured strain data corroborates that equation 5 is a valid expression to quantify strain without knowledge of the Young's moduli of the skin layer or underlying substrate.

4.3.2 Calculating Compressive Strain of Wrinkled Polymer Brush Surfaces

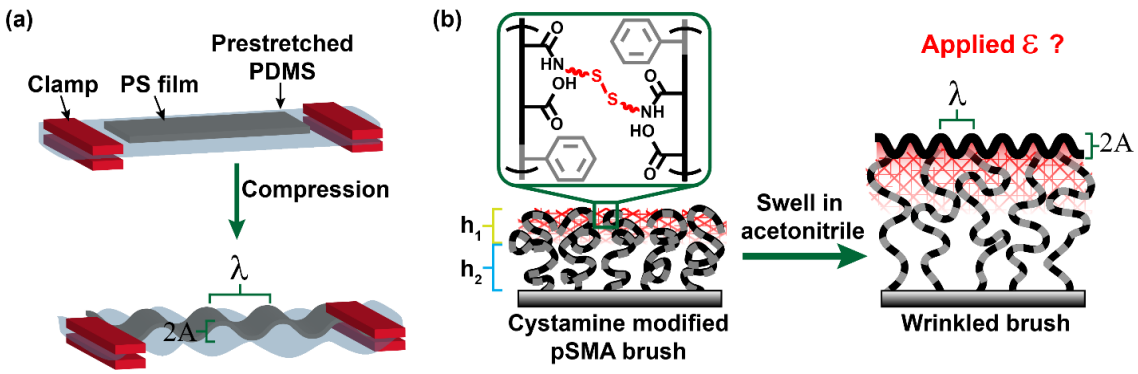

Scheme 4.2 Schematic illustration of (a) PS on PDMS model system utilized to validate equation 5, and (b) wrinkled cystamine-modified pSMA brush surfaces, where h_1 and h_2 represent the cystamine-modified thickness and unmodified thickness layers, respectively. The applied strain, ε, to induce surface wrinkling is unknown.

After validation of equation 5, we next applied it to the wrinkled pSMA brush system where the applied compressive strain is unknown (Scheme 4.2b). It is important to note that these calculations are based on wrinkling data we previously reported.[26] In brief, pSMA brushes with an initial thickness of 80 nm were post-modified with cystamine under aqueous conditions at discrete reaction times and various anhydride conversions. The cystamine-modified brush can be divided into two layers – the cystamine-modified cross-linked "skin" layer (h_1) and the unmodified layer (h_2). At each anhydride conversion (k), a typical features morphology was observed (Figure 4.2a) via AFM. The anhydride conversion was calculated based on the difference in brush thickness before and after post-modification with cystamine.[40] Next, the brushes were exposed to good solvent conditions (acetonitrile) to generate an in-plane compressive

stress arising from the mismatch between lateral and perpendicular swelling within the brush. Above a critical swelling ratio of 1.8, the stress causes an out-of-plane deformation of the untethered brush surface leading to the observed wrinkled morphologies shown in Figure 4.2b.

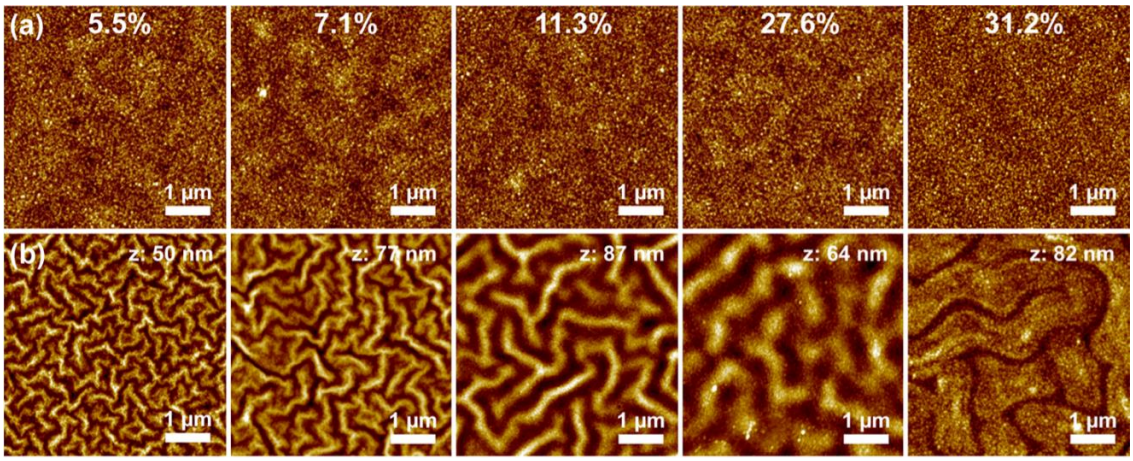

Figure 4.2 AFM images of (a) cystamine-modified brushes at discrete reaction times and anhydride conversions and (b) subsequent exposure to good solvent (acetonitrile) conditions. Reproduced with permission.[26]

An empirical relationship we previously derived between anhydride conversion and brush thickness was used to determine the cystamine-modified skin thickness (h_1).[26] An example calculation is provided in the experimental section. The wavelength was calculated by taking the radial average of the AFM 2D fast Fourier transform power spectrum. The wrinkle amplitude was measured from the RMS amplitude by taking a cross-section of the AFM image in Nanoscope Analysis software. An average of 20 cross-sections was taken to minimize error. The values of wavelength, amplitude, and h_1 for each wrinkled pSMA brush scaffold were used to quantify strain of the wrinkled pSMA brushes according to equation 5. The strain values are shown in Table 4.1.

Table 4.1 Calculated values of applied strain based on cystamine-modified thickness (h_1), wrinkle wavelength (λ), and wrinkle amplitude (A) from equation 5.

Conversion (%)	h_1 (nm)	Wavelength (nm)	Amplitude (nm)	Calculated Strain (%)
5.5	7.16	315	3.36	0.62
7.1	9.18	411	5.60	0.68
11.3	15.86	480	6.45	1.26
27.6	37.29	968	6.51	1.51
31.2	39.25	1000	6.65	1.56

The strain values ranged from 0.62 % to 1.56 % for the wrinkled brush system. These values are representative of the calculated strain above the critical strain. For the wrinkled pSMA brush system, we can only calculate strain after wrinkles are observed. However, from equation 3, the critical strain that leads to the wrinkled morphologies is inversely related to the skin's modulus, E_{h_1}. Although we lack the ability to determine the modulus of the "skin" and unmodified "substrate" layers individually, we previously established a scaling relationship for a rigid-on-soft multilayer construct, $\lambda \sim (h_1 h_2)^{1/2}(E_{h_1}/E_{h_2})^{1/6}$, where E_{h_1} and E_{h_2} represent the Young's moduli of the cystamine-modified "skin" layer and unmodified layer.[26] From this scaling relationship, an increase in cystamine-modified thickness, h_1, and an increase in wrinkle wavelength result in an increase in the modulus ratio, $(E_{h_1}/E_{h_2})^{1/6}$. For example, a cystamine-modified pSMA brush (k = 5.5 %) with $h_1 = 7.16$ nm, $h_2 = 74.18$ nm, and λ = 315 nm results in a $(E_{h_1}/E_{h_2})^{1/6}$ value of 13.66. Increasing the conversion to 31.3 % with a $h_1 = 39.25$ nm, $h_2 = 52.15$ nm, and λ = 1000 nm results in a $(E_{h_1}/E_{h_2})^{1/6}$ value of 22.10. Thus, as the skin's modulus (E_{h_1}) increases with an increase in cystamine-modified "skin" layer thickness (h_1), the critical strain for wrinkling to occur decreases (equation

3), and the calculated applied compressive strain above the critical strain increases. Although equation 5 allowed us to quantify the applied strain for the wrinkled pSMA brush surfaces, we corroborated the calculated strain values in Table 4.1 using another set of data described in the next section. Specifically, we utilized the relationship between applied strain and the persistence length of aligned wrinkled morphologies via AFM lithography techniques.

4.3.3 Quantifying Persistence Lengths of Aligned Wrinkled pSMA Brushes

The ability to control the finer aspects of wrinkled morphologies beyond wrinkle wavelength and amplitude (e.g. wrinkle orientation and persistence length) is an important aspect for the design of novel materials with well-ordered and controlled topographies. For instance, if we can quantify the applied strain of wrinkled bilayer systems, then we can make predictions about persistence lengths of aligned wrinkled morphologies for applications in microlens arrays,[41] diffraction gratings,[16,36] and open-channel microfluidics.[42]

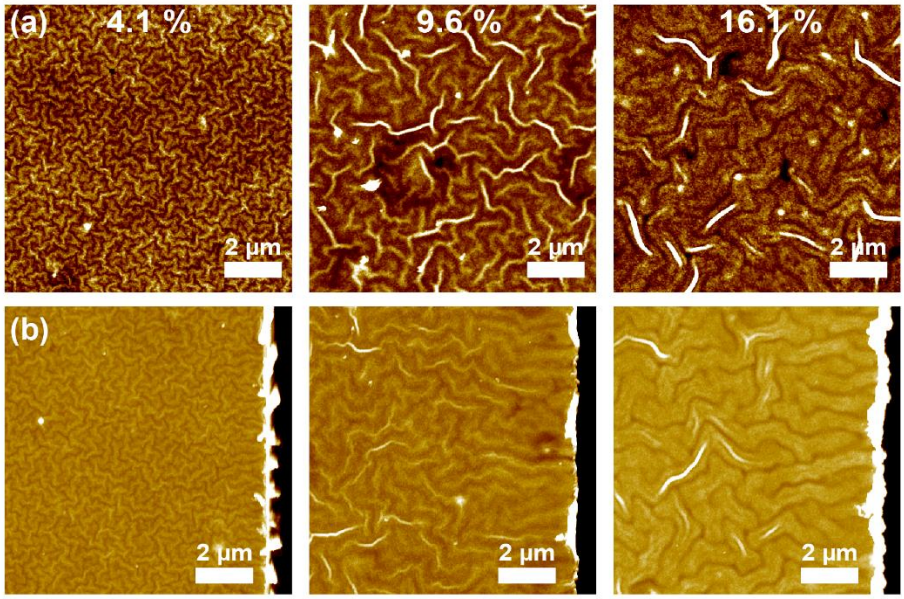

Figure 4.3 AFM images of (a) unpatterned and (b) patterned cystamine-modified pSMA brush (H_o= 97 nm) after swelling in acetonitrile at 4.1 %, 9.6 %, and 16.1 % anhydride conversion.

In this work, we exploit AFM lithography to pattern the pSMA brush surfaces to align the wrinkled morphologies. pSMA brushes with an initial thickness of 97 nm were modified with cystamine to afford brushes with 4.1 %, 9. 6 % and 16.1 % anhydride conversion. Figure 4.3 shows the AFM height images of the unpatterned and patterned cystamine-modified pSMA brushes after swelling in acetonitrile. The unpatterned surfaces (Figure 4.3a) exhibited an equi-biaxial state of stress, where there is not a preferred orientation for the wrinkles to form and thus show isotropic morphologies. When employing AFM lithography, the wrinkles aligned perpendicular to the boundary (Figure 4.3b). Near the boundary, the compressive stress in the direction perpendicular to the edge was released due to the discontinuity of the densely grafted polymer brush (stress-free boundary condition). Upon swelling in acetonitrile, the surface experiences stress parallel to the edge resulting in aligned wrinkles in the perpendicular direction.[2,7]

Near the boundary the wrinkles persist over a finite distance until they become isotropic. The length over which the wrinkle is aligned is referred to as the persistence length, ξ. Groenewold has defined the persistence length as[24,43]

$$\xi = \lambda\left(\frac{1}{2\varepsilon^{1/2}} + 2\left(\frac{1}{4(1-\nu_s^2)}\frac{E_f}{E_s}\right)^{1/3}\right) \qquad \text{Equation 7}$$

where ε is the strain applied to the rigid skin layer from the osmotic stress upon swelling and E_f and E_s represent the modulus of the film and substrate, respectively. However, there are two limiting cases that quantify the persistence length. For the case of a bilayer film comprised of a thin rigid film on a viscoelastic substrate at sufficiently low strain, the persistence length can be simplified to the following scaling relationship[23,24]

$$\xi = \frac{0.5\lambda}{\varepsilon^{1/2}} \qquad \text{Equation 8}$$

where ξ is dictated by the wrinkle wavelength and applied compressive strain. The second case is for high applied strains of a bilayer film, where the persistence length is proportional to the wrinkle wavelength.

$$\xi = \frac{\lambda^2}{2\pi h_1} \qquad \text{Equation 9}$$

However, equation 9 is independent of applied strain, where Groenewold describes the persistence length within domains or grains of aligned wrinkles, not the persistence length of aligned wrinkles from an edge. Therefore, for this work, we utilized Equation 8 to calculate the persistence length of the aligned wrinkled pSMA brushes. The relationship between persistence length and applied strain in equation 8 will allow us to corroborate the calculated strain values of the pSMA brush surfaces observed in Table 4.1 and further validate calculations of the persistence length of aligned wrinkles. First, we calculated the strain of the pSMA wrinkled brushes in Figure 4.3 using equation 5

with knowledge of the cystamine-modified thickness, wrinkle wavelength, and wrinkle amplitude. The calculated strain values were plugged into equation 8 in order to calculate the persistence length, ξ. From equation 8, we established relationships between wrinkle wavelength and applied strain versus the calculated ξ. As shown in Figure 4.4a, the wrinkle wavelength scales linearly with calculated ξ as expected from equation 8. Furthermore, Figure 4.4b shows the applied strain exhibits a non-linear relationship as a function of calculated ξ (by equation 8, $\xi \sim \varepsilon^{1/2}$). Most importantly, the calculated and measured persistence lengths are compared and the results are shown in Table 4.2 and Figure 4.4c.

Table 4.2 Calculated versus measured persistence length of patterned pSMA wrinkled brushes

Conversion (%)	h_1 (nm)	Wavelength (nm)	Amplitude (nm)	Calculated Strain (%)[a]	Calculated ξ (nm)[b]	Measured ξ (nm)[c]
4.1	6.48	270	2.12	0.63	1701	1683
9.6	15.13	450	2.54	1.14	2107	2136
16.1	25.38	705	3.67	1.31	3079	3028

[a]Calculated from equation 5, [b]Calculated from equation 8, [c]Measured from equation 10 and ImageJ analysis.

The measured persistence lengths were obtained by following a previously reported procedure.[22,27,28] In brief, persistence lengths were measured by drawing contour lengths (ten contours per image) using ImageJ 1.51a[29] software. Tangent vectors were drawn along the lengths of the contour with an angle θ and a distance *s* between the tangents. The persistence length ξ was calculated according to the following equation:

$$\langle \cos(\theta(s)) \rangle = e^{-s/2\xi} \qquad \text{Equation 10}$$

where $\langle\cos(\theta(s))\rangle$ is the average cosine of the θ between the tangent vectors. Three angles between the tangent vectors were measured for each contour, resulting in 30 total measurements. The results were averaged to obtain the measured persistence length values in Table 4.2.

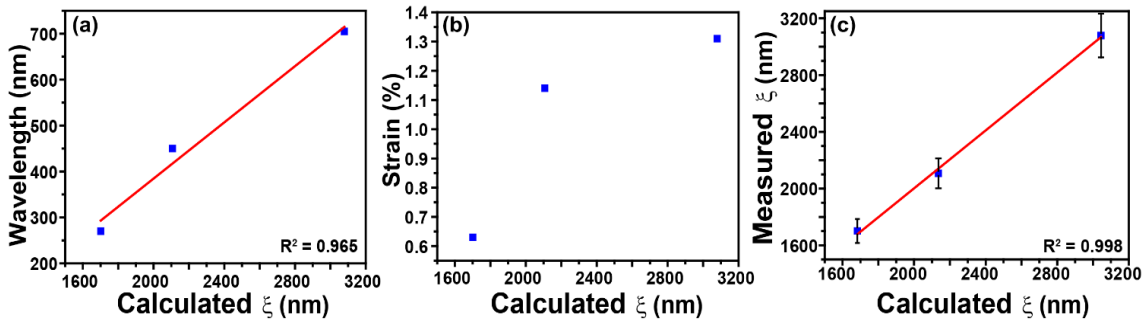

Figure 4.4 Relationship between (a) wrinkle wavelength, (b) applied strain, and (c) measured persistence length ξ versus calculated persistence length ξ.

The linear relationship in Figure 4.4c depicts an excellent agreement between the measured ξ with the calculated ξ. For example, from Table 4.2, a patterned cystamine-modified pSMA brush (9.6 % anhydride conversion, $h_1 = 15.13$ nm) with a wavelength of 450 nm yielded a measured persistence length of approximately 2136 nm. In comparison, a cystamine-modified brush (9.6 % anhydride conversion, $h_1 = 15.13$ nm) with a wavelength of 450 nm and applied compressive strain of 1.14 % resulted in a calculated persistence length (equation 8) of 2107 nm. The close agreement between the calculated and measured persistence lengths corroborates the calculated strain values for the wrinkled pSMA brush surfaces, further validating equation 5. In addition, we can further corroborate the calculated strain values by plugging the measured persistence length values into equation 8 to calculate applied strain, which can then be compared to the strain values from Table 4.1. For example, a wrinkled pSMA brush with wrinkle

wavelength of 450 nm and a measured persistence length of approximately 2099 nm, result in a strain value of 1.11 % from equation 8. The calculated strain is in close agreement obtained from our data in Table 4.1; the strain is 1.26 % for a wrinkled pSMA brush with a wrinkle wavelength of 480 nm Therefore, these data further support the derived equation 5, where applied strain can be calculated by measuring wrinkle wavelength, amplitude, and skin thickness. More importantly, the ability to quantify the applied strain of wrinkled films allow us to make predictions about persistence lengths of ordered wrinkled surfaces. Furthermore, we can establish a relationship between persistence length and wrinkle wavelength, where larger wrinkle wavelengths result in larger persistence lengths. These observations demonstrate that persistence length can be judiciously tuned and quantified by controlling wrinkle wavelength and calculating applied strain, respectively.

4.4 Conclusion

In summary, we derived an expression to deduce the compressive strain of wrinkled pSMA brush surfaces with knowledge of the cystamine-modified "skin" thickness (h_1), wrinkle wavelength, and wrinkle amplitude. The expression was validated using a prototypical model system, e.g., stiff, thin film (PS) bonded to a thick, compliant substrate (PDMS). Next, we utilized this expression to quantify applied strain of previously reported wrinkled pSMA brush surfaces, where the strain values range from 0.62 % to 1.56 %. Finally, we further validate the derived expression by elucidating the relationship between applied compressive strain and persistence length of aligned wrinkles via AFM lithography.

4.5 Acknowledgments

CMR acknowledges support from the NSF Graduate Research Fellowship Program (DGE-1445151) and traineeship support from the NSF NRT program “Interface” (DGE-1449999). *In situ* strain stage measurements were conducted at the Materials Science & Engineering Division at NIST.

4.6 References

(1) Cerda, E.; Mahadevan, L. Geometry and Physics of Wrinkling. *Phys. Rev. Lett.* **2003**, *90* (7), 074302. https://doi.org/10.1088/0264-9381/20/6/701.

(2) Yang, S.; Khare, K.; Lin, P. C. Harnessing Surface Wrinkle Patterns in Soft Matter. *Adv. Funct. Mater.* **2010**, *20* (16), 2550–2564. https://doi.org/10.1002/adfm.201000034.

(3) Genzer, J.; Groenewold, J. Soft Matter with Hard Skin: From Skin Wrinkles to Templating and Material Characterization. *Soft Matter* **2006**, *2* (4), 310–323. https://doi.org/10.1039/b516741h.

(4) Khang, D.-Y.; Jiang, H.; Huang, Y.; Rogers, J. A. A Stretchable Form of Single-Crystal Silicon for High-Performance Electronics on Rubber Substrates. *Science* **2006**, *311*, 208–212. https://doi.org/10.1126/science.1121401.

(5) Xu, B.; Chen, D.; Hayward, R. C. Mechanically Gated Electrical Switches by Creasing of Patterned Metal/Elastomer Bilayer Films. *Adv. Mater.* **2014**, *26* (25), 4381–4385. https://doi.org/10.1002/adma.201400992.

(6) Su, Y.; Ping, X.; Yu, K. J.; Lee, J. W.; Fan, J. A.; Wang, B.; Li, M.; Li, R.; Harburg, D. V.; Huang, Y. A.; Yu, C.; Mao, S.; Shim, J.; Yang, Q.; Lee, P. Y.; Armonas, A.; Choi, K. J.; Yang, Y.; Paik, U.; Chang, T.; Dawidcsyk, T. J.; Huang, Y.; Wang, S.; Rogers, J. A. In-Plane Deformation Mechanics for Highly Stretchable Electronics. *Adv. Mater.* **2017**, *29* (8), 1–12. https://doi.org/10.1002/adma.201604989.

(7) Stafford, C. M.; Harrison, C.; Beers, K. L.; Karim, A.; Amis, E. J.; Vanlandingham, M. R.; Kim, H. C.; Volksen, W.; Miller, R. D.; Simonyi, E. E. A Buckling-Based Metrology for Measuring the Elastic Moduli of Polymeric Thin Films. *Nat. Mater.* **2004**, *3* (8), 545–550. https://doi.org/10.1038/nmat1175.

(8) Khang, D. Y.; Rogers, J. A.; Lee, H. H. Mechanical Buckling: Mechanics, Metrology, and Stretchable Electronics. *Adv. Funct. Mater.* **2009**, *19* (10), 1526–1536. https://doi.org/10.1002/adfm.200801065.

(9) Wilder, E. A.; Guo, S.; Lin-Gibson, S.; Fasolka, M. J.; Stafford, C. M. Measuring the Modulus of Soft Polymer Networks via a Buckling-Based Metrology. *Macromolecules* **2006**, *39* (12), 4138–4143. https://doi.org/10.1021/ma060266b.

(10) Bae, H. J.; Bae, S.; Park, C.; Han, S.; Kim, J.; Kim, L. N.; Kim, K.; Song, S. H.; Park, W.; Kwon, S. Biomimetic Microfingerprints for Anti-Counterfeiting Strategies. *Adv. Mater.* **2015**, *27* (12), 2083–2089. https://doi.org/10.1002/adma.201405483.

(11) Chung, J. Y.; Nolte, A. J.; Stafford, C. M. Surface Wrinkling : A Versatile Platform for Measuring Thin-Film Properties. *Adv. Mater.* **2011**, *23*, 349–368. https://doi.org/10.1002/adma.201001759.

(12) O'Connor, B.; Chan, E. P.; Chan, C.; Conrad, B. R.; Richter, L. J.; Kline, R. J.; Heeney, M.; McCulloch, I.; Soles, C. L.; DeLongchamp, D. M. Correlations between Mechanical and Electrical Properties of Polythiophenes. *ACS Nano* **2010**, *4* (12), 7538–7544. https://doi.org/10.1021/nn1018768.

(13) Chan, E. P.; Lin, Q.; Stafford, C. M. Quantifying the Elasticity and Viscosity of Geometrically Confined Polymer Films via Thermal Wrinkling. *J. Polym. Sci. Part*

B Polym. Phys. **2012**, *50* (22), 1556–1561. https://doi.org/10.1002/polb.23152.
(14) Bowden, N.; Huck, W. T. S.; Paul, K. E.; Whitesides, G. M. The Controlled Formation of Ordered, Sinusoidal Structures by Plasma Oxidation of an Elastomeric Polymer. *Appl. Phys. Lett.* **1999**, *75* (17), 2557–2559. https://doi.org/10.1063/1.125076.
(15) Huck, W. T. S.; Bowden, N.; Onck, P.; Pardoen, T.; Hutchinson, J. W.; Whitesides, G. M. Ordering of Spontaneously Formed Buckles on Planar Surfaces. *Langmuir* **2000**, *16* (7), 3497–3501. https://doi.org/10.1021/la991302l.
(16) Bowden, N.; Brittain, S.; Evans, A. G.; Hutchinson, J. W.; Whitesides, G. M. Spontaneous Formation of Ordered Structures in Thin Films of Metals Supported on an Elastomeric Polymer. *Nature* **1998**, *393*, 146–149.
(17) Stafford, C. M.; Vogt, B. D.; Harrison, C.; Julthongpiput, D.; Huang, R. Elastic Moduli of Ultrathin Amorphous Polymer Films. *Macromolecules* **2006**, *39* (15), 5095–5099. https://doi.org/10.1021/ma060790i.
(18) Chung, J. Y.; Chastek, T. Q.; Fasolka, M. J.; Ro, H. W.; Stafford, C. M. Quantifying Residual Stress in Nanoscale Thin Polymer Films via Surface Wrinkling. *ACS Nano* **2009**, *3* (4), 844–852. https://doi.org/10.1021/nn800853y.
(19) Chan, E. P.; Page, K. A.; Im, S. H.; Patton, D. L.; Huang, R.; Stafford, C. M. Viscoelastic Properties of Confined Polymer Films Measured via Thermal Wrinkling. *Soft Matter* **2009**, *5* (23), 4638–4641. https://doi.org/10.1039/b916207k.
(20) Guvendiren, M.; Burdick, J. A.; Yang, S. Solvent Induced Transition from Wrinkles to Creases in Thin Film Gels with Depth-Wise Crosslinking Gradients. *Soft Matter* **2010**, *6* (22), 5795–5801. https://doi.org/10.1039/c0sm00317d.
(21) Kim, H. S.; Crosby, A. J. Solvent-Responsive Surface via Wrinkling Instability. *Adv. Mater.* **2011**, *23* (36), 4188–4192. https://doi.org/10.1002/adma.201101477.
(22) Paci, J. T.; Chapman, C. T.; Lee, W. K.; Odom, T. W.; Schatz, G. C. Wrinkles in Polytetrafluoroethylene on Polystyrene: Persistence Lengths and the Effect of Nanoinclusions. *ACS Appl. Mater. Interfaces* **2017**, *9* (10), 9079–9088. https://doi.org/10.1021/acsami.6b14789.
(23) Lim, J.; Choi, S. J.; Kim, P. Controlling Wrinkle Propagation in the Bilayer System with Thickness-Gradient. *Adv. Mater. Interfaces* **2018**, *5* (2), 1–7. https://doi.org/10.1002/admi.201701109.
(24) Groenewold, J. Wrinkling of Plates Coupled with Soft Elastic Media. *Physica A* **2001**, *298*, 32–45. https://doi.org/10.1016/S0378-4371(01)00209-6.
(25) Huang, H.; Chung, J. Y.; Nolte, A. J.; Stafford, C. M. Characterizing Polymer Brushes via Surface Wrinkling. *Chem. Mater.* **2007**, *19* (26), 6555–6560. https://doi.org/10.1021/cm702456u.
(26) Guo, W.; Reese, C. M.; Xiong, L.; Logan, P. K.; Thompson, B. J.; Stafford, C. M.; Ievlev, A. V.; Lokitz, B. S.; Ovchinnikova, O. S.; Patton, D. L. Buckling Instabilities in Polymer Brush Surfaces via Postpolymerization Modification. *Macromolecules* **2017**, *50* (21), 8670–8677. https://doi.org/10.1021/acs.macromol.7b01888.
(27) Mücke, N.; Klenin, K.; Kirmse, R.; Bussiek, M.; Herrmann, H.; Hafner, M.; Langowski, J. Filamentous Biopolymers on Surfaces : Atomic Force Microscopy

Images Compared with Brownian Dynamics Simulation of Filament Deposition. *PLoS One* **2009**, *4* (11), 1–7. https://doi.org/10.1371/journal.pone.0007756.
(28) Mücke, N.; Kreplak, L.; Kirmse, R.; Wedig, T.; Herrmann, H.; Aebi, U.; Langowski, J. Assessing the Flexibility of Intermediate Filaments by Atomic Force Microscopy. *J. Mol. Biol.* **2004**, *335*, 1241–1250. https://doi.org/10.1016/j.jmb.2003.11.038.
(29) *ImageJ*; National Institutes of Health, Bethesda, MD.
(30) Guo, W.; Xiong, L.; Reese, C. M.; Amato, D. V.; Thompson, B. J.; Logan, P. K.; Patton, D. L. Post-Polymerization Modification of Styrene-Maleic Anhydride Copolymer Brushes. *Polym. Chem.* **2017**, *8* (44), 6778–6785. https://doi.org/10.1039/c7py01659j.
(31) Patton, D. L.; Page, K. A.; Xu, C.; Genson, K. L.; Fasolka, M. J.; Beers, K. L. Measurement of Reactivity Ratios in Surface-Initiated Radical Copolymerization. *Macromolecules* **2007**, *40*, 6017–6020.
(32) Stafford, C. M.; Guo, S.; Harrison, C.; Chiang, M. Y. M. Combinatorial and High-Throughput Measurements of the Modulus of Thin Polymer Films. *Rev. Sci. Instrum.* **2005**, *76* (6), 1–5. https://doi.org/10.1063/1.1906085.
(33) Volynskii, A. L.; Bazhenov, S.; Lebedeva, O. V.; Bakeev, N. F. Mechanical Buckling Instability of Thin Coatings Deposited on Soft Polymer Substrates. *J. Mater. Sci.* **2000**, *35* (3), 547–554. https://doi.org/10.1023/A:1004707906821.
(34) Song, J. Herringbone Buckling Patterns of Anisotropic Thin Films on Elastomeric Substrates. *Appl. Phys. Lett.* **2010**, *96* (5), 597–603. https://doi.org/10.1063/1.3309696.
(35) Huang, R. Kinetic Wrinkling of an Elastic Film on a Viscoelastic Substrate. *J. Mech. Phys. Solids* **2005**, *53* (1), 63–89. https://doi.org/10.1016/j.jmps.2004.06.007.
(36) Harrison, C.; Stafford, C. M.; Zhang, W.; Karim, A. Sinusoidal Phase Grating Created by a Tunably Buckled Surface. *Appl. Phys. Lett.* **2004**, *85* (18), 4016–4018. https://doi.org/10.1063/1.1809281.
(37) Brandrup, J; Immergut, E.H; Grulke, E. A. *Polymer Handbook*, 4th ed.; Wiley: New York, 1999. https://doi.org/10.1038/238056a0.
(38) Croll, S. G. The Origin of Residual Internal Stress in Solvent-cast Thermoplastic Coatings. *J. Appl. Polym. Sci.* **1979**, *23* (3), 847–858. https://doi.org/10.1002/app.1979.070230319.
(39) Reiter, G.; de Gennes, P. G. Spin-Cast, Thin, Glassy Polymer Films: Highly Metastable Forms of Matter. *Eur. Phys. J. E* **2001**, *6*, 25–28. https://doi.org/10.1007/s101890170024.
(40) Murata, H.; Prucker, O.; Rühe, J. Synthesis of Functionalized Polymer Monolayers from Active Ester Brushes. *Macromolecules* **2007**, *40* (15), 5497–5503. https://doi.org/10.1021/ma0624550.
(41) Chan, E. P.; Crosby, A. J. Fabricating Microlens Arrays by Surface Wrinkling. *Adv. Mater.* **2006**, *18* (24), 3238–3242. https://doi.org/10.1002/adma.200601595.
(42) Khare, K.; Zhou, J.; Yang, S. Tunable Open-Channel Microfluidics on Soft Poly(Dimethylsiloxane) (PDMS) Substrates with Sinusoidal Grooves. *Langmuir* **2009**, *25* (21), 12794–12799. https://doi.org/10.1021/la901736n.

(43) Chan, E. P.; Crosby, A. J. Wrinkling Polymer for Surface Structure Control and Functionality. In *Polymer Thin Films*; Tsui, O. K. C., Russell, T. P., Eds.; World Scientific, 2008; pp 141–162.

CHAPTER V – CONCLUSIONS AND FUTURE WORK

The research presented in this dissertation is focused on the design of ultrathin polymer brush surfaces with multifunctional chemistries and tunable morphologies via post-polymerization modification (PPM) techniques. Specifically, this dissertation demonstrates methods to control PPM parameters to govern the through-thickness polymer brush composition.

In Chapter II, microwave-assisted surface-initiated polymerization was employed to synthesize poly(acrylamide-homocysteine thiolactone) (pAHT) brushes. The pAHT brushes served as a powerful platform to undergo sequential and one-pot amine-thiol-ene conjugation reactions. XPS depth profile experiments provided insight into the pAHT brush through-thickness composition and PPM efficiency (e.g. sequential vs one-pot reactions). The one-pot double modification strategy can be exploited with other chemistries to design surface with specific functionalities. Future work can exploit the kinetics of the thiolactone PPM reactions. Furthermore, the thiols formed upon aminolysis have the potential to undergo thiol-thioester or thiol-disulfide exchange reactions, which can be utilized for stimuli-responsive polymer brush applications (e.g. switchable bacteria-killing and bacteria-releasing surfaces).

In Chapter III, a simple PPM approach was utilized to engineer buckling instabilities (e.g. wrinkles) in ultrathin (poly(styrene-*alt*-maleic anhydride) (pSMA) brush surfaces. The wrinkled morphologies were judiciously tuned by PPM reaction time. ToF-SIMS depth profiling and *in situ* ellipsometry provided insight into the parameters that influence the buckling behavior. The control of brush thickness serves as an approach to control wrinkle wavelength. In addition, reversible-redox chemistry allowed the

formation of stimuli-responsive wrinkles. Future work can exploit other stimuli-responsive cross-linkers, such as a light-responsive azobenzene diamine, to induce morphological changes. In addition, sequential PPM reactions can be exploited to induce further functionality and induce other morphological transitions. Current work (not shown) has shown wrinkle to crease morphological transitions upon a sequential PPM reaction, however, the morphological transitions are not fully understood. Future work can exploit a comprehensive understanding of buckling transitions in polymer brush surfaces.

In Chapter IV, an expression to quantify the applied compressive strain was derived for bilayer systems where the strain is unknown or unmeasurable. The expression was validated using a prototypical bilayer model system (e.g. polystyrene on polydimethylsiloxane). Next, the expression was used to quantify strain of the wrinkled pSMA brushes. Finally, the strain values were corroborated using the relationship between strain and persistence length of aligned wrinkles. The ability to quantify strain can provide insight to quantify other mechanical properties of buckled polymer films. Furthermore, other patterning techniques such as microcontact printing or microcapillary patterning can be employed to further control wrinkle alignment. Future work can utilize soft lithography techniques for precise control of wrinkle alignment in new applications such as stretchable electronics and microlens arrays.

APPENDIX A – Supporting Information for Chapter II

Table A.1 Molecular weights of monomer and post-modifiers

Compound	MW (g/mol)
Thiolactone	171.21
Ethanolamine (EA)	61.08
Hexylamine (HA)	101.19
4-Bromobenzyl amine (BBA)	186.05
2-Hydroxyethyl acrylate (HEA)	116.12
1H, 1H-Perfluoro-n-decyl acrylate (FA)	554.15
2-(Perfluorobutyl)ethyl acrylate (FEA)	318.14

Table A.2 FTIR peak assignment of polymer brushes

Polymer Brush	Wavenumber cm^{-1}	
pAHT	1669	-C=O,
	1536	-N-H amide II
pAHT-EA	3300	-O-H
	1649	-C=O amide I
	1545	-N-H amide II
pAHT-HA	2931, 2864	-C-H
	1649	-C=O amide I
	1543	-N-H amide II
pAHT-EA-FEA	3400	-O-H
	1732	-C=O
	1652	-C=O amide I
	1545	-N-H amide II
	1226, 1136	-C-F
pAHT-HA-HEA	3400	-O-H
	2930, 2861	-C-H
	1730	-C=O
	1652	-C=O amide I
	1546	-N-H amide II
pAHT-EA-FEA one-pot	3400	-O-H
	1734	-C=O
	1653	-C=O amide I
	1543	-N-H amide II
	1228, 1136	-C-F

Table A.2 Continued FTIR peak assignment of polymer brushes

pAHT-HA-HEA one-pot	3400	-O-H
	2932, 2858	-C-H
	1731	-C=O
	1652	-C=O amide I
	1544	-N-H amide II

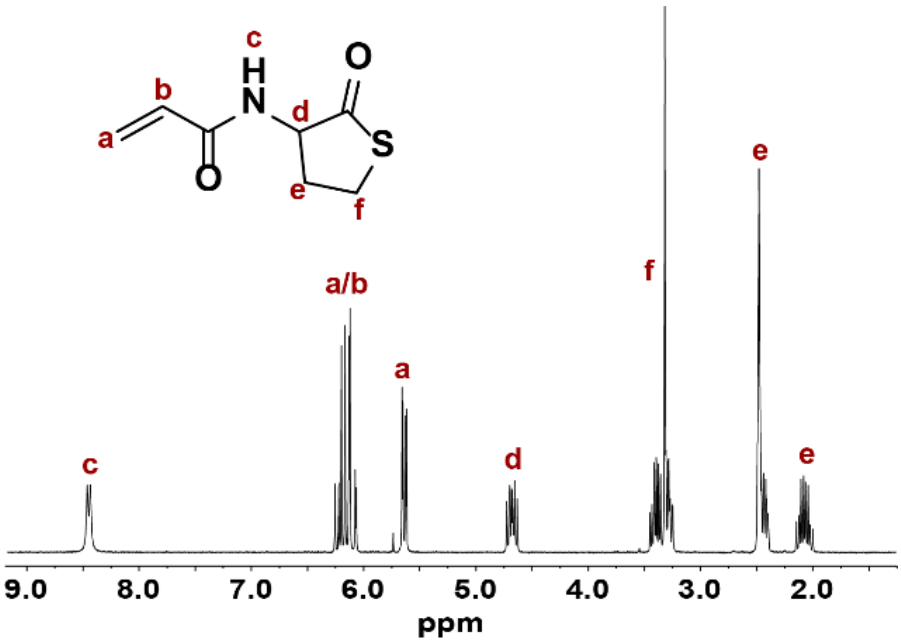

Figure A.1 ^{1}H NMR of the thiolactone acrylamide (TlAm) monomer

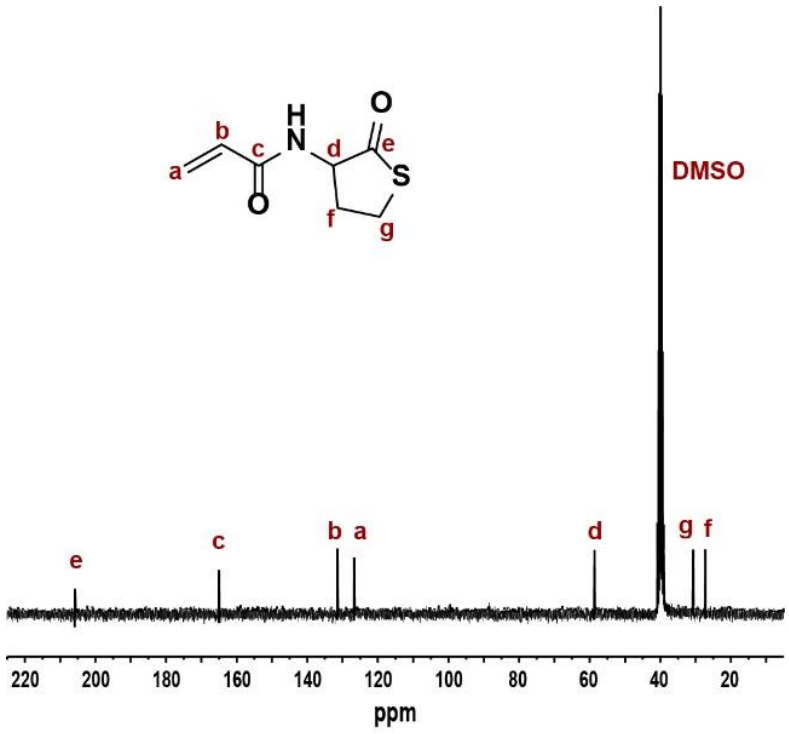

Figure A.2 ^{13}C NMR of the thiolactone acrylamide (TlAm) monomer

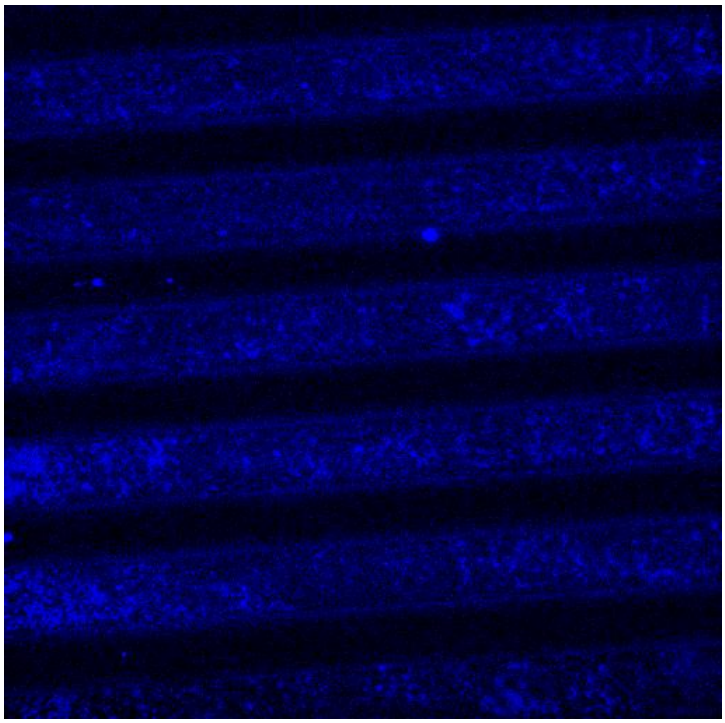

Figure A.3 Microcontact printing of dansylcadaverine on pAHT brush surface. Fluorescent microscopy images of dansylcadaverine-patterned pAHT brush with excitation at 405 nm.

APPENDIX B – Supporting Information for Chapter III

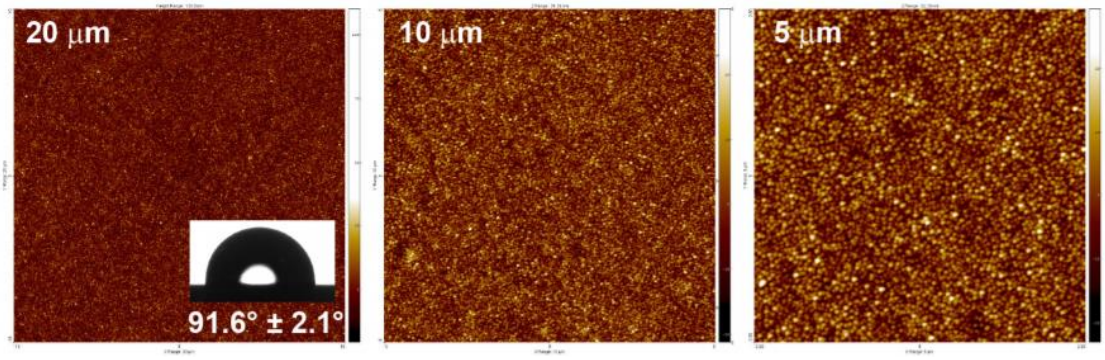

Figure B.1 AFM height images of a typical unmodified pSMA brush surface. Inset image shows the static water contact angle of the unmodified pSMA brush.

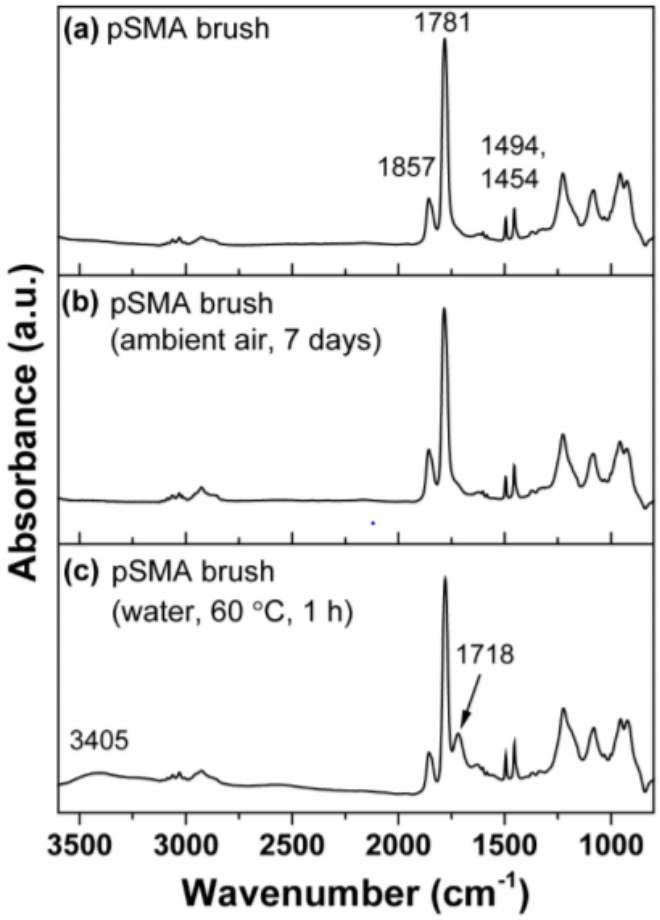

Figure B.2 ATR-FTIR spectra for a) pSMA brush, (b) pSMA brush exposed to ambient air at rt for 7 days, and c) pSMA brush heated at 60 °C for 1 h in DI water. The anhydride peaks at 1857 cm^{-1} and 1781 cm^{-1} remain unchanged in air, while a small peak at 1718 cm^{-1} (carboxylic acid) due to anhydride ring-opening appears only after heating in water for 1 h.

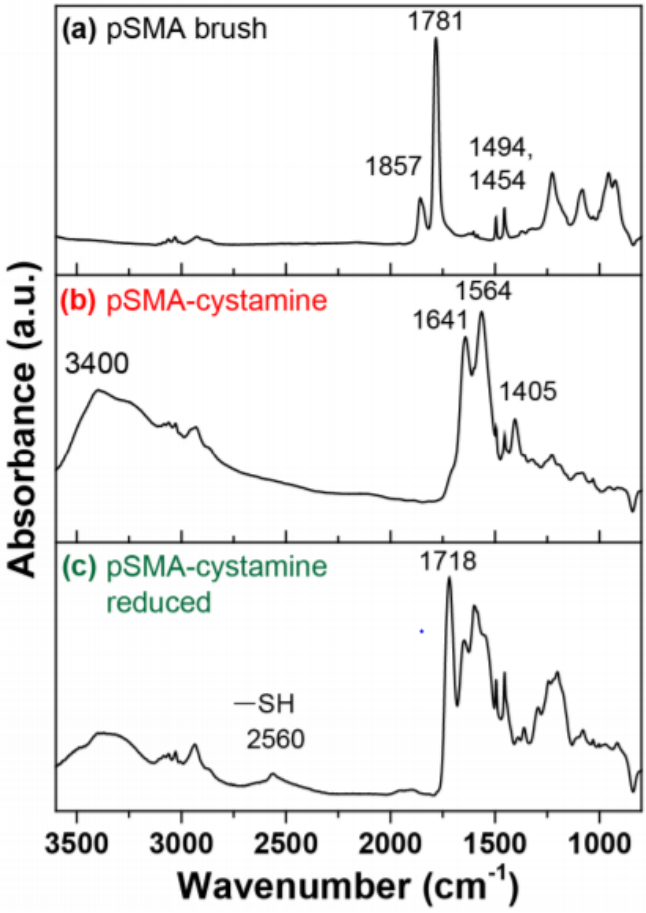

Figure B.3 ATR-FTIR: a) pSMA brush b) cystamine modified pSMA brush at full conversion c) cystamine modified pSMA brush after reduction. The disappearance of anhydride peaks (1857 cm^{-1} and 1781 cm^{-1}) and the appearance of the amide band (1641 cm^{-1}) after cystamine modification in (b) indicates full conversion of the anhydride-amine reaction. Following post-modification, much of the carboxylic acids moieties are present as carboxylate tertiary amine salts (1564 cm^{-1}, asym C=O, carboxylic salt; 1405 cm^{-1}, sym C=O, carboxylic salt). The thiol peak at 2560 cm^{-1} following exposure to TCEP in phosphate buffer indicates reduction of the disulfide linkage in cystamine.

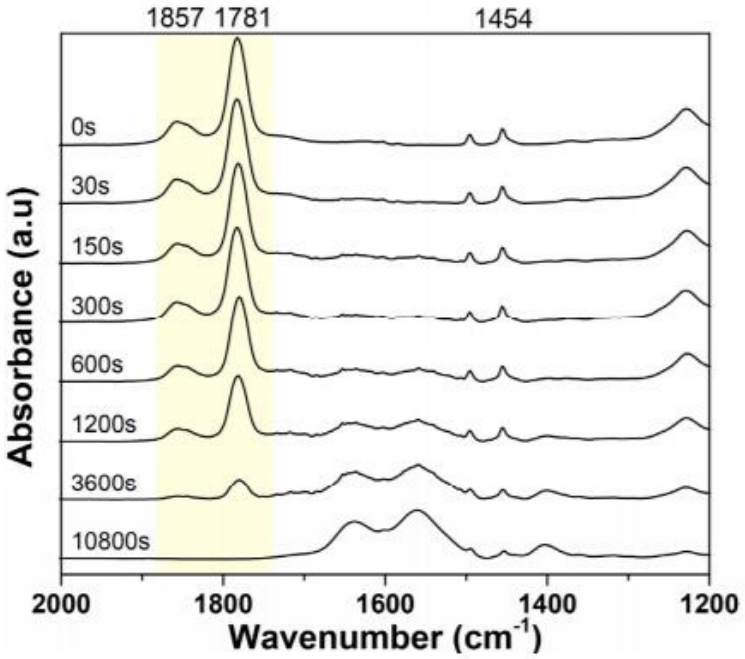

Figure B.4 ATR-FTIR spectra of pSMA post-modified with cystamine aqueous solution at discrete reaction times. The conversion of the amidation reaction of maleic anhydride at discrete times was calculated using anhydride peak area values (aromatic peak at 1454 cm^{-1} used as reference).

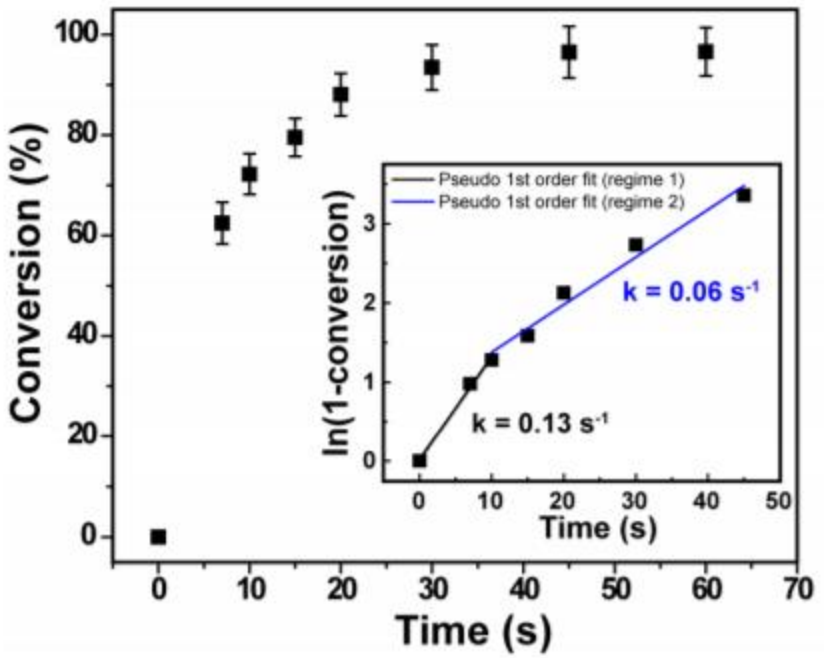

Figure B.5 Anhydride conversion versus cystamine reaction time for pSMA brush under good solvent conditions. Solvent employed for these measurements was 50:50 acetonitrile/water (v/v %).

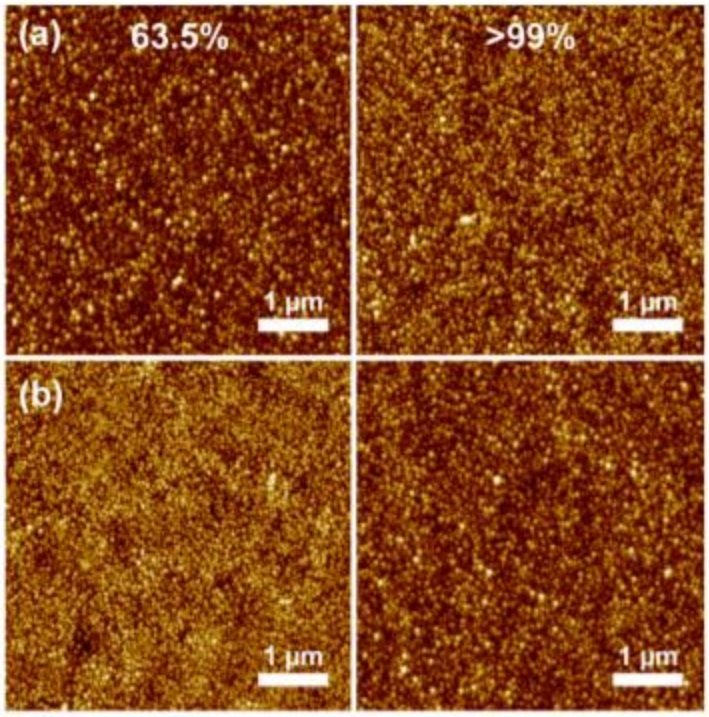

Figure B.6 AFM height images of pSMA brushes following (a) reaction with cystamine to >40 % conversion and (b) subsequent exposure to good solvent (acetonitrile) conditions.

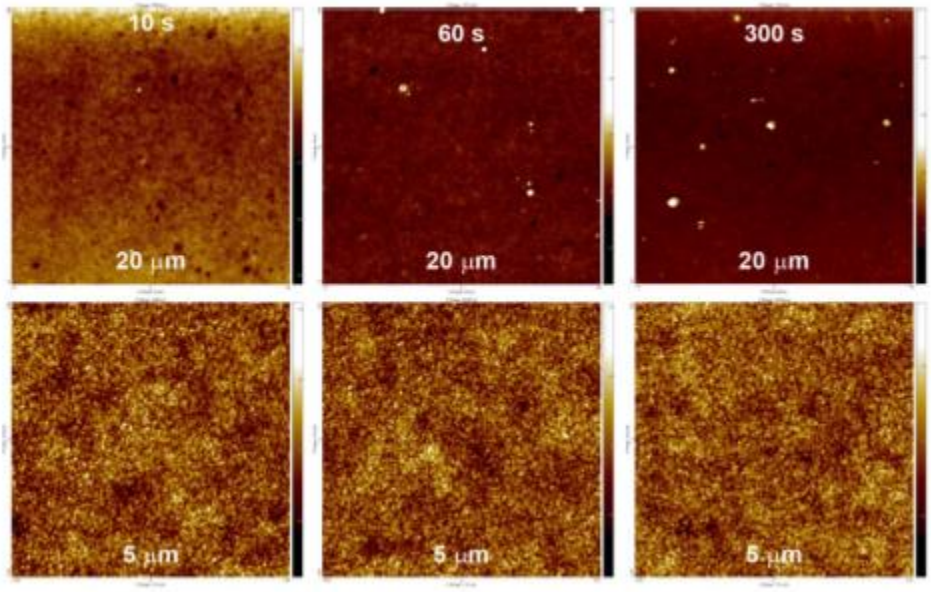

Figure B.7 AFM height images of pSMA brushes modified with cystamine under good solvent conditions (50:50 acetonitrile/water, v/v %) at discrete times.

Table B.1 Comparison of total brush thickness following cystamine modification via ToF-SIMS and ellipsometry measurements.

H_f ToF-SIMS (nm)	H_f Ellipsometry (nm)
87.6	87.4
90.0	90.1
86.0	86.0
91.5	94.0
103.2	107.3
120.0	121.0

Table B.2 Brush thickness parameters predicted by empirical relationships assuming a front-like post-modification process under poor solvent conditions. Predicted values are compared with measured values obtained from ToF-SIMS and ellipsometry measurements.

H_o (nm)	k (%)	$h_{1,\ emp}$ (nm)	$h_{1,\ SIMS}$ (nm)	$h_{2,\ emp}$ (nm)	$h_{2,\ SIMS}$ (nm)	$H_{f,\ emp}$ (nm)	$H_{f,\ ellip}$ (nm)	$H_{f,\ SIMS}$ (nm)
84.5	9.9	13.8	13.5	76.1	76.5	89.9	90.1	90.0
78.3	29.9	38.8	45.0	54.8	46.5	96.6	93.9	91.5
91.5	88.0	110.8	112.1	9.1	9.2	119.9	121.0	120.0
emp = empirical, ellip = ellipsometry								

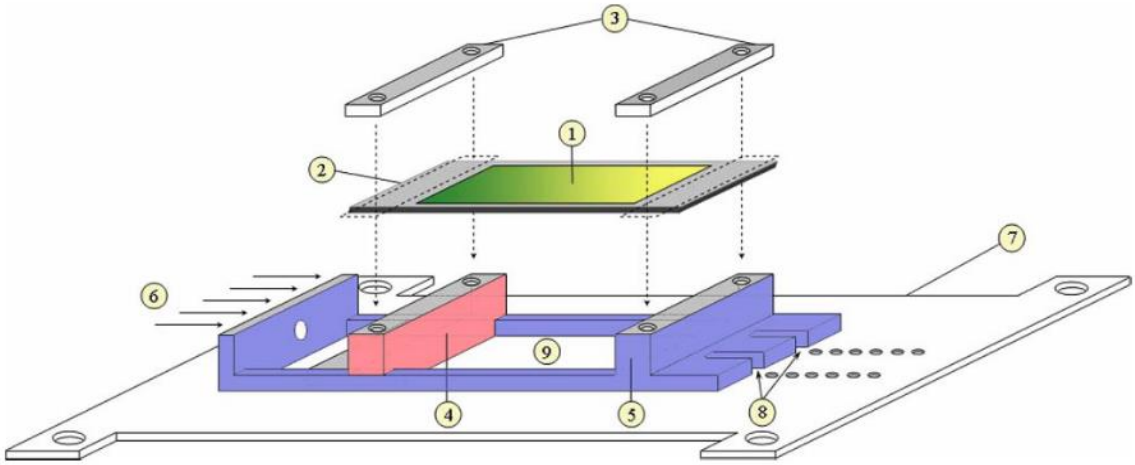

Scheme C.1 Strain stage design: (1) thin film mounted onto (2) elastic PDMS substrate. (3) Clamps for PDMS, (4) stationary grip, (5) moving sled grip, (6) motorized actuator for controlling compressional strain, (7) mounting plate, (8) grooves for locking in strain, and (9) window for measurements. Reproduced with permission.[32]

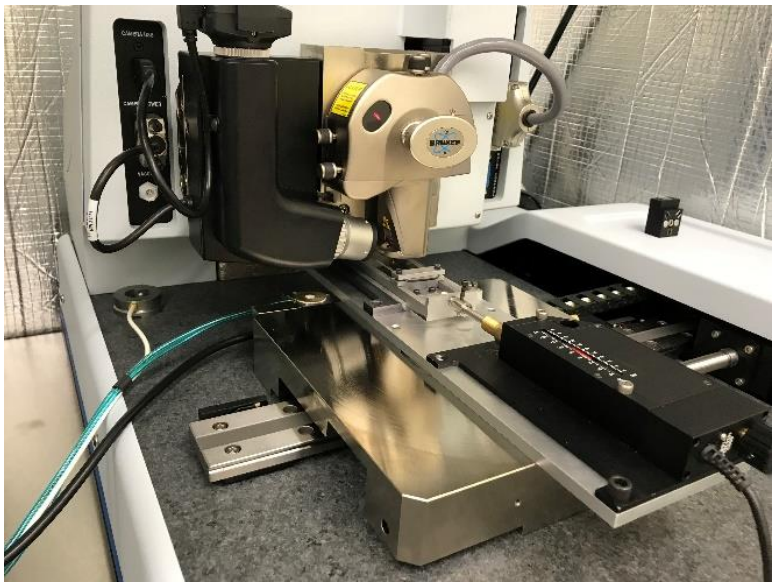

Figure C.2 *In situ* strain stage experiments under a Bruker Dimension Icon AFM

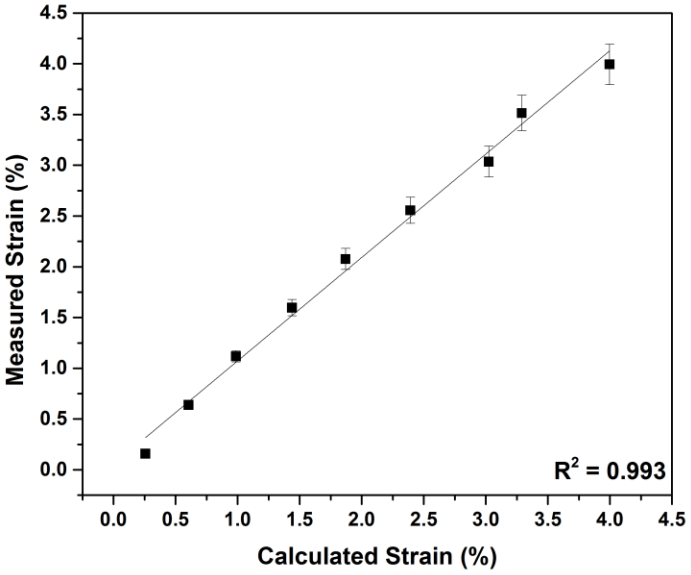

Figure C.3 Measured versus calculated strain (h_1= 96 nm)

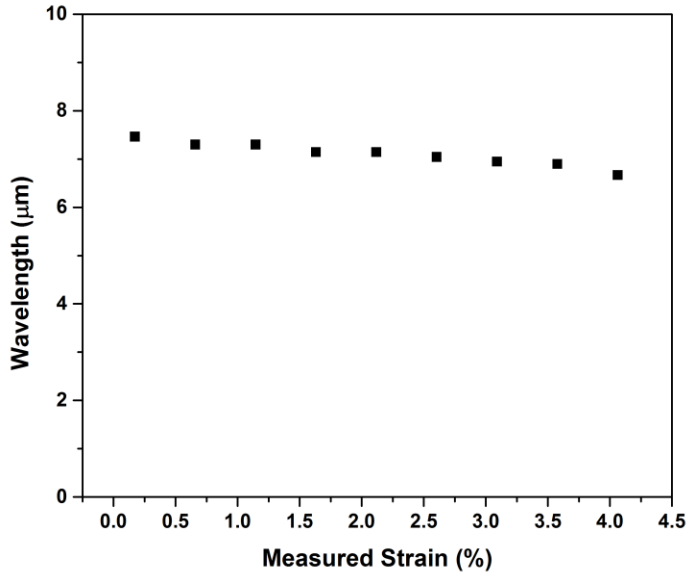

Figure C.4 Wavelength versus measured strain (h_1= 110 nm)

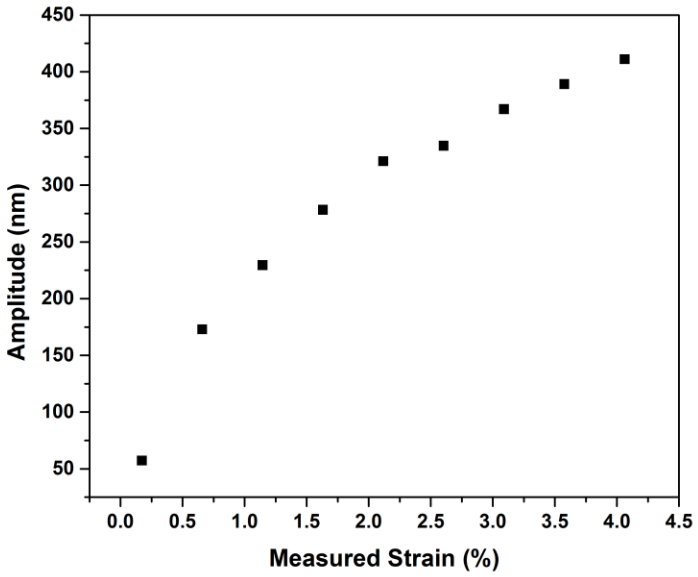

Figure C.5 Amplitude versus measured strain (h_1 = 110nm)

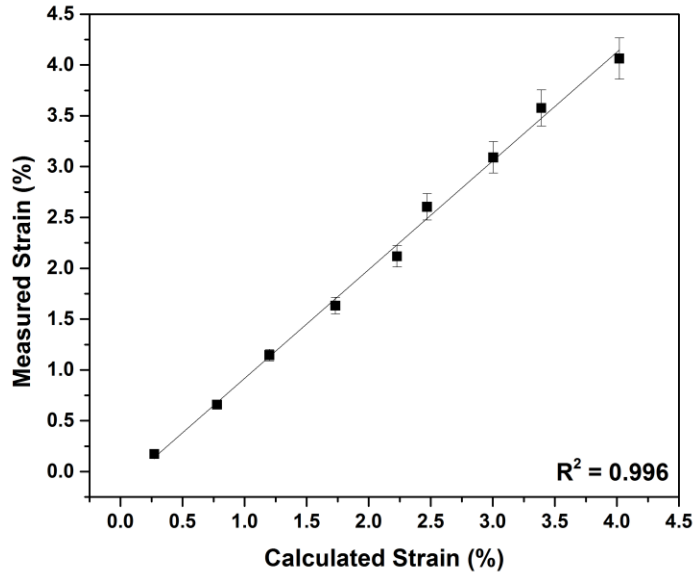

Figure C.6 Measured versus calculated strain (h_1= 110 nm)

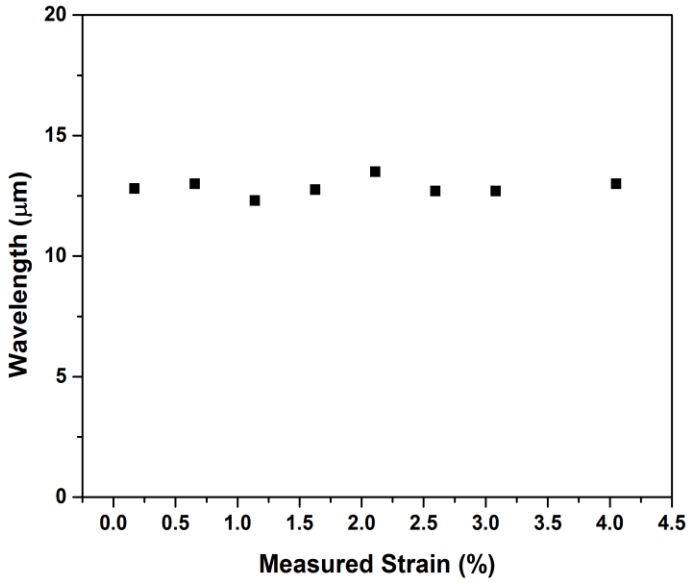

Figure C.7 Wavelength versus measured strain (h_1= 158 nm)

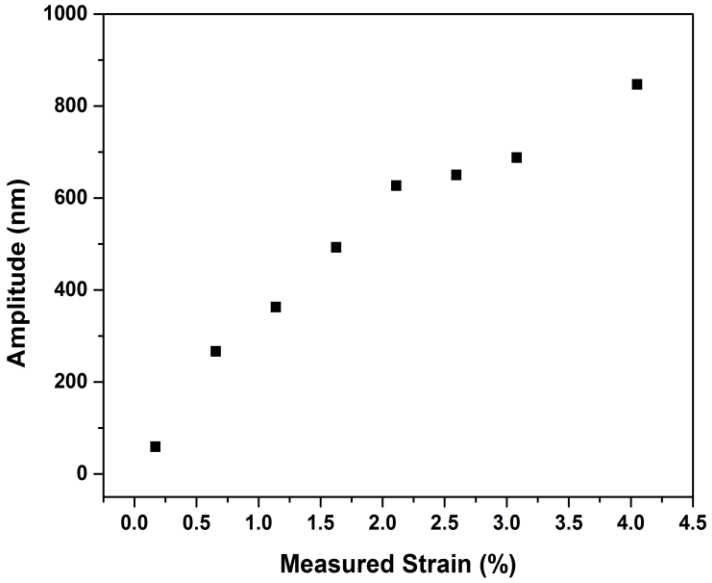

Figure C.8 Amplitude versus measured strain (h_1= 158 nm)

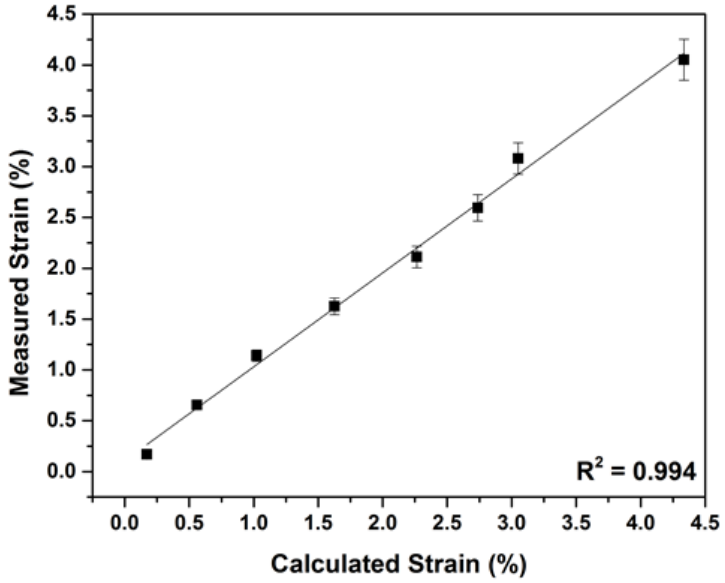

Figure C.9 Measured versus calculated strain (h_1= 158 nm)